Lübeck, Germany
06-07 June 2024

Proceedings of the

5th KuVS/GI Expert Talk on Localization

ITG VDE

GI

CoSA Center of Excellence

TECHNISCHE HOCHSCHULE LÜBECK

HI LUBECK www.hic-luebeck.de/hi

HIC Lübeck

HCU HafenCity Universität Hamburg

TECHNISCHE UNIVERSITÄT DRESDEN

Editors: Marco Cimdins, Horst Hellbrück, Harald Sternberg
DOI: 10.34712/142.51
Publisher: HafenCity University
Publication Date: 2024

Message from the Editors

Localization is an important technology in medical, industrial, underwater, and logistics applications. Many sectors will greatly benefit from advancements in localization. Despite the evolving research interest and emerging solutions, numerous technical challenges remain for various use cases.

The program of the 5th Expert Talk on Localization addresses a wide range of topics within this field. It includes discussions on innovative algorithms, numerous application scenarios, and supporting technologies, offering a comprehensive overview of current advancements. The 5th Expert Talk on Localization is as a platform for discussing recent research and development outcomes, and for sharing ideas and perspectives. It brings together researchers from academia and industry, featuring a broad spectrum of contributions, including complete localization systems and demonstrations.

We extend our gratitude to all authors for their contributions to the program. We appreciate the support from Technische Hochschule Lübeck, especially the project HI Lübeck, the organizational efforts of the Center of Excellence CoSA, and the continuous contributions from HafenCity University and Technische Universität Dresden. We also thank GI and KuVS for facilitating and supporting this event.

June 2024 M. Cimdins, H. Hellbrück & H. Sternberg

General Chair

Horst Hellbrück, Technische Hochschule Lübeck

Program Committee

Marco Cimdins, Technische Hochschule Lübeck
Marco Gunia, Technische Universität Dresden
Hossein Shoushtari, HafenCity University

Organization

Marco Cimdins, Technische Hochschule Lübeck

Table of Contents

Contributions

Evaluation of the Modular Design Structure for the UWB Single Anchor Localization System SALOS

Sven Ole Schmidt and Horst Hellbrück
Technische Hochschule Luebeck - University of Applied Sciences, Germany
Department of Electrical Engineering and Computer Science
Email: {sven.ole.schmidt, horst.hellbrück}@th-luebeck.de

***Abstract*—In the realm of indoor localization, one challenge is accurate positioning with minimal infrastructure. The motivation is a cost-effective and scalable solution for various applications. In this work, we introduce the modular design structure for our ultra-wideband single anchor localization system called SALOS. We demonstrate the structure's efficacy by evaluating localization lag, and position update interval, With maximum $561\,\text{ms}$ total localization lag and a position update rate of less than $500\,\text{ms}$ in 98% of measurements, we show the ability for live-localization.**

***Index Terms*—Single Anchor Localization, UWB, DW1000, Modularity, localization lag, Position Update Interval.**

I. Introduction

Indoor localization research has explored various methodologies, including optical, acoustic, and radio frequency (RF) techniques [1], [2]. RF-based solutions, while effective, often necessitate expensive setups [3]. Recent trends focus on cost reduction within a wireless network using a single anchor sensor node, simplifying the infrastructure drastically [4].

In our previous work [5], we introduce SALOS, an innovative ultra-wideband (UWB) single-anchor indoor localization system. SALOS contrasts with traditional systems by negating the need for extensive hardware nor external information during operation, instead utilizing sophisticated signal processing techniques. It operates by comparing real-time UWB measurements against a pre-modeled set of signals, generated artificially only from the environment's floor plan. In the given evaluation scenario, correct localization results for more than 73% of all position estimates. However, a capable positioning system does not only have to offer high position accuracy. For live operation, the total processing time from measurement to estimate, namely the *localization lag*, and the *update interval* of these estimates are vital for real-time localization and the system's responsiveness in dynamic environments.

In this work, we re-designed the system's architecture modularly to ensure scalability and adaptability due to suitable implementation and parallel computation. We evaluate the design in terms of localization lag and overall position update interval.

The contributions are as follows:

- We introduce the modular structure based on the concept of our single anchor localization system called SALOS.
- We evaluate the localization lag and the position update interval for this structure.
- We compare the position update interval with a sequential non-modular implementation.

II. Modular Structure of the UWB Single Anchor Localization Approach

The objective of UWB localization is to deduce the position of a tag sensor node by analyzing the signal transmission between the tag and an anchor sensor node. The anchor's received signal $y(t)$ constitutes a superposition of all the transmitted UWB pulses, encompassing both the direct path and the paths involving reflections off various surfaces such as walls or furniture. The received signal is given by the convolution of the transmitted signal $x(t)$ with the channel impulse response $h(t)$, as shown below:

$$y(t) = x(t) * h(t),$$

where the channel impulse response $h(t)$ encapsulates the effects of multipath propagation on the signal echo when passing the distinct paths.

The multipath propagation, when combined with the environmental floor map and the anchor position, furnishes sufficient data to geometrically deduce the tag's position.

A. General Concept of the Single Anchor Localization System

To derive a suitable modular structure for SALOS, a closer look at the system is inevitable to avoid miss-structuring leading to high position update intervals. Therefore, we briefly explain the methodology underpinning this concept. Note, that a more detailed description is covered in [5].

Initialization: The SALOS system requires a singular external input: a floor plan covering reflective surfaces. Based on the floor plan, a set of candidate points (CP) is established, representing the prospective tag coordinates. In [6], we determine the optimal anchor position results with maximal diversity in the modeled multipath propagation between itself and all CPs individually. Subsequently, this multipath propagation is integrated for generation of multiple modeled received signals ($\{y_{CP,n}[kT_S]\}$ per CP, combined in one set.

Localization System: We employ Qorvo's UWB RF-Chip DW1000. Even though, the firmware offers easy received signal storing for communication between anchor and tag, for efficient storage the DW1000 performs additional processing on the

signal. This processed signal $y_{raw}[mT]$, along with transmission parameters, is transmitted via serial bus. We developed a post-processing algorithm to realistically reconstruct the original measurements, resulting in $y[kT_S]$. This post-processed measurement is compared with the set of modeled received signal $\{y_{CP,n}[kT_S]\}$ utilizing the discrete cross-correlation between the signals to determine the respective correlation coefficient ($\mathbf{d_S}$). We identify the modeled signal that yields the highest correlation coefficient, which serves as an indicator of the corresponding CP as the most probable position estimate $\hat{P}$. The final position estimate $\hat{P}_{MD}$ is derived through a majority rule algorithm: the position estimates from all signal sets are aggregated, and the most frequently occurring position estimate is selected as the final determination. If multiple positions are estimated with equal frequency, the position with the highest correlation coefficient becomes $\hat{P}_{MD}$.

B. Modular Design Structure of the Concept

The conceptualization of a modular architecture necessitates a systematic allocation of individual structural components. Absent this step-wise approach, the envisaged multithreading capability, inclusive of asynchronous module operations, could introduce bottlenecks, ultimately escalating the interval of position updates. Thus, a detailed examination of the proposed modular segmentation is warranted.

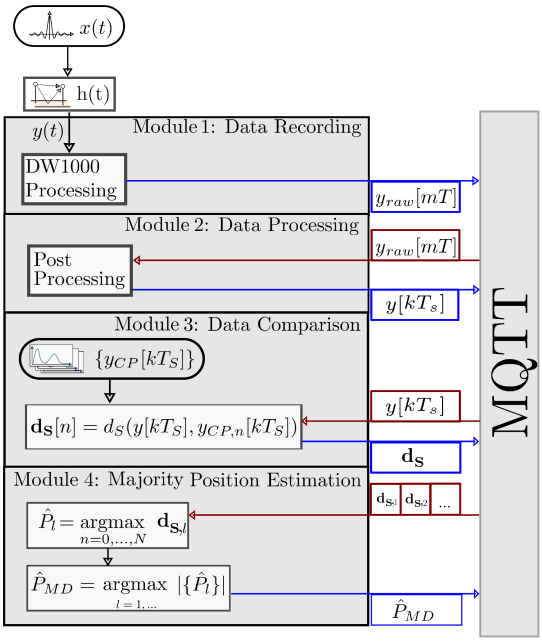

Fig. 1: Schematic representation of the modular architecture.

As illustrated in Figure 1, the architecture is partitioned into four discrete modules. The orchestration of these modules is facilitated by the Message Queuing Telemetry Transport (MQTT) protocol. Within the MQTT system, publishers disseminate data encapsulated in messages, each associated with a uniquely selected topic, to the MQTT broker—a transient data hub. Subscribers, in turn, may elect to receive updates on topics of interest, prompting the immediate relay of pertinent messages upon their availability.

Module 1 is tasked with capturing and relaying the measured signals of the DW1000, to the MQTT broker. Module 2 engages in the reception of these measured signals, undertaking signal post-processing endeavors to restore the signals to their unadulterated state.

Multiple instances of Module 3 receive the processed signal. Each instance is responsible for computing the correlation coefficient between the measured signal and one of the predefined sets of modeled received signals, subsequently outputting the coefficients corresponding to the modeled signal set. In the following, we will have four distinct sets of modeled received signals, resulting in four parallel running instances of Module 3. Each signal consists of $6,000$ floating point samples.

Module 4 consolidates the coefficients from all modeled signal sets. Initially, it deduces the most probable position estimate for each set in a sequential manner. Thereafter, it ascertains the majority-based position estimate, synthesizing the individual position estimates and their associated correlation coefficients.

III. Evaluation of Localization Lag and Update Interval

The efficacy of the modular structure is quantitatively assessed by examining the localization lag and the position update interval. The structure's maximum throughput is constrained by the computation duration of its slowest module.

A. Evaluation Methodology

The modular structure was implemented in Python, and interfaced with an MQTT broker. The hardware running all modules is a Dell Precision 5480 laptop with Intel i7-13800H 13^{th}-Gen processor and 64GB RAM. Each module's computation duration measurement was delimited from message reception to the end, immediately before the results were published. The computation duration was subsequently disseminated via a dedicated MQTT topic. A separate computational entity retrieves the computation duration for each module 5,000 times.In the end, the localization lag results from superposing the module's computation durations. Furthermore, the position update interval is determined, by calculating the temporal interval between consecutive MQTT messages of position estimation.

B. Module's Computation Duration and Localization Lag

Figure 2 illustrates the module's computation duration. Note, that these duration measurements for the four instances of Module 3 are aggregated into a singular histogram for clarity.

In the case of Module 1, approximately 94% of all computation durations are confined to a maximum duration of $250\,\text{ms}$. The distribution of measurement frequencies relative to computation durations exhibits a uniform profile. These computation durations are attributed not to the Python module but to the DW1000 RF chip since the firmware has not been optimized for processing time.Module 2 displays computation

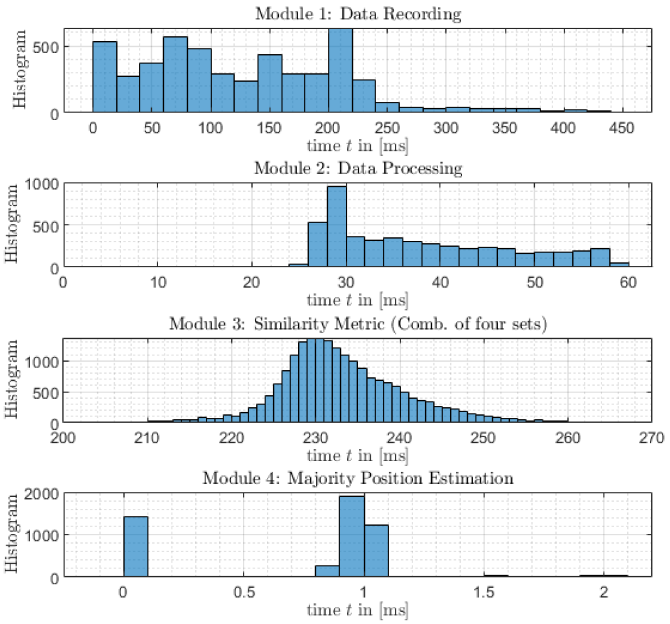

Fig. 2: Computation Durations of Modules 1 through 4, based on a dataset of 5,000 measurements.

durations ranging from 25 ms to 60 ms, with about 30% of these operations completing in under 30 ms. The histogram for measurements exceeding 30 ms approaches a uniform distribution. The computation durations for Module 3 show a slight normal distribution across all four sets, culminating in a mean computation duration denoted by $\mu \approx 233$ ms. So on average, Module 3 has the longest computation duration.Conversely, Module 4 exhibits the lowest computation durations, averaging around 1 ms. Certain intervals are recorded as 0 ms, which may be attributed to the temporal resolution limitations.

When a measurement is recorded, a total localization lag $(250\,\text{ms}+60\,\text{ms}+250\,\text{ms}+1\,\text{ms}) = 561\,\text{ms}$. is expected. In particular, the parallelization of modules 3 to four parallel instances saves time.

C. Position Update Interval

In the scenario where the modules operate in a sequential manner, the initiation of a subsequent position determination is contingent upon the completion of the preceding one, yielding to an approx. position update interval of $(250\,\text{ms}+60\,\text{ms}+4\times 250\,\text{ms}+1\,\text{ms}) = 1311\,\text{ms}$.

Fig. 3 illustrates the empirical data for the overall position update interval across 5,000 measurements. The analysis of the measurements indicates that the maximum duration does not exceed 550 ms translating to a position update rate of 1.82 Hz. A near-linear relationship is observed with the increment of the position update interval, with the frequency of measurements peaking within the range of 400 ms to 450 ms resulting in a position update rate of at least 2.2 Hz in 80% of all measurements.

Employing a modular architecture enables the parallel computation of the single processing steps, diminishing the

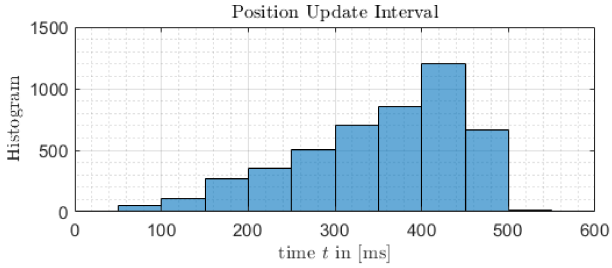

Fig. 3: Overall position update interval for 5,000 measurements.

position update interval by as much as 811 ms, effectively reducing it to 38% of the original duration. Also, the position update rate of 2.2 Hz provides a sufficiently accurate time resolution for tracking stationary tags and tags moving at walking speed.

IV. Conclusion and Future Work

In this work, we introduce and evaluate the modular structured SALOS, our UWB single anchor localization system.

Despite the substantial computational requisites, SALOS has exhibited commendable efficacy. The evaluation yielded a total localization lag at approximately 561 ms. An update interval of less than 500 ms was maintained for approximately 98% of the measurements. Therefore, the system's operational viability is highlighted by its ability to update position estimates swiftly and its closeness in time to real-world events. The attainment results from the architectural design of the constituent modules and the refinement of the underlying algorithms.

The modular structure enables a systematic optimization of SALOS, in which modules can be exchanged, further approaches, such as AI, can be easily tested and evaluated in comparison to the existing solution and different technologies.

Acknowledgments

This publication is a result of the research of the Center of Excellence CoSA. Horst Hellbrück is adjunct professor at the Institute of Telematics of University of Lübeck.

References

[1] A. M. Rahman, T. Li, and Y. Wang, "Recent advances in indoor localization via visible lights: A survey," *Sensors*, vol. 20, no. 5, p. 1382, 2020.

[2] M. Liu, L. Cheng, K. Qian, J. Wang, J. Wang, and Y. Liu, "Indoor acoustic localization: A survey," *Human-centric Computing and Information Sciences*, vol. 10, pp. 1–24, 2020.

[3] S. Leugner and H. Hellbrück, "Lessons learned: Indoor Ultra-Wideband localization systems for an industrial IoT application," Technische Universität Braunschweig, Braunschweig, Tech. Rep., 2018. [Online]. Available: https://www.publikationsserver.tu-braunschweig.de/receive/dbbs_mods_00065900

[4] B. Großwindhager, M. Rath, J. Kulmer, M. S. Bakr, C. A. Boano, K. Witrisal, and K. Römer, "Salma: Uwb-based single-anchor localization system using multipath assistance," in *Proceedings of the 16th ACM Conference on Embedded Networked Sensor Systems*, 2018, pp. 132–144.

[5] S. O. Schmidt, M. Cimdins, F. John, and H. Hellbrück, "Salos—a uwb single-anchor indoor localization system based on a statistical multipath propagation model," *Sensors*, 2024. [Online]. Available: https://www.mdpi.com/1424-8220/24/8/2428

[6] S. O. Schmidt, M. Cimdins, and H. Hellbrück, "On the Effective Length of Channel Impulse Responses in UWB Single Anchor Localization," in *International Conference on Localization and GNSS*, 2019.

On Weight Functions for Multipath-Assisted Radio Tomographic Imaging Algorithms

Marco Cimdins*, Sven Ole Schmidt*, and Horst Hellbrück*
* Technische Hochschule Lübeck - University of Applied Sciences, Germany
Department of Electrical Engineering and Computer Science
Email: {marco.cimdins, sven.ole.schmidt, horst.hellbrueck}@th-luebeck.de

***Abstract*—This paper examines the efficacy of various weight functions in multipath-assisted (MA) device-free localization (DFL) systems that employ radio tomographic imaging (RTI) algorithms for object detection and tracking. RTI algorithms utilize weight functions to correlate alterations in radio signals with the spatial positioning within the target area. We evaluate the standard weight model, which depends solely on the link distance between transmitter and receiver, against three alternative weight functions in a MA DFL context. Our findings reveal that more complex weight functions do not necessarily enhance the localization accuracy in MA RTI. Consequently, future research will focus on exploring different regularization methods.**

***Index Terms*—device-free localization; multipath-assisted radio tomographic imaging; weight functions**

I. Introduction and Related Work

Device-free localization (DFL) systems detect and track objects, such as persons, without necessitating the carriage of any electronic devices. DFL systems measure the perturbations in ambient radio signals within a target area, making them ideal for applications in ambient assisted living and smart home environments. Communication links (e.g., on direct or echo paths) of the multipath-based radio frequency (RF) transmission between transmitter and receiver are influenced by the object. Our DFL approach leverages multipath propagation, by detecting alterations in the link's multipath components (MPCs) from ultra-wideband (UWB) channel impulse responses. Multipath-assisted (MA) radio tomographic imaging (RTI) algorithms transfer changes of the amplitude in an MPC to the target area, creating an *heatmap*. If many altered (echo) signal paths of the MPCs overlap in the target area, objects are detected by searching for local maxima. This paper builds upon our preceding studies [1], [2], and explore enhancement of weight functions for this MA RTI.

The rest of this paper is structured as follows: In Section II, we describe the principles of RTI algorithms and their weight functions. In Section III, we depict our implementation. We evaluate the results of our investigation in Section IV and conclude the results in Section V.

II. Multipath-assisted Radio Tomographic Imaging

In the following, we explain the principles of RTI algorithms. We assume I (echo) signal paths in a target area A. We construct a heatmap for area A, partitioning it into J two-dimensional pixels, each of equal dimensions. At the coordinates of each pixel, the cumulative effect of MPCs superimposes, leading to an aggregate signal attenuation, when an object is nearby. The heatmap's value at any given pixel is determined by the superposed link alteration values at that location. RTI algorithms are based on a mathematically simple linear model [3].

$$\mathbf{z} = \mathbf{W}\mathbf{v} + \mathbf{n}, \tag{1}$$

where $\mathbf{n}$ is normally distributed noise of dimension I. This heatmap is encapsulated by the vector $\mathbf{v}$, which comprises J elements. To quantify the impact of each MPC on individual pixels, we employ a matrix $\mathbf{W}$, dimensioned $I \times J$, which allocates weight w_{ij} to the heatmap's values. Consequently, the measurement vector denoted as $\mathbf{z}$ and also spanning I elements, is derived.

In previous works [1], [2], we deployed a simple weight function that determines the weight w_{ij} of each signal path i and each pixel j. The weight function is described by the following equation [3]:

$$w_{ij} = \begin{cases} 1/\sqrt{d_i} & \text{if } d_{ij}(1) + d_{ij}(2) < d_i + \gamma_{\text{RTI}} \\ 0 & \text{otherwise} \end{cases}, \tag{2}$$

where $d_{ij}(1) + d_{ij}(2)$ is the distance from radio node 1 to radio node 2 on the i-th signal path to the center of pixel j. d_i is the distance of the i-th signal path and γ_{RTI} is a tuning parameter in $\mathbb{R}^+$[3]. In the following, we refer to this weight function as our standard.

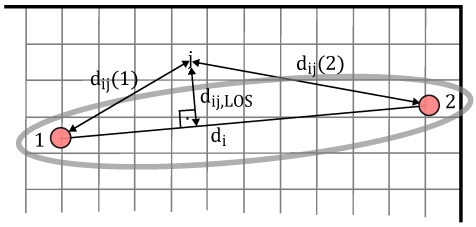

Fig. 1: Geometry and visualization of the elliptical weight function.

Figure 1 shows the geometry of the weight function. If the center of the pixel j is within an ellipse with the radio nodes in their focii, then the pixel is assigned the weight $w_{ij} = 1/\sqrt{(d_i)}$, otherwise, the weight is $w_{ij} = 0$. An object outside the signal path does not affect the heatmap. The tuning parameter γ_{RTI} controls the width of the ellipse.

A disadvantage of this standard weight function is, that the influence of an object is solely based on the length of the direct signal path, which is not representing reality well. Therefore, in this paper, we investigate and compare other weight functions that were proposed in the past and shown promising results, although they have not been tested for MA RTI. In [4], the authors proposed a distance-based weight function that takes into account, that objects in the middle of the direct path have a higher alteration of the radio signal than at the edges of an ellipse between the transmitter and the receiver [4]:

$$w_{ij} = \begin{cases} e^{-d_{ij,\text{LOS}}} & \text{if } d_{ij}(1) + d_{ij}(2) < d_i + \gamma_{\text{RTI}} \\ 0 & \text{otherwise} \end{cases}, \tag{3}$$

where $d_{ij,\text{LOS}}$ is the distance from the pixel to the direct path.

In [5], the authors propose a second distance-based weight function that considers the position of the object. An object close to the radio nodes creates a bigger effect on the MPC.

$$w_{ij} = \begin{cases} e^{-\min(d_{ij}(1), d_{ij}(2))} & \text{if } d_{ij}(1) + d_{ij}(2) < d_i + \gamma_{\text{RTI}} \\ 0 & \text{otherwise} \end{cases}, \tag{4}$$

Another weight model was proposed in [6]. It differentiates, whether the object is present in the direct path and, therefore causes non-line-of-sight conditions or not. We will call this weight function communication-link.

$$w_{ij} = \begin{cases} 1/d_i(k_1 + \max\left(d_{ij}(1), d_{ij}(2)\right) \\ \text{if } d_{ij}(1) + d_{ij}(2) < d_i + \gamma_{\text{RTI}}, d_{ij}(1) + d_{ij}(2) \neq d_i \\ 1/d_i(k_2 + \max\left(d_{ij}(1), d_{ij}(2)\right) \\ \text{if } d_{ij}(1) + d_{ij}(2) < d_i + \gamma_{\text{RTI}}, d_{ij}(1) + d_{ij}(2) = d_i \\ 0 \qquad \text{otherwise} \end{cases} \tag{5}$$

where $k_2 = k_1 + \beta$, with k_1 empirically determined with 2 and β empirically determined with 0.5 [6].

We solve (1), by utilizing ℓ_2-minimization:

$$\hat{\mathbf{v}}_{LS} = \underbrace{\arg\min}_{\tilde{\mathbf{v}} \in \mathbb{C}^J} ||\mathbf{W}\tilde{\mathbf{v}} - \mathbf{z}||_2^2, \tag{6}$$

this leads to the well-known solution [3]:

$$\hat{\mathbf{v}}_{LS} = \mathbf{W}^{\dagger}\mathbf{z}, \tag{7}$$

where $\mathbf{W}^{\dagger}$ is the Moore-Penrose pseudo-inverse of $\mathbf{W}$. Each weight w_{ij} for each signal path i and each pixel j is calculated according to the respective weight function (2), (3), (4), (5).

As device-free localization is an ill-posed inverse problem, the solution requires regularization of the pseudo inverses using the covariance matrix $\mathbf{C}_v$ of v $\mathbf{C}_v$ weighted by the regularization parameter σ_J^{-2} [3].

$$\mathbf{C}_v[k,l] = \sigma_v^2 e^{-d_{kl}/\delta_c}. \tag{8}$$

d_{kl} is the distance from pixel k to l, δ_c is a distance constant and σ_v^2 is the pixel variance of the estimation error. Exponential covariance are a common approximation for a spatial attenuation modeled as a Poisson process [3].

If the covariance matrix is included in the calculation of the pseudo inverses, (7) becomes [3]:

$$\hat{\mathbf{v}} = \left(\mathbf{W}^T\mathbf{W} + \mathbf{C}_v^{-1}\sigma_J^2\right)^{-1}\mathbf{W}^T\mathbf{z} \tag{9}$$

We define the input vector $z_i = \mathbf{z}[i]$ for the i-th MPC on the (echo) signal path as follows:

$$z_i = |P_{i,\text{obs}} - P_{i,\text{idle}}|, \tag{10}$$

Here, $P_{i,\cdot}$ is the signal power of the observed MPC and the MPC measured in idle mode at the time τ_i. The stronger the object influences the amplitude of the MPC on the (echo) signal path compared to the idle path, the higher the influence for the MA RTI system.

After calculation of the heatmap $\hat{\mathbf{v}}$, we determine the position of the object $\hat{\mathbf{r}}_O$ by searching for the maximum value in $\hat{\mathbf{v}}$: $\hat{\mathbf{r}}_O = \text{Pos}\left(\arg\max_{j \in \{0 \ldots J-1\}} \hat{v}_j\right)$, where the operator $\text{Pos}(j)$ returns the position vector of the jth pixel.

In addition to the previously described weight functions, we investigate a combined weight function: For this, we first identify the maximum value, denoted as v_j, across all measurements and weight functions. Subsequently, we normalize the heatmaps, represented by $\hat{\mathbf{v}}$, to a range between 0 and 1. During each measurement, we evaluate the normalized peak values across the heatmaps. The highest of these values, along with its associated position vector $\hat{\mathbf{r}}_O$, is then selected to serve as the estimated position.

III. Implementation

For evaluation, we used the test setup and utilized the dataset from [2]. Measurements were conducted in a standard office environment measuring approximately $6\,m \times 7\,\text{m}$. We chose 53 reference positions throughout the room, maintaining an approximate distance of $0.5\,\text{m}$ between each point. The experimental setup included four radio nodes equipped with Qorvo's DWM1000 ultra-wideband (UWB) radio modules. These nodes engaged in message exchanges over IEEE 802.15.4a channel 3, operating at a center frequency of 4.4928 GHz and a bandwidth of 499.2 MHz. Upon receiving a message, each node captured the UWB channel impulse response (CIR) together with the required meta data to process the CIR and extract the magnitudes of each MPC [2]. The radio nodes were strategically positioned at a height of 1.418 m, equating to half the room's height, to optimize the spatial sampling of the radio signals.

To compare the different weight functions, we used the same parameters: The pixel width of the target area is $0.1\,\text{m}$ [3]; the width of the weighting ellipse $\gamma_{\text{RTI}} = 0.01$ m [3]; the pixel variance $\sigma_v^2 = 0.5\,\text{dB}^2$ [7]; the regularization parameter $\sigma_J^2 = 0.5\,\text{dB}^2$; the pixel correlation constant $\delta_c = 0.5\,\text{m}$ [3].

IV. Evaluation

Figure 2 presents exemplary outcomes of the study. The white cross marks the actual position of a person, denoted by $\hat{\mathbf{r}}_\mathbf{O}$, within the designated area, while the red cross signifies

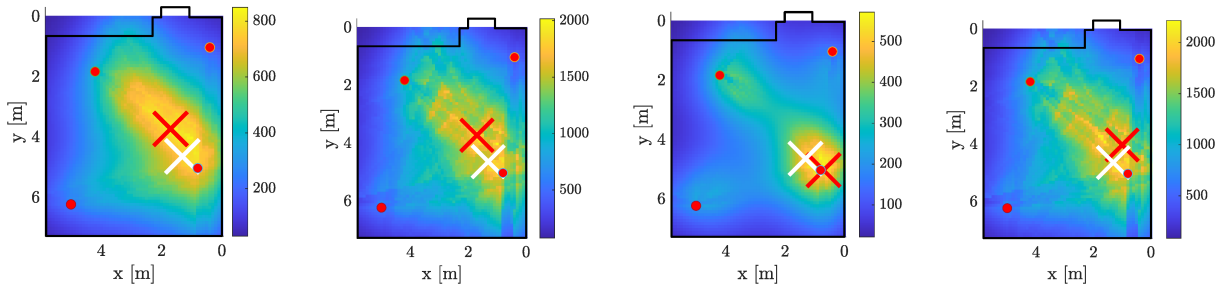

(a) Standard. (b) Distance-based-1. (c) Distance-based-2. (d) Communication-Link.

Fig. 2: Exemplary results of the heatmap $\hat{\mathbf{v}}$ for the different weight functions.

the estimated location, $\mathbf{r_O}$. The red dots symbolize the radio nodes. The heatmap's coloration, a product of the MA RTI algorithm employing various weight functions, indicates the likelihood of the object's proximity, with yellow suggesting a high probability. As the weight functions assign different weights to each pixel, the color scale differs for each figure. The conventional weight function, as shown in Figure 2a, yields a broad area where the object might be situated, proving effective for central positions within the area. Conversely, the second distance-based weight function assigns greater significance to positions nearer to the radio nodes, enhancing accuracy for objects located near these nodes.

To evaluate the localization accuracy, we calculate the Euclidean distance: $e = ||\hat{\mathbf{r}}_\mathbf{O} - \mathbf{r_O}||$, where $||\cdot||$ is the Euclidean distance, $\hat{\mathbf{r}}_\mathbf{O}$ the estimated position, and $\mathbf{r_O}$ the ground truth position of the object.

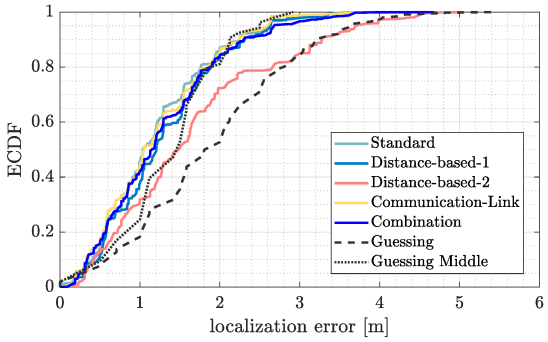

Fig. 3: ECDF results for the different weight functions.

Figure 3 presents the empirical cumulative distribution functions (ECDFs) for various weighting functions. For benchmarking purposes, we compare these ECDFs against two scenarios: one where all reference positions are considered (represented by a gray dashed line), and another where only the central reference position is assumed (indicated by a gray dotted line). At the 50th percentile, the standard weight function exhibits a localization error of 1.04 m, closely followed by the communication-link function at 1.05 m. The proposed combination yields an error of 1.15 m, while the first and second distance-based functions result in errors of 1.2 m and 1.49 m, respectively. At the 80th percentile, the errors associated with the weight functions are 1.76 m, 1.86 m, 1.9 m (for both the proposed combination and the first distance-based model), and 2.69 m, in the same sequence as before. Despite these figures, MA RTI outperforms the baseline strategy of random guessing across all positions, which incurs errors of 1.80 m and 2.83 m at the 50th and 80th percentiles, respectively. Moreover, consistently guessing the central position results in lower errors of 1.45 m and 1.84 m for the respective percentiles. As the other weight functions do not yield better results, we continue using the standard weight function for future works.

V. Conclusion and Future Work

In this paper, we explore a variety of weight functions within the context of MA RTI. Our findings suggest that increasing the complexity of these weight functions does not necessarily lead to better localization accuracy in MA RTI scenarios.

In the future, our we will focus on diverse regularization techniques, an area not covered in the current paper. Additionally, we plan to delve into the automated identification of MPCs that significantly influenced by the object.

Acknowledgments

This publication is a result of the research of the Center of Excellence CoSA.

References

[1] M. Cimdins, S. O. Schmidt, P. Bartmann, and H. Hellbrück, "Exploiting Ultra-Wideband Channel Impulse Responses for Device-Free Localization," *Sensors*, vol. 22, no. 16, 2022. [Online]. Available: https://www.mdpi.com/1424-8220/22/16/6255

[2] M. Cimdins, S. O. Schmidt, F. John, M. Constapel, and H. Hellbrück, "MA-RTI: Design and Evaluation of a Real-World Multipath-Assisted Device-Free Localization System," *Sensors*, vol. 23, no. 4, 2023. [Online]. Available: https://www.mdpi.com/1424-8220/23/4/2199

[3] J. Wilson and N. Patwari, "Radio tomographic imaging with wireless networks," *IEEE Transactions on Mobile Computing*, vol. 9, no. 5, pp. 621–632, 2010.

[4] C. Zhu and Y. Chen, "Distance attenuation-based elliptical weighting-g model in radio tomography imaging," *IEEE Access*, vol. 6, pp. 34 691–34 695, 2018.

[5] G. Li and Q. Lei, "Device-free localization using enhanced channel selection and a distance-based elliptical model," *IEEE Access*, vol. 10, pp. 129 531–129 538, 2022.

[6] Q. Lei, H. Zhang, H. Sun, and L. Tang, "A new elliptical model for device-free localization," *Sensors*, vol. 16, no. 4, p. 577, 2016.

[7] M. Cimdins, S. O. Schmidt, and H. Hellbrück, "MAMPI-UWB—Multipath-Assisted Device-Free Localization with Magnitude and Phase Information with UWB Transceivers," *Sensors*, vol. 20, no. 24, 2020. [Online]. Available: https://www.mdpi.com/1424-8220/20/24/7090

On Options for the Design of Radio Frequency-based Positioning Systems

Marco Gunia* and Frank Ellinger*†
*Chair for Circuit Design and Network Theory (CCN) and
†Centre for Tactile Internet with Human-in-the-Loop (CeTI)
Technische Universität Dresden, 01062 Dresden
Email: marco.gunia@tu-dresden.de

***Abstract*—This paper examines various alternatives for the design of radio frequency-based positioning systems. In addition to the potential signals used, such settings differ in the methods employed to derive the characteristic parameter like distance or incident angle. Multiple such measurements are combined into a raw position by means of a selected positioning algorithm. Due to measurement errors, these position estimates are subject to deviations which are eliminated via a chosen tracking filter. Finally, the results of several of these systems can be merged at different levels. In addition to highlighting all these options, the paper also analyses the advantages and disadvantages of the individual alternatives and aims to provide designers of future systems with assistance in specification and implementation.**

Keywords*—Positioning, Localization, Design, Choices, Options, Alternatives, Distance, Range, Incident angle, Received signal strength, Positioning algorithms, Least squares, Maximum-likelihood, Iterative, Kalman filter, Particle filter, Data level fusion, System level fusion

I. Introduction

Designers are often overwhelmed by the different alternatives and their impact on performance when analyzing and implementing Radio Frequency (RF) -based positioning systems. This is usually accompanied by a lack of knowledge of the pros and cons of individual approaches, with cost and accuracy often being the most important Figure of Merits (FoM). This paper attempts a rough classification of the effects of choices at different level in the design process on the overall performance. First, various underlying signals are presented. Building on this, the paper evaluates several methods for extracting the two parameters range or incident angle from the signal characteristics. By using multiple independent parameter measurements, it is possible to determine the position, whereby a designer can choose between simple geometric and complex non-geometric variants. The resulting estimate is not the true value due to the underlying error-prone parameter measurement process. Tracking filters with different properties are applied to smooth successive estimates and reduce these observation errors. If multiple systems are available at the same time, the data can be fused with the goal of improving the final result. In all of the aforementioned aspects, the paper examines possible options and presents their advantages and disadvantages.

II. Design choices

In order to consider the following explanations in a common context, we assume that a Mobile Station (MS) is localized via stationary Base Stations (BS) of known position. Table I contains a summary of all variations described below, together with their pros and cons.

A. Signals

Positioning systems differ in terms of whether the underlying hardware and associated RF signals are specially tailored for localization or whether existing communication hardware is adapted [1]. Typical representatives of the first category are radar systems, e.g. Frequency Modulated Continuous Wave (FMCW) or Ultra-WideBand (UWB) [2]. Furthermore, these include Global Navigation Satellite Systems (GNSS) like the Global Positioning System (GPS). The second category comprises the use of Wireless Local Area Networks (WLAN), Bluetooth and ZigBee, where usually Commercial Off The Shelf (COTS) components are available. Typically, proprietary positioning systems are more expensive to design, but often achieve significantly better accuracy [1]. In addition, Radio Frequency IDentification (RFID) is also sometimes employed to determine the position. Due to its typically very short range, the known position of the base station is used as an estimate [3]. Last but not least, the radio cells for mobile communication can be evaluated to obtain a rough approximation [3]. A classification of typical signal protocols, divided into whether they are mainly applied indoor or outdoor, is shown in Fig. 1.

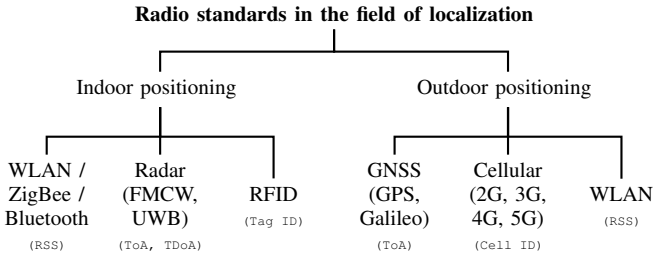

Fig. 1. Classification with regard to the operation of different radio standards

B. Method

Irrespective of the signal protocols, radio frequency signals differ on the basis of various characteristics. Firstly, the measurement of the signal propagation time, abbreviated as Time of Arrival (ToA), between BS and MS is conceivable. This requires synchronization of the clocks of all stations [3]. If only the synchronization of all BS is possible, then the use of the differences in signal propagation time, abbreviated as Time Difference of Arrival (TDoA), is an option [4]. In addition

to synchronization, both variants place high demands on the hardware, as the very short signal propagation times must be measured. This requires fast clocked counters [5]. One way of limiting hardware effort is to draw indirect conclusions from the Received Signal Strength (RSS). Various channel models proposed in the literature describe the dependence of that characteristic on the distance. Well known is the log-normal model [6]. All of the aforementioned concepts allow conclusions to be drawn about the distance parameter.

Alternatively, it is possible to derive the incident angle, e.g. by determining the phase shift of a signal when it is received at multiple antennas. Approaches employing that parameter are denoted by Angle of Arrival (AoA). Advantageous is that in general a two-dimensional position can already be inferred from the intersection of the incident angles of signals emerging from two BS, whereas at least three observations are required for distance measurements [1]. The disadvantage is that, depending on the design, this requires beam steering or alternatively the use of multiple antennas [7]. In practice, computationally complex algorithms for spectrum analysis such as MuSiC ([8]) or ESPRIT ([9]) are often required.

C. Positioning

Regardless if applying ranges or incident angles, a number of different algorithms are proposed in the literature, which infer the position by taking into account parameter measurements between multiple BS and the MS. A detailed description is found in [1]. The approaches can be roughly divided into geometric and non-geometric concepts. In the first case, exact measured values are not required. Instead, the estimation is largely based on the arrangement of the BS. Such an example employing ranges is *Proximity* [10], where the estimate is the BS location for which the measured distance is the smallest.

In contrast, non-geometric methods require exact parameter measurements. The direct calculation via the system equations is practically not expedient. Because on the one hand, the measured values are subject to errors, which means that no unique solution can be found. On the other hand, redundant measurements (e.g. for additional existing BS) cannot be included. Instead, practical methods use either the solution of a *least square* matrix equation system [11] or the minimization of an error function. Due to the direct formulation of this error, more accurate methods can be expected for the second case [6]. These include *Iterative* ([11]) or *Maximum Likelihood* ([12]). As example, the following equation shows the error function

$$\tilde{\varepsilon} = \sum_{n=1}^{N} \left[\sqrt{(x_n - x)^2 + (y_n - y)^2} - \tilde{d}_{n\leftrightarrow\bullet} \right]^2 \qquad (1)$$

for *Iterative* assuming distance measurements $\tilde{d}_{n\leftrightarrow\bullet}$ to the N BS, located at position (x_n, y_n). For *Maximum Likelihood*, where the inverse of the statistical distribution density function serves as a formula for the error, the underlying measurement error distribution is required. If known, optimal results can be achieved. A disadvantage of both is that error minimisation is carried out continuously by gradient descent until the error is below a certain threshold [11]. On the one hand, this requires high computing power. On the other hand, the solution can be trapped in local minima and not in the global one [6].

A completely alternative concept not requiring any BS is operating an Inertial Navigation System (INS). Here, acceleration sensors and gyroscopes are utilized to deduce the change in the current position in relation to a starting point [13].

It is only mentioned in passing that, based on the inclusion in the system equations, positioning is also conceivable directly by means of tracking filters, which are described next.

D. Tracking filters

The goal of tracking filters is to smooth the measured values by eliminating the unknown observation error. A simple option is a moving average filter, in which the sliding mean value of the last N measurements $x_{k-N+1}, x_{k-N+2}, \cdots, x_k$ is used as an estimate at time step k according to [14]

$$\begin{aligned} \overline{x}_k &= \frac{x_{k-N+1} + x_{k-N+2} + \cdots + x_k}{N} \\ &= \overline{x}_{k-1} + \frac{x_k - x_{k-N}}{N} \end{aligned} \qquad (2)$$

where the recursive expression in the last line follows from introducing the moving average value $\overline{x}_{k-1}$ from the last time step into the first formula [14]. The advantage is the low calculation effort. In contrast, there is the disadvantage of having the observations of all previous N time steps being weighted equally, even though the true output has evolved.

One way to achieve a stronger weighting on the last measurements is by means of a low-pass filter. It reads [14]

$$\overline{x}_k = \alpha\, \overline{x}_{k-1} + (1 - \alpha)\; x_k \quad \text{with } \alpha \in [0, 1] \qquad (3)$$

However, the problem here is the fixed parameter α, which indicates the ratio of the new value to the current estimate.

Kalman Filters (KF), on the other hand, represent an extension in that this parameter, which is now referred to as Kalman gain, is selected variably depending on the statistical values. Hereby, the current measured variable is compared with the respective value to be expected from the system. Mathematically, KF are optimal in terms of calculating the minimum variance estimate, if the observed system is linear, the expected value and associated covariance of the initial value, being a random variable, are known and the observation noise and process noise[1] are Gaussian random processes with symmetrical positive semi-definite covariance matrices. In addition, the initial state, process noise and observation noise must be mutually uncorrelated [15], [16]. In practice, not all conditions are typically fulfilled in this respect, so that the estimated value then deviates from the optimum result. Compared to the previous approach, the calculation effort is higher due to the matrix operations involved.

In the case of non-linearity of the observed system, linearisation of the system in each time step is conceivable before applying the KF. However, this approach, known as the Extended Kalman Filter (EKF), only offers the optimal solution with regard to the linearised system and not the original system. A method that dispenses with linearisation is the Unscented Kalman Filter (UKF), in which the statistical variables are reconstructed taking the functional values of the non-linear functions for a few selected points [14].

[1] Process noise is usually not present in positioning systems.

The consideration of few selected points serves to avoid a complex Monte Carlo simulation. Nevertheless, such a concept is the Particle Filter (PF). It is based on initial generating multiple particles, which represent random samples in the state space. Subsequently, their propagation is simulated using the system equations, whereby less probable elements are discarded and the remaining ones are pursued further [17].

E. Fusion

In addition to individual systems, hybrid systems are also proposed in the literature. These differ in terms of whether a single system is duplicated (e.g. installation of the same system in several rooms) or whether hybrid hardware is applied. Duplication saves design costs, but with true hybrid hardware there is the possibility that the weaknesses of one system are compensated for by the strengths of the other. Irrespective of this, it is possible to use one system at a time or to employ them simultaneously. In either case, the systems generate measurement data, which can be combined into a final position estimate either at data level or system level. In the former case, the parameter measurements (e.g. the determined distances or angles of incidence) are combined in a large system equation. In the latter case, however, the individual systems determine position estimates independently, which are then merged into a final result by means of weighting or filters, e.g. by taking into account the covariances of the measurements [1]. The disadvantage for the system-level fusion is that a position estimate must be available for each individual system. However, if there are insufficient measurements for a system to draw conclusions about a unique position, e.g. if there are too few distance measurements, then it may be possible to estimate the position using fusion at data level, taking into account the alternative parameter measurements.

TABLE I. DESIGN OPTIONS FOR RF-BASED POSITIONING

Approach	Advantage	Disadvantage
Signals		
Communication	• COTS available. • Inexpensive.	• Configuration fixed (e.g. low accuracy or range).
Proprietary	• Arbitrary configuration (e.g. accuracy or range).	• Extra hardware design. • Costly.
Method		
ToA	• High accuracy.	• Sync. between BS and MS.
TDoA	• Moderate accuracy.	• Sync. between BS.
RSS	• Inexpensive.	• Low accuracy.
AoA	• Less BS necessary.	• High hardware efforts. • Computationally complex.
Positioning		
Geometric	• Easy set-up.	• Very low accuracy (depends on BS arrangement).
Least squares	• Computationally moderate.	• Indirect minimization of error function.
Iterative	• Direct minimization of error function.	• Computationally complex.
Maximum-likelihood	• Optimal solution.	• Distribution density function required. • Computationally complex.
Tracking filter		
Moving average	• Computationally simple.	• Equal weighting of measurements.
Low-pass	• Computationally simple. • Non-equal weighting.	• Fixed weighing of last measurement.
KF	• Optimal solution.	• Only linear systems. • Only Gaussian noise. • Only mutually uncorrelated.
EKF	• Non-linear system support.	• Optimal solution not guaranteed.
UCF	• Non-linear system support.	• Optimal solution not guaranteed.
PF	• Arbitrary conditions.	• Computationally complex.
Fusion: Duplication vs hybrid hardware		
Duplication	• Low efforts.	• No mutual supplementation.
Hybrid	• Mutual supplementation.	• High efforts.
Fusion: Data-level vs. system-level		
Data-level	• Position calculation even if data is not sufficient for individual systems.	• No statistical weighting.
System-level	• Statistical weighting.	• Position calculation even if data is not sufficient for individual systems.

III. CONCLUSION AND FURTHER WORK

The paper analysed several alternatives for the design of positioning systems, from the underlying RF signal to the extracted parameters, the positioning approach, the filter algorithms and fusing methods. The pros and cons of the choices, which relate to FOM like accuracy and costs, were outlined. Together, this offers future designers the opportunity to select promising options at an early stage and thus support both the specification and implementation of such systems.

ACKNOWLEDGMENT

We acknowledge the cooperation with the Centre for Tactile Internet with Human-in-the-Loop (CeTi), a Cluster of Excellence at TU Dresden and with the BMBF funded project 6G-life (project ID: 16KISK001K).

REFERENCES

[1] M. Gunia, "Analyse und Design verschiedenartiger Positionierungssysteme, deren Zusammenführung sowie Vorhersage zukünftiger Positionen und Trajektorien," Dissertation, Technische Universität Dresden, 2023, pp. 1–371.

[2] M. Gunia, F. Protze, N. Joram, and F. Ellinger, "Setting up an ultra-wideband positioning system using off-the-shelf components," in *Proc. 13th Work. Positioning, Navig. Commun. (WPNC'16)*, Oct. 2016, pp. 1–6.

[3] H. Liu, H. Darabi, P. Banerjee, and J. Liu, "Survey of wireless indoor positioning techniques and systems," *IEEE Trans. Syst., Man, Cybern., Part C (Applications and Reviews)*, vol. 37, no. 6, pp. 1067–1080, Nov. 2007, ISSN: 1094-6977.

[4] Y. Qi and H. Kobayashi, "On relation among time delay and signal strength based geolocation methods," in *Proc. IEEE Global Telecommun. Conf. (GLOBECOM'03)*, San Francisco, CA, USA: IEEE, 2003, pp. 4079–4083.

[5] Z. Sahinoglu and S. Gezici, "Ranging in the ieee 802.15.4a standard," in *2006 IEEE Annual Wireless and Microwave Technology Conf.*, Dec. 2006, pp. 1–5.

[6] P. Tarrio, A. M. Bernardos, and J. R. Casar, "Weighted least squares techniques for improved received signal strength based localization," *Sensors 2011*, pp. 8569–8592, 2011.

[7] M. Gunia, A. Zinke, N. Joram, and F. Ellinger, "Analysis and design of a MuSiC-based angle of arrival positioning system," *ACM Trans. Sen. Netw.*, Jan. 2023, Gerade angenommen, ISSN: 1550-4859. [Online]. Available: https://doi.org/10.1145/3577927.

[8] R. Schmidt, "Multiple emitter location and signal parameter estimation," *IEEE Transactions on Antennas and Propagation*, vol. 34, no. 3, pp. 276–280, Mar. 1986, ISSN: 0018-926X.

[9] R. Roy and T. Kailath, "Esprit-estimation of signal parameters via rotational invariance techniques," *IEEE Transactions on Acoustics, Speech, and Signal Processing*, vol. 37, no. 7, pp. 984–995, Jul. 1989, ISSN: 0096-3518.

[10] N. Patwari and A. O. H. III, "Using proximity and quantized rss for sensor localization in wireless networks," *Proc. 2nd ACM Int. Conf. Wireless Sensor Networks and Applications (WSNA 03)*, pp. 20–29, 2003.

[11] P. Tarrio, A. M. Bernardos, and J. R. Casar, "An rss localization method based on parametric channel models," in *2007 Int. Conf. Sensor Technol. Appl. (SENSORCOMM 2007)*, 2007, pp. 265–270.

[12] M. Laaraiedh, L. Yu, S. Avrillon, and B. Uguen, "Comparison of hybrid localization schemes using rssi, toa, and tdoa," in *17th Eur. Wireless 2011 - Sustain. Wireless Technol.*, 2011, pp. 1–5.

[13] M. Gunia, Y. Wu, N. Joram, and F. Ellinger, "Building up an inertial navigation system using standard mobile devices," *J. Elect. Eng.*, vol. 5, pp. 299–320, 2017.

[14] P. Kim and L. Huh, *Kalman Filter for Beginners: with MATLAB Examples*. CreateSpace Independent Publishing Platform, 2011.

[15] K. Brammer and G. Siffling, *Stochastische Grundlagen des Kalman-Bucy-Filters: Wahrscheinlichtkeitsrechung und Zufallsprozesse*, 3. verb. Aufl. Oldenbourg Wissenschaftsverlag, 1990.

[16] K. Brammer and G. Siffling, *Kalman-Bucy-Filter: Deterministische Beobachtung und stochastische Filterung*, 4. verb. Aufl. de Gruyter, 1993.

[17] M. d. T. Peral, F. G. Bravo, and A. MartinhoVale, "State variables estimation using particle filter: Experimental comparison with kalman filter," in *2007 IEEE International Symposium on Intelligent Signal Processing*, 2007, pp. 1–6.

Indoor Localization Using Commercially-off-the-Shelf-Available Gas Sensors

Marco Cimdins*, Domenic Hampf*, Sebastian Hauschild*, and Horst Hellbrück*
* Technische Hochschule Lübeck - University of Applied Sciences, Germany
Email: {marco.cimdins, domenic.hampf, sebastian.hauschild, horst.hellbrueck}@th-luebeck.de

***Abstract*—This paper presents the application of commercially-off-the-shelf (COTS)-available gas sensors for monitoring indoor air quality and proposes their integration into an electronic nose system for indoor localization. The objective is to accurately identify specific locations within various rooms of a building. To achieve this, we employ a nearest neighbor algorithm for fingerprinting. Our initial results are promising, demonstrating the system's ability to distinguish between corridors and distinct rooms or laboratories. However, to advance towards a fully operational prototype, further research is necessary. This includes the development of more advanced signal processing techniques and the extraction of detailed information, such as deciphering the unique gas composition signatures of different rooms.**

***Index Terms*—fingerprinting, indoor localization, gas sensor**

I. Introduction and Related Work

Low-cost air quality sensors in buildings are commonly deployed for monitoring of indoor environments [1]. Our idea to is to build a mobile electronic nose, equipped with commercially off-the-shelf (COTS)-available gas sensors for indoor localization. Such sensors can help identify the type of room, thus narrowing down the position within a building.

Previous studies explored the concept of a virtual nose for person localization [2], as well as the detection and localization of gas leaks [3]. Our research takes inspiration from these works, particularly the use of aroma fingerprints for indoor localization, as detailed by Müller et al. [4]. In their study, a handheld chemical detector from Environics, utilizing ion mobility spectrometry, was employed. The k-nearest neighbour algorithm facilitated the classification of various locations, such as offices, coffee rooms, open spaces, and corridors, based on their distinct olfactory profiles.

In the paper, we deploy a COTS-available gas sensor capable of detecting four distinct gases. We aim to determine whether varying operational modes can yield sufficient data to accurately localize a room. The potential applications of this technology are vast, including its integration into indoor localization systems to provide supplementary information that could differentiate between floors or specific rooms.

Section II outlines the proposed localization algorithm, while Section III details the hardware and measurement setup. Section IV presents and discusses our preliminary findings. Finally, Section V provides a summary and the implications of our research.

II. Localization Algorithm

In this paper, we propose to utilize the nearest neighbor algorithm to perform fingerprinting for indoor localization [5]. Therefore, we define J positions within the target area, whereby each position is described by its position index $j = 1, ..., J$. Each position in the target area is described by its reference feature vector $\mathbf{r}_{j,r}$, which contains the reference measurement values at the j-th position.

To determine the position, the observation feature vector $\mathbf{r}_{j,o}$ is required. This is recorded with an observation measurement at the j-th position. For localization, a suitable metric is used to calculate the distance between all reference feature vectors $\mathbf{r}_{j,r}$ and the observation feature vector $\mathbf{r}_{j,o}$. In this case, the $\ell 1$-distance serves as an example of a distance metric between two vectors: $d_{\ell 1}(\mathbf{r}_{j,o}, \mathbf{r}_{j,r}) = \sum_{n=1}^{N} |\mathbf{r}_{j,o}[n] - \mathbf{r}_{j,r}[n]|$

The most probable position $\hat{\mathbf{r}}$ is then determined by determining the minimum, here using the example of the $\ell 1$ norm:

$$\hat{\mathbf{r}} = \underbrace{\arg\min}_{d_{\ell 1}(\mathbf{r}_{j,o}, \mathbf{r}_{j,r})} \left(\mathbf{d}_{\ell 1}(\mathbf{r}_{j,o}, \mathbf{r}_{j,r})\right) \tag{1}$$

III. Implementation

In this section, we describe the measurement setup and the measurement mode.

The sensor system consists of a sensor chamber equipped with an integrated Grove Multichannel Gas Sensor V2, which is COTS-available for approx. 40 €. The sensor is a combination of four MEMS sensors with different cross-sensitivities. The main sensitivities of the sensors are as follows: nitrogen dioxide (NO2) for the GM-102B, ethanol (C2H5OH) for the GM-302B, volatile organic compounds (VOC) for the GM-502B, and carbon monoxide (CO) for the GM-702B. The sensor values are processed on the board by a microcontroller STM32F030 with a 12-bit ADC and output the raw data that represents changes via an I2C interface. The sensor chamber is connected via silicone hoses to a pump, which is controlled by a Grove MOSFET CJQ4435. The control of the MOSFET for the pump and the data acquisition of the sensor values via I2C is carried out by the WIO terminal with the help of a 32-bit ARM Microchip microcontroller ATSAMD51. The WIO terminal supplies the MEMS sensors in the chamber with a voltage of 3.3 V and the control and load circuit of the MOSFET for pump control with 5 V. For forwarding the data for later processing, a UART connection is established over the USB-C cable with 9600 baud using the EDGE Impulse CLI. The sensor

values are recorded at a sampling rate of 10 Hz. The start of the recording is done via the web interface of EDGE Impulse. Figure 1 shows a picture of the test setup.

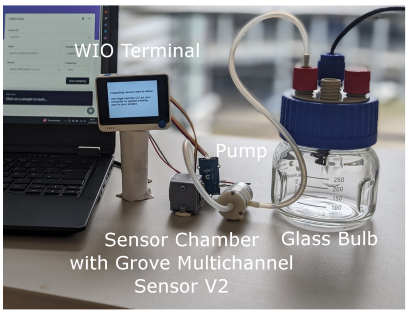

Fig. 1: Test Setup. The air flows from the right-hand side through the glass bulb towards the sensor chamber.

For our preliminary analysis, we conducted tests at three strategic reference points as depicted in Figure 2. Position 01 is situated at the terminus of a corridor, position 02 is located within a standard office space, and position 03 is set in a conventional laboratory setting.

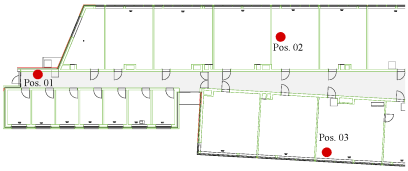

Fig. 2: Floorplan with reference positions.

Given the absence of additional detectable chemicals in an office setting, we expect only minimal fluctuations in sensor readings. The electronic nose faces the challenge of discerning subtle variations in the concentrations of NO2, C2H5OH, VOCs, and CO across different positions.

Initial tests revealed that the sensor requires an extended preheating period; sensor readings continued to drift even after 2 h of operation. To address this, we implemented a pump system that maintains a steady airflow of 1.8 l/min through the sensor chamber. Air is first directed through a glass bulb before entering the sensor chamber, which isolates the sensor from ambient air currents and the movement of individuals, ensuring consistency in the absence of active pumping. Previous research demonstrated that the repeated process of pumping gases in and out significantly enhances the accuracy of substance classifications [6]. To assess the sensor's responsiveness to the presence or absence of new air, we conducted measurements using our test setup for 300 s under a specific operational mode (refer to Figure 3 for details).

The operational mode is designed to capture air within the glass bulb at a specific location, which is then analyzed by the sensor. We hypothesize that the variations in gas concentrations at distinct positions will induce significant changes in the sensor's dynamic readings, thereby enabling accurate localization.

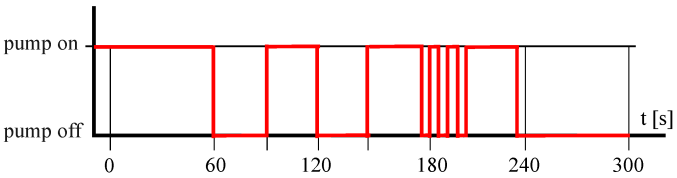

Fig. 3: Measurement procedure.

TABLE I: Localization results.

t_0, t_m [s]	fp. ℓ_1 abs.	fp. ℓ_1 norm.	fp. R abs.	fp. R norm.
1, 300	1,0,1	1,0,1	1,0,1	1,0,1
60, 90	0,0,1	0,0,1	1,0,1	1,0,1
60, 200	1,1,1	1,1,1	1,0,1	1,0,1
180, 205	0,0,0	0,0,0	1,0,0	1,0,0
235, 300	1,0,0	1,0,0	1,0,1	1,0,1

IV. Evaluation

In this section, we present and analyze our initial findings. Figure 4 and Figure 5 illustrate the processed sensor data across three distinct locations for each type of sensor. To mitigate quantization noise, we have implemented a moving average filter with a window size of 10, corresponding to a 1-second interval, across all data sets.

Figure 4 displays the raw data from the sensors, while Figure 5 shows the normalized sensor data, scaled from 0 to 1. The data from different sensors (NO2, C2H5OH, VOC, and CO) are indicated by varying colors. The dotted lines represent the reference measurements utilized for training, and the solid lines correspond to the observational measurements used for evaluation.

Upon visual examination, we observe that the sensor readings in the corridor (Figure 5a) exhibit more pronounced differentiation compared to those in the office (Figure 5b) or the laboratory (Figure 5c). Additionally, there is a noticeable offset between the training and evaluation datasets.

For the feature vector, we define:

$$\mathbf{r}_j = [\mathbf{s_1}\ \mathbf{s_2}\ \ldots\ \mathbf{s_4}]^T, \tag{2}$$

where each sensor vector s_s is composed of sequential measurements at times t_0 through t_m: $\mathbf{s_s} = [s_s(t_0)\ s_s(t_1)\ \ldots\ s_s(t_m)]^T$.

Table I presents the outcomes of our measurements across various time windows, which served as feature vectors in accordance to (2). Beyond employing the nearest neighbor algorithm (refer to (1)), we computed the correlation coefficient, denoted as R, to ascertain the most probable location by identifying the peak correlation between the training set and observational data. Our findings reveal that normalizing the measurement data is not required for our analysis. Additionally, employing the Nearest-Neighbor algorithm utilizing the ℓ_1-distance, alongside the correlation coefficient R, yields comparable results. For instance, the sequence $1, 0, 1$ in the table indicates that the first and third positions were accurately estimated, while the second position was incorrectly estimated. Notably, we successfully differentiated between all three positions using a time window

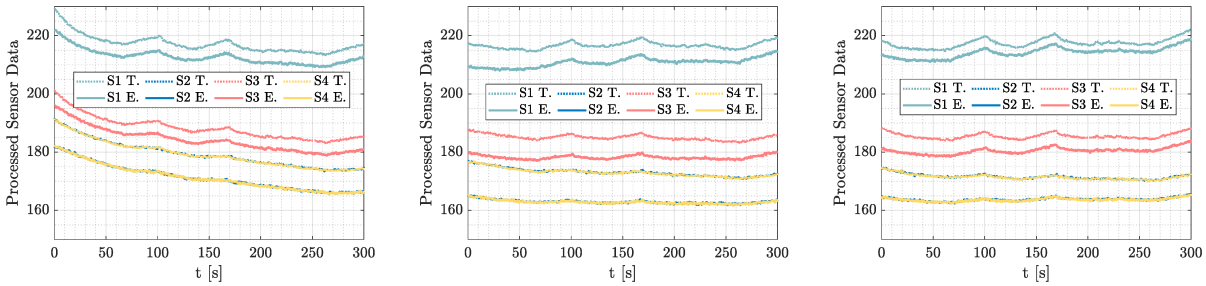

(a) Pos. 01. (b) Pos. 02. (c) Pos. 03.

Fig. 4: Absolute processed sensor data for the three positions. Each figure contains the training (T.) and evaluation (E.) data for each of the s sensors (S).

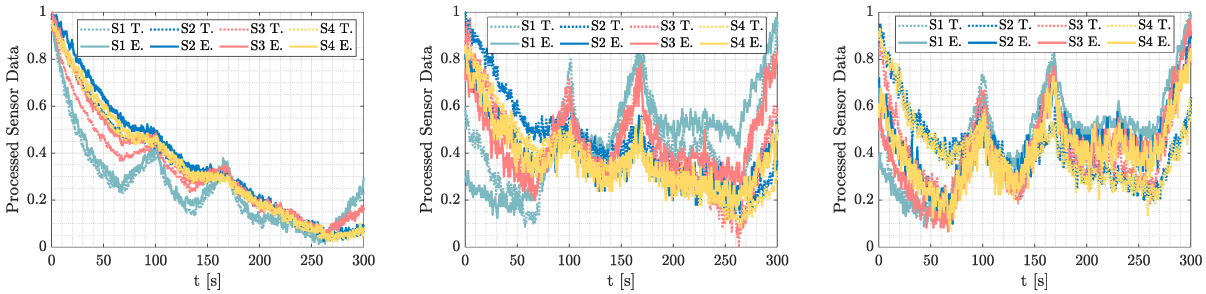

(a) Pos. 01. (b) Pos. 02. (c) Pos. 03.

Fig. 5: Normalized processed sensor data for the three positions. Each figure contains the training (T.) and evaluation (E.) data for each of the s sensors (S).

ranging from 60 s to 200 s, which encapsulated the most distinctive dynamics. Our initial findings indicate the potential to distinguish between locations such as corridors, office rooms, and laboratories, despite the observed drift in sensor readings. We propose that curve fitting could be applied to the sensor data when the pump is deactivated. Utilizing these fitted curves as fingerprints may enhance the accuracy of our localization efforts in subsequent studies.

Looking ahead, we plan to integrate additional sensors to identify foreign substances present in the air. The inclusion of such sensors could prove beneficial in environments with distinct characteristics, such as rooms with extensive leather furnishings or areas where soldering is frequently performed. Moreover, incorporating an oxygen (O2) sensor could aid in differentiating between frequently occupied spaces and those less used, such as offices with high foot traffic versus occasionally occupied laboratories. We also aim to extend our analysis to encompass sensor data collected over more extended periods and with different conditions such as opened windows.

V. Conclusion and Future Work

In this paper, we explored the capability of a COTS-available gas sensor, integrated into an electronic nose, to differentiate between various locations within an office environment. Our initial findings highlight the challenges associated with this task, still, we distinguish between the three positions correctly.

In the future, we intend to conduct a comprehensive analysis of the sensor data, taking into account environmental variables such as temperature and humidity, which may influence our measurements. Additionally, we plan to enhance the operational mode of the electronic nose and evaluate a range of algorithms suitable for indoor positioning applications.

Acknowledgments

This publication is a result of the research of the Center of Excellence CoSA in the project PRECISE funded by Interreg Deutschland-Danmark co-funded by the European Union.

References

[1] X. Liu, R. Jayaratne, P. Thai, T. Kuhn, I. Zing, B. Christensen, R. Lamont, M. Dunbabin, S. Zhu, J. Gao *et al.*, "Low-cost sensors as an alternative for long-term air quality monitoring," *Environmental research*, vol. 185, p. 109438, 2020.

[2] A. Anyfantis and S. Blionas, "Indoor air quality monitoring sensors for the design of a simple, low cost, mobile e-nose for real time victim localization," in *2019 Panhellenic Conference on Electronics & Telecommunications (PACET)*. IEEE, 2019, pp. 1–6.

[3] M. Di Rocco, M. Reggente, and A. Saffiotti, "Gas source localization in indoor environments using multiple inexpensive robots and stigmergy," in *2011 IEEE/RSJ International Conference on Intelligent Robots and Systems*. IEEE, 2011, pp. 5007–5014.

[4] P. Müller, S. Ali-Löytty, J. Lekkala, and R. Piché, "Indoor localisation using aroma fingerprints: A first sniff," in *2017 14th Workshop on Positioning, Navigation and Communications (WPNC)*. IEEE, 2017, pp. 1–5.

[5] M. Cimdins, S. O. Schmidt, and H. Hellbrück, "Mampi-uwb—multipath-assisted device-free localization with magnitude and phase information with uwb transceivers," *Sensors*, vol. 20, no. 24, 2020. [Online]. Available: https://www.mdpi.com/1424-8220/20/24/7090

[6] L. Liu, N. Na, J. Yu, W. Zhao, Z. Wang, Y. Zhu, and C. Hu, "Sniffing like a wine taster: Multiple overlapping sniffs (moss) strategy enhances electronic nose odor recognition capability," *Advanced Science*, vol. 11, no. 7, Dec. 2023.

3D-OLE: Three-Dimensional Optical Pipeline Inspection

Georg Fjodorow, Hossein Shoushtari, Harald Sternberg
Depts. Geodesy and Geoinformatics
HafenCity University Hamburg
Hamburg, Germany
firstname.lastname@hcu-hamburg.de

***Abstract*—Identifying structural damage in confined spaces with restricted access, such as gas pipelines, poses a significant challenge. This work proposes a concept, that can tackle the challenges by using a visual Simultaneous Localization and Mapping (vSLAM) system consisting of a various combined sensors on a 3D printed platform. The integration of multiple sensors results in an accurate trajectory and mapping solution. Damage detection can be then achieved by Machine Learning (ML) algorithms trained on extracted point clouds.**

***Index Terms*—vSLAM, Visual Odometry, Depth Camera, 3D Reconstruction**

I. Introduction

Controlling underground pipelines for damage involves expenses and requires high time expenditure. There is also a risk of blocking the pipe due to unknown geometry and hard-to-reach systems. Reconstructing a 3D model of the pipe system requires a platform or autonomous vehicle, that is small enough and can fit a setup of sensors.

The inspection of pipelines and the detection of damage within them includes a series of challenges: Due the subterranean position, GPS for localization is not available. Monotonously build pipes make it difficult for the SLAM algorithm to match images and construct a 3D model of the environment. Poor or non-existent light sources prevent the usage of traditional tracking devices.

A system with the combination of multiple sensors, such as camera, inertial measurement unit (IMU) and light detection and ranging (LiDAR) in addition to ML algorithms allow to resolve those issues. By synchronizing the data in form of images and various measurements, the surrounding environment can be mapped in 3D. The large amount of data, that is generated by the system, requires post-processing on a more powerful computer. It is also possible to save the collected data to a computer, enabling a map creation and damage detection at the end of the inspection time.

We propose a concept for a platform using a dual depth camera, a LiDAR, an IMU setup using a multi camera vSLAM and a ML algorithm and resulting in an accurate 3D representation and tracking solution, in pursuit of post-processing data analysis and visualization (see Fig. 1). The primary emphasis of this endeavor lies in sensor fusion, with a particular focus on integrating multiple sensing modalities into a cohesive system. The proposed system configuration would be tailored towards the development of a prototype capable of accommodating existing inspection tools.

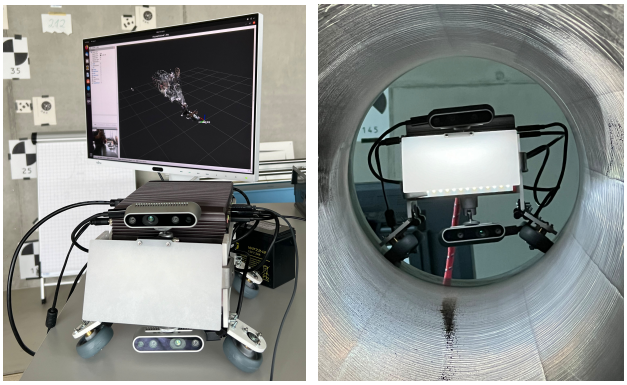

(a) Hardware and Software (b) Experimental Setup

Fig. 1. Current State of the 3D-OLE System Setup (22x15x10 cm)

The next section, Section II lists previous solutions and achievements. Section III describes the platform and the sensor setup. Section IV explains the proposed concept. Concluding with Section V, consisting of a summary and an outlook for upcoming improvements.

II. Related work

Precise and expeditious inspection methodologies are imperative for ensuring the secure functionality of expansive pipeline infrastructures. Predominantly employed for periodic surveillance of pipelines, autonomous inspection tools, including pipeline inspection gauges (PIGs) [1], [2] , and robotic crawlers [3], [4], play a pivotal role in this endeavor. The inspection can be done without the support of visual-based sensors. One way is to use a ”low-cost smart PIG” that integrates sensing and data collection capabilities within a disposable foam pig carrier [5], allowing inspections to be performed more frequently and at lower risk and cost. Mechanical arms equipped with strain gauge sensors are used for the detection of changes in the geometrical size and roughness of the pipes.

A recently published approach is using a dual-function depth camera array (DF-DCA) installed at the end of a PIG, for reconstruction and inspection of underground pipelines [6].

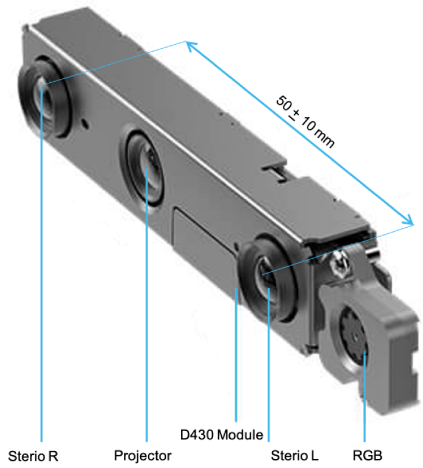

Fig. 2. RealSense D435i depth camera in details [13]

By using a central positioned camera and four oblique-viewed depth cameras it is possible to create a 3D model of complex pipelines with prior unknown geometrical segments.

In addition to advancements in pipeline inspection methodologies, the development of SLAM algorithms is experiencing rapid growth. One state of the art SLAM technique, that can be used for 3D reconstruction and inspection, is ORB-SLAM3 [7]. It supports monocular, stereo, RGB-D and fisheye cameras and offers a superior trajectory accuracy compared to other SLAM system, based on the EuRoC [8] and TUM-VI [9] dataset.

Another SLAM approach is RTAB-MAP [10]. The graph-based SLAM processes uses visual and LiDAR input and performs loop closure detection [11]. RTAB-MAP generates 2D grids and 3D point clouds and is part of the ROS SLAM library and the RealSense camera software, which makes it a convenient out-of-box experience.

Achieving a accurate tracking and mapping solution in real-time is possible by using 3D Gaussian Splatting SLAM [12] (3DGS). Unlike other SLAM systems, that use representations like occupancy or Signed Distance Function (SDF) voxel grids, meshes or point clouds, 3DGS focuses on optimizing memory usage, rendering speed and resolution.

III. System Setup

A. Hardware

The computer used in this setup is the Box PC LEC-7070-311A from Lanner Electronics. It has a Dual-Core i3-3217UE processor and 8GB DDR3 RAM. For a three-dimensional recording of the surroundings we use two RealSense D435i RGBD cameras with integrated IMUs, as seen in Fig. 2.

A RealSense L515 LiDAR or a RPlidar S2 360° Laser-scanner is planned to be positioned on top of the platform, in addition to the integrated IMU in the camera. It is also intended to add another IMU, from Witmotion, the HWT9053-485. However, both the LiDAR and the IMU are currently planned for implementation but have not yet been installed.

B. Software

The computer is operating on Ubuntu 18.04 and is using ROS, an advanced robotics development platform, used to realize complex robotics applications. The post-processing is done on a separate computer using a NVIDIA GeForce RTX 3080 GPU.

C. Testing Environment

To simulate a real environment a cylindrical pipe is used, which is fully coated in black (Fig. 3). The dimensions are approximately 3 meters in length and a diameter of 30cm. The addition of scratches and dirt is considered to mimic real pipeline systems and also to add features for the iterative loop closure algorithm, that is used to match recorded point clouds.

Fig. 3. Test environment located in the university laboratory

IV. Concept

A multi-functional robotic platform is designed for the pipeline inspection. A 3D printed case serves as base structure for the robotic system, where various components are mounted (Fig. 1). The RGBD camera is positioned on top of the platform and one at the bottom, increasing the the field of view and adding redundancy to the data collection. The cameras capture images and point cloud data as displayed in Fig. 4, enabling the system to recreate a 3D environment. The laser beams measure the distance to objects and the surface of the pipeline, generating another point cloud in addition to those from the dual camera setup.

All sensors are connected to a mini PC, that serves as controlling unit. The PC controls all sensors, while also processing the data and running algorithms for vSLAM. The system is powered by a battery which is placed at the back of the system. Since the pipeline lacks illumination, lighting is mounted at the front of the system.

The data collection process follows a simple procedure. The wheeled system moves along a linear path within the pipeline until reaching its end, after which it returns the same route in reverse, thereby generating redundant data.

Simultaneous localization and mapping is used to create a 3D representation of the pipeline in real-time using the both DRGB cameras. One of the used algorithms is RTABMAP [10] (Real-Time Appearance-Based Mapping). It uses a combination of appearance-based techniques and loop

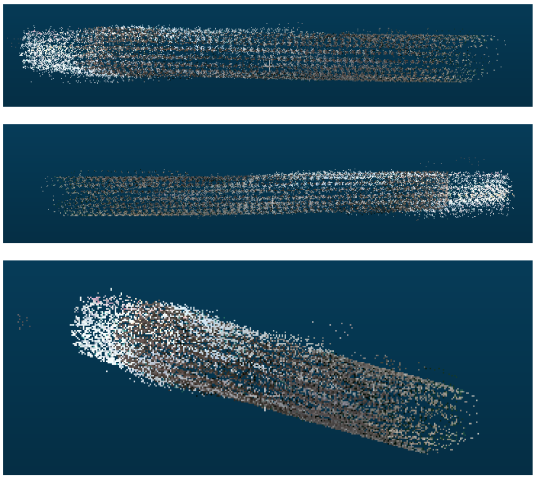

Fig. 4. Point cloud of the test environment

closure detection to build maps while estimating the trajectory. RTABMAP utilizes visual features extracted from sensor data, such as cameras. The second algorithm is a self-developed algorithm, tailored specific to the requirements of pipeline inspection. Integrating sensor fusion, feature extraction and probabilistic modeling while maintaining real-time performance. In contrast to other SLAM algorithms, we propose to fuse data from multiple LiDAR and camera systems to effectively address issues such as dynamic object detection and motion estimation. In addition to sensor fusion, our research incorporates deep learning techniques for localization within the SLAM framework to enhance the accuracy of position estimation.

Aiming for a comparison of both algorithms in experimental and real environments, an evaluation will be conducted. The comparison will include the consistency and precision of maps generated by both algorithms to see what accuracy can be reached. Efficiency will be assessed by the real-time performance, looking at processing speed and resource management. Using sensor noise, dynamic obstacles, varying lighting conditions, and changes in the environment layout to check the robustness of each algorithm.

V. Conclusion and Outlook

Instead of relying on one camera or one LiDAR, this setup facilitates sensor fusion through the use of multiple sensors, ensuring a minimum of blind spots and a wider coverage of the target area. Another benefit of the proposed setup is the higher density and quality of the point clouds, which can lead to better prediction by the ML model, but resulting in the requirement of higher processing power to effectively manage and analyze the vast amount of data generated by the sensors.

If the realization of the proposed setup and algorithm return a satisfying result, it is planned to implement a process that sends the data in real-time to the processing PC, which enables a real-time visualization of the pipeline and tracking of the system.

Another task is to compare the quality of the output with more cameras and more accurate LiDAR sensor, considering processing speed, required processing power and complexity of implementation in regards to the interaction between the sensors.

The final step is to develop and train a suiting deep learning model, aiming towards the elimination of the requirement of a powerful PC. Allowing the use of a all-in-one platform and maybe the use of cheap minicomputers like the Raspberry Pi or Jetson Nano.

Acknowledgement

Resources used in this study were funded by the 'IRENE UND FRIEDRICH VORWERK-STIFTUNG' as part of the 3D-OLE project.

References

[1] G. Canavese, L. Scaltrito, S. Ferrero, C.F. Pirri, M. Cocuzza, M. Pirola, S. Corbellini, G. Ghione, C. Ramella, F. Verga, A. Tasso, A. Di Lullo A novel smart caliper foam pig for low-cost pipeline inspection-part A: design and laboratory characterization. J. Pet. Sci. Eng., 127 (2015), pp. 311-317.

[2] C. Ramella, G. Canavese, S. Corbellini, M. Pirola, M. Cocuzza, L. Scaltrito, S. Ferrero, C.F. Pirri, G. Ghione, V. Rocca, A. Tasso, A. Di Lullo A novel smart caliper foam pig for low-cost pipeline inspection - Part B: field test and data processing. J. Pet. Sci. Eng., 133 (2015), pp. 771-775.

[3] J. Okamoto, J.C. Adamowski, M.S.G. Tsuzuki, F. Buiochi, C.S. Camerini Autonomous system for oil pipelines inspection. Mechatronics, 9 (7) (1999), pp. 731-743.

[4] G.H. Mills, A.E. Jackson, R.C. Richardson. Advances in the inspection of unpiggable pipelines. Robotics, 6 (4) (2017), p. 36.

[5] R. Chiara et. al. (2014). A novel Smart Caliper Foam pig for low-cost pipeline inspection – Part B: Field Test and data processing. Journal of Petroleum Science and Engineering. 133. 10.1016/j.petrol.2014.09.038i.

[6] Shang, Z. & Shen, Z. Dual-function depth camera array for inline 3D reconstruction of complex pipelines. *Automation In Construction*. 152 pp. 104893 (2023)

[7] C. Campos, R. Elvira, J. Rodríguez, M. Montiel, J. & D. Tardós, J. ORB-SLAM3: An Accurate Open-Source Library for Visual, Visual–Inertial, and Multimap SLAM. *IEEE Transactions On Robotics*. 37, 1874-1890 (2021)

[8] M. Burri, J. Nikolic, P. Gohl, T. Schneider, J. Rehder, S. Omari, M. Achtelik and R. Siegwart, The EuRoC micro aerial vehicle datasets, International Journal of Robotic Research, DOI: 10.1177/0278364915620033, 2016.

[9] S Klenk, J Chui, N Demmel and D Cremers), In International Conference on Intelligent Robots and Systems (IROS), 2021.

[10] Labbé, M. & Michaud, F. RTAB-Map as an open-source lidar and visual simultaneous localization and mapping library for large-scale and long-term online operation. *Journal Of Field Robotics*. 36, 416-446 (2018,10), http://dx.doi.org/10.1002/rob.21831

[11] Labbé, M. & Michaud, F. Appearance-Based Loop Closure Detection for Online Large-Scale and Long-Term Operation. *IEEE Transactions On Robotics*. **29**, 734-745 (2013)

[12] Matsuki, H., Murai, R., Kelly, P. & Davison, A. Gaussian Splatting SLAM. (2023)

[13] Intel Depth Camera D435i — intelrealsense.com. (https://www.intelrealsense.com/depth-camera-d435i/,2024), [Accessed 10-04-2024]

RSSI Indoor Localization System for Asset Management in Medical Facilities

Naglaa El Agroudy
Chair for Circuit Design and Network Theory
Technische Universität Dresden
naglaa.elagroudy@tu-dresden.de

Matthias Stege
Exelonix GmbH
Dresden, Germany
matthias.stege@exelonix.com

Uwe Sommerlatt
Exelonix GmbH
Dresden, Germany
uwe.sommerlatt@exelonix.com

Marco Gunia
Chair for Circuit Design and Network Theory
Technische Universität Dresden
marco.gunia@tu-dresden.de

Frank Ellinger
Chair for Circuit Design and Network Theory
Centre for Tactile Internet with Human-in-the-Loop(CeTI)
Technische Universität Dresden
frank.ellinger@tu-dresden.de

***Abstract*—This work presents an indoor localization system based on received signal strength indicator (RSSI) that is readily available in Bluetooth devices. Two algorithms are used for localization, namely proximity and weighted circular. Both algorithms are tested in an office room and a mean localization error of 1.76 m is measured. The proposed system shows its suitability for localization of medical assets in large medical facilities.**

Keywords— indoor localization, RSS, Bluetooth

I. Introduction

Indoor localization systems can be utilized in many applications in medical facilities, for example localization and tracking of medical assets. Automated asset management tools can improve the operation efficiency in medical facilities [1-2]. Such tools can be used in seeking medical devices and equipment shared between different medical units. It can also help in keeping track of expensive equipment and hence increased protection against theft. Localization tools can as well support the identification of medical equipment that require maintenance.

One of the aims of the secure medical microsystems and communications (SEMECO) project [3] is to design an indoor localization system that can determine the position of assets in medical facilities. Many positioning algorithms and technologies were researched in order to enhance indoor localization [2, 4]. In the proposed system, a device will be attached to the equipment to be located and then its position can be estimated with the help of fixed anchor nodes that will be distributed along the floorplan of the indoor environment under test. In this paper, received signal strength (RSS) based localization technique is investigated due to its simplicity and wide availability in many technologies such as WiFi and Bluetooth [2, 4], which means that it does not need a dedicated hardware. Although RSS based localization techniques have a lower accuracy compared to other techniques, they have shown an acceptable accuracy with an error below 5% [4], which makes them suitable indoors for the application of interest here, where it is enough to determine in which room an equipment is located. For the system presented in this paper, Bluetooth low energy (BLE) based devices are chosen since they can cover a range up to 100 meters [2]. BLE devices enable as well angle of arrival (AoA) in case a higher localization accuracy is needed in the future [4].

The remainder of this paper is organized as follows: In section II, the proposed system architecture is presented. Then in section III, background about RSSI localization and the algorithms employed are introduced. In section IV, measurement results that show the accuracy of the proposed system are presented. Finally, in section V, the results of this work are concluded.

II. Proposed System Overview

The proposed localization system is based on an active positioning system, where an active radio frequency (RF) transmission has to take place between the devices to be detected and the devices that serve as anchor nodes. This approach has advantages in terms of DC power (since RF power decreases versus distance by the power of 2 instead of power of 4) and privacy (devices can switch off the positioning function). The proposed system in this paper is composed of:

- Off-the-shelf Bluetooth beacon nodes that will be mounted on the walls of the different rooms of the indoor environment under test. The local positions of these nodes are stored in a database after installation and are known to the localization system.
- Sensor nodes which will be attached to the equipment to be localized. In the proposed system, 5G SENS device [5] is used. This device offers seamless tracking of assets indoor and outdoor. GNSS (Global Navigation Satellite System) reception is used for outdoor position tracking, whereby the estimated position is transmitted to the cloud environment via low power wireless access (LPWA) cellular standards Long Term Evolution for Machines (LTE-M) and Narrowband-Internet of things (NB-IoT). This offers runtime for few years with a single battery charge. Furthermore, a built-in Bluetooth receiver measures RSSI of Bluetooth beacons along with its unique media access control (MAC) address. This enables position estimation in indoor environments. Positioning can be triggered by an acceleration sensor. This enables low power consumption, since the device only needs to operate when it moves, and sleeps all other times to save power. The 5G SENS offers five sensors: temperature, humidity, air pressure, 6D acceleration and light. These sensors enable monitoring of assets conditions according to application needs. A device

management and a data processing IoT-cloud completes the solution. The device is built to tackle many different IoT use cases, from tracking mobile assets to monitoring conditions during delivery [5].

- The localization framework that was previously introduced in [6]. This framework gets the local positions of the beacon nodes as an input together with the RSSI data collected in the database from the sensor nodes. It then outputs the estimated local positions of the sensor nodes and writes them back into the database.
- A database that stores the RSSI data sensed by all sensor nodes from the beacon nodes versus time. The database also stores the estimated local positions of these devices versus time, which is generated by the localization framework.

An example employing the described system is shown in Fig. 1. In the coming section, a detailed explanation of the implemented technique is presented.

III. RSSI Localization Technique

RSSI measurements are performed and recorded between each sensor node and each beacon node which enables estimating the distance between them. The transmitted signal power P_t, the received signal power P_r and the distance d between the transmitter (beacons node) and receiver (sensor node) are related by [7]:

$$P_r = P_t \times \left(\frac{\lambda}{4\pi d}\right)^n \quad (1)$$

where λ is the RF carrier wavelength and n is the path loss exponent whose value is equal to 2 in free space and differs from one environment to another.

From equation (1), we can see that the received signal power is inversely proportional to the distance between the two nodes, and from this, the relationship between the RSSI and the distance can be defined as follows:

$$\text{RSSI} = P_r \text{ dBm} = P_0 \text{ dBm} - 10\, n \log(d/d_0) \quad (2)$$

where P_0 is the RSSI at distance d_0 usually defined at 1 m. The values for n and P_0 can be determined through performing several distance measurements while recording the corresponding RSSI values and then using curve fitting for calibration as was shown in [7]. Then the distance between the sensor node and the beacon node can be estimated based on the RSSI value by rearranging (2) to get:

$$d = 10^{-\frac{RSSI+P_0}{10\,n}} \quad (3)$$

If the beacon node is at a position (x_i,y_i,z_i) and the sensor node is at a position (x_n,y_n,z_n), then the distance between them is given as:

$$d_{i,n} = \sqrt{(x_i - x_n)^2 + (y_i - y_n)^2 + (z_i - z_n)^2} \quad (4)$$

where i and n are the IDs for the beacon node and sensor node respectively.

Thus combining equations (3) and (4) together, one can relate the (x_i,y_i,z_i) position of the beacon node to the (x_n,y_n,z_n) position of the sensor node through the corresponding RSSI measurement. All RSSI data that are gathered are stored in a database as shown in table 1.

TABLE 1: RSSI Data Saved at Database

Beacon Node Coordinates	Sensor ID 1	Sensor ID 2	⋯	Sensor ID n
(x_1,y_1,z_1)	RSSI(1,1)	RSSI (1,2)	⋯	RSSI (1,n)
(x_2,y_2,z_2)	RSSI (2,1)	RSSI (2,2)	⋯	RSSI (2,n)
⋯	⋯	⋯	⋯	⋯
(x_i,y_i,z_i)	RSSI (i,1)	RSSI (i,2)	⋯	RSSI (i,n)

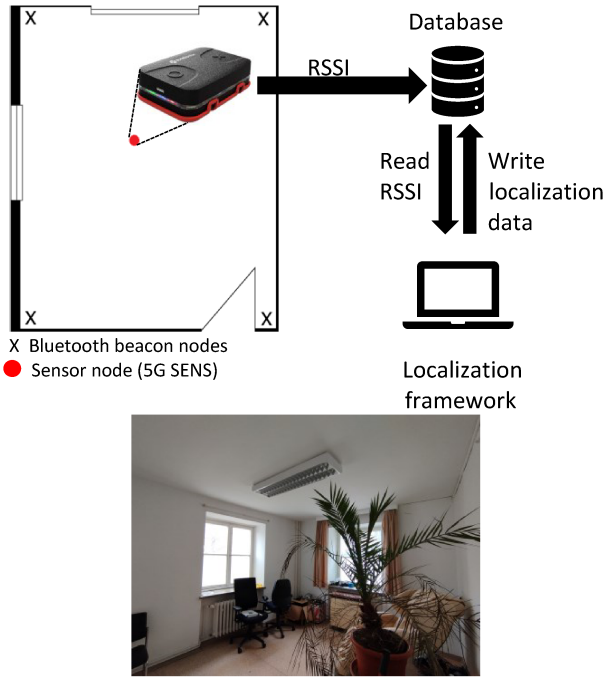

Fig. 1. Top: Overview of a localization scenario in an office room with four anchor nodes and one sensor node. Bottom: Photo of the office room.

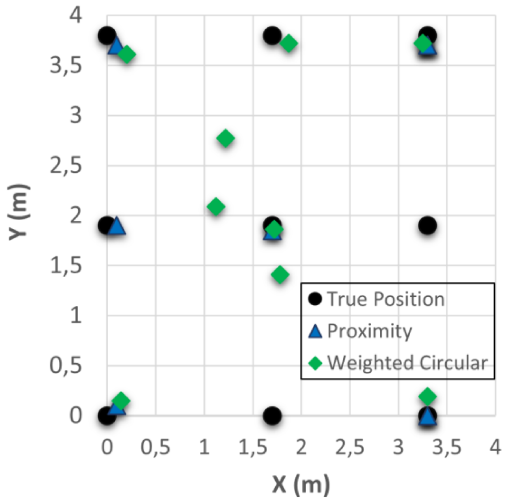

Fig. 2. Localization results using proximity and weighted circular algorithms

After calculating the distances based on equation (3) and storing the data in the database, localization can then take place using either calibrated algorithms and equations (3-4) or non-calibrated algorithms [4].

Calibrated algorithms take into account the parameters in equation (3) that can be different from one environment to another, which improves the localization accuracy.

TABLE 2: COMPARISON WITH OTHER INDOOR POSITIONING MEASUREMENTS

	Test Area (m^2)	Mean Error (m)	Technology
[8]	24.75	1	WiFi
[9]	27	5.82	Bluetooth
[10]	64	1.3	WiFi
[10]	64	1.7	Bluetooth
This	**12.54**	**1.76**	Bluetooth

An example of calibrated algorithms is the weighted circular algorithm [4] that minimizes the sum error of least squares of the estimated distance between the anchor node and the sensor node and also gives higher weight to the RSS measurements that are closer to the anchor nodes. On the other hand, non-calibrated algorithms ignore the environment parameters in equation (3) which simplifies the localization algorithm. An example is the proximity approach which estimates the position of the sensor node by using the position of the anchor node with the highest RSSI [4].

IV. MEASUREMENT RESULTS

Initial measurements for the proposed system were carried out in an office room sized 3.3 m by 3.8 m equipped with furniture. Four beacon nodes were installed at the four corners of the room as shown in Fig. 1. RSSI was then recorded between the sensor node (5G SENS) and each of the four beacon nodes at nine different locations distributed along the room as shown in Fig. 2. Two localization algorithms, proximity and weighted circular were then used to estimate the position of the sensor node. A mean localization error of 2.18 m and 1.76 m was obtained using proximity and weighted circular algorithms, respectively. The measurement results presented in Fig. 2 show that for proximity, the error is smallest at the corners of the room near the anchor nodes, while for the weighted circular the smallest error is obtained in the middle of the room as expected. It is worth mentioning that the localization framework runs in less than ten seconds including reading from and writing back to the database.

Table 2 shows comparison with other RSSI-based indoor positioning measurements that could be found in the literature. The mean positioning error of the presented system here is of an acceptable value compared to the others, keeping in mind that WiFi based positioning systems give better accuracy than Bluetooth based systems as was shown in [11]. An additional reference point was used in [8] in order to mitigate the errors that can be introduced due to multi-paths, which increases the hardware/costs needed for the system. In [10], all measurements ensured line-of-sight and also ten measurements were performed for each beacon node in order to average the error in the RSSI readings, which increases the run time for the positioning measurement. In this work, only one RSSI measurement per beacon node was performed.

CONCLUSION AND FUTURE WORK

An indoor localization system was presented for the application of asset management in medical facilities. The presented system shows its suitability for the intended application. Future work includes testing in a larger indoor environment with multiple rooms and multiple sensor nodes. Also, the impact of varying the number of anchor nodes per room on the positioning accuracy will be investigated. In addition, the effect of the number of RSSI measurements performed by each beacon node on the positioning accuracy is worth investigating.

ACKNOWLEDGMENT

This work was supported by the German Federal Ministry of Education and Research (BMBF) in the program “SEMECO” under contract number 03ZU1210CA. We would like also to acknowledge the cooperation with the Centre for Tactile Internet with Human-in-the-Loop (CeTi), a Cluster of Excellence at TU Dresden and with the BMBF funded project 6G-life (project ID: 16KISK001K).

REFERENCES

[1] “Cyber security and resilience for Smart Hospitals." [Online]. Available: https://www.enisa.europa.eu/publications/cyber-security-and-resilience-for-smart-hospitals/. [Accessed: 03- April- 2024].

[2] F. Zafari, A. Gkelias and K. K. Leung, "A Survey of Indoor Localization Systems and Technologies," in IEEE Communications Surveys & Tutorials, vol. 21, no. 3, pp. 2568-2599, 2019.

[3] "SEMECO." [Online]. Available: https://semeco.info/. [Accessed: 03- April- 2024].

[4] M. Gunia, Y. Lu, N. Joram and F. Ellinger, "Statistical Positioning Quality Metrics for Common Received Signal Strength-Based Positioning Techniques," in IEEE Sensors Journal, vol. 19, no. 23, pp. 11377-11395, 1 Dec.1, 2019.

[5] "5G SENS." [Online]. Available: https://www.exelonix.com/products/5g-sens-3/. [Accessed: 03- April- 2024].

[6] M. Gunia, Bo Zhang, N. Joram and F. Ellinger, "A hybrid localization framework supporting multiple standards and manifold post-processing," 2016 International Conference on Localization and GNSS (ICL-GNSS), Barcelona, Spain, 2016, pp. 1-6.

[7] N. El Agroudy, N. Joram and F. Ellinger, "Low power RSSI outdoor localization system," 2016 12th Conference on Ph.D. Research in Microelectronics and Electronics (PRIME), Lisbon, Portugal, 2016, pp. 1-4.

[8] M. E. Rusli, M. Ali, N. Jamil and M. M. Din, "An Improved Indoor Positioning Algorithm Based on RSSI-Trilateration Technique for Internet of Things (IOT)," 2016 International Conference on Computer and Communication Engineering (ICCCE), Kuala Lumpur, Malaysia, 2016, pp. 72-77.

[9] F. M. Wibowo and D. F. H. Permadi, "Comparison of Three Border Positioning (TBP) and Least Square Estimation (LSE) Algorithm Towards Indoor Positioning System (IPS)," 2023 IEEE International Conference on Communication, Networks and Satellite (COMNETSAT), Malang, Indonesia, 2023, pp. 629-634.

[10] F. A. Abed, Z. A. Hamza and M. F. Mosleh, "Indoor Positioning System Based on Wi-Fi and Bluetooth Low Energy," 2022 8th International Engineering Conference on Sustainable Technology and Development (IEC), Erbil, Iraq, 2022, pp. 136-141.

[11] M. Gunia, "Analyse und Design verschiedenartiger Positionierungssysteme, deren Zusammenführung sowie Vorhersage zukünftiger Positionen und Trajektorien," Ph.D. dissertation, Chair of Circuit Design and Network Theory, Technische Universität Dresden, Germany, 2023.

Printed Super-Capatteries for Smart Energy Storage Systems

Tilo Meister,*‡, Koichi Ishida*, Frank Ellinger*†
*Chair for Circuit Design and Network Theory, Technische Universität Dresden, Dresden, Germany, ‡e-mail: tilo@ieee.org,
†Centre for Tactile Internet with Human-in-the-Loop (CeTI), Technische Universität Dresden, Dresden, Germany

***Abstract*—Advances in roll-to-roll printing and in functional inks have made it possible to integrate printed super-capacitors and printed Li-ion batteries in one substrate, at a low cost, and high manufacturing throughput. Combined with smart power management circuitry, this new super-capattery device can offer the advantages of both underlying energy storage systems: high power-density and high energy-density. The power management circuitry has to maximize the super-capattery performance regarding charging speed, versatility, life time, and security. To cover a wide range of applications we propose different combinations of super-capacitor cells, Li-ion battery cells, and power management. As a result we can cover application profiles that fit active long-term low-power devices like active RFID-tags, NFC-tags, autonomous sensor nodes, other battery powered mobile devices like localization devices, but also high-power short-term profiles like remote controlled vehicles and robotics.**

***Index Terms*—energy storage, printed super capacitor, printed lithium-ion battery, super capattery**

I. Introduction

Electric energy storage system should securely store as much energy as possible at a low cost, small volume, long lifetime, and light weight. Simultaneously, they should usually be able to deliver a constant output voltage and high power, independent of their load conditions. On top of that, a convenient voltage level that is compatible with the used consumer is much preferred over the need to have voltage conversion in a device. However, the range of consumers is very wide and the voltage requirements can be very different. Further, quick recharge times are also important. In summary, the requirements posed to energy storage systems are manifold and their individual realizations are contradictory in nature.

Important parameters to describe the characteristics of an energy storage are its specific energy (energy-to-weight ration, EWR) or energy density, usually given in Wh/kg or Wh/l, respectively. Equally important are the parameters specific power (power-to-weight ratio, PWR) or power density, which describe how much power a storage can absorb and deliver, usually given in Wh/kg or Wh/l, respectively. The ratio of of specific energy to specific power is what is known as the characteristic time t_C of an energy storage.

$$t_C = {}^{\mathrm{EWR}}/_{\mathrm{PWR}} \tag{1}$$

It roughly determines how long it takes to fully charge an energy storage (lower is better) and how long it can deliver its maximum power before being depleted. In reality, depending on the power profile, either the charging or discharging process will be faster than the other. The three described parameters are shown in Fig. 1 in the so-call Ragone plot for the most relevant electric energy storages.

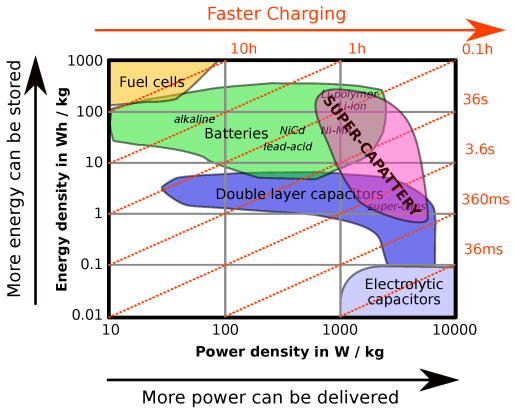

Fig. 1. Ragone plot classifying and comparing super-capatteries to the most relevant electric energy storage technologies. The diagonal lines mark the characteristic time of the technologies (based on data from [1]).

In this work, we focus on super-capatteries, a new combination of super-capacitors and Li-ion batteries that can cover an area in the Ragone plot, where no monolithic energy-storage type can currently operate. Only by combining the benefits of the two individual technologies super-capacitors and Li-ion batteries in a heterogeneous systems can this area be covered. Figure 2 and Tab. I show and compare the main characteristics of both super-capacitors and Li-ion batteries. Their cost-efficient and compact integration has recently become possible by the advances of roll-to-roll printing, active inks for Li-ion batteries, as well as active inks for super-capacitors [2]–[6]. Since it is a degree of freedom in what ratio to combine the two underlying technologies, there is a large spectrum of power density and energy density combination that can be covered, which is illustrated by the large size of the pink super-capattery area in Fig. 1. This freedom allows us to address a wide range of requirements and cover the needs of a wide variety of consumers.

Among the targeted consumers are active RFID- and NFC-tags as well as battery powered small mobile sensor nodes. These can benefit for example from a ultra-fast charging time combined with very long energy retention, because the high-power density of the super-capacitors is combined with the very high energy density and low leakage of rechargeable Li-ion batteries. Another scenario that can be covered is energy harvesting in mobile devices [7]. The presented solution can provide low leakage during the harvesting and storage phase, but can also, on-demand, provide high power, for example during short bursts of activity of a mobile wireless sensor node.

The durability of Lithium-ion (Li-ion) batteries is very

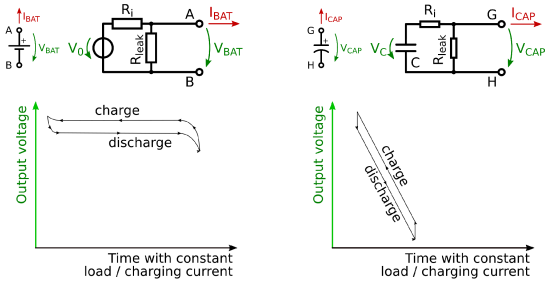

(a) (b)

Fig. 2. Comparison of the charging and discharing curve of (a) Li-ion batteries and (b) super-capacitors. At the top the respective basic equivalent circuit is shown.

TABLE I
COMPARISON LI-ION BATTERY AND SUPER-CAPACITOR CHARACTERISTICS.

Characteristic	**Li-ion Batteries**	**Super-Capacitors**
Voltage	typically 3.7 V, stable during discharge	$V_{break} \sim 4.0$ V, drops during discharge
Output impedance, R_i	higher	lower → can drive larger output current → can deliver larger output power
Specific power	lower (1.8 kW/kg)	higher (1-10 kW/kg)
Specific energy	higher (100 Wh/kg)	lower (1-10 Wh/kg)
Charging efficiency*	85 %	95 %
	*ratio of energy consumed by charging process and stored energy	
Leakage, $I_{leak} = V / R_{leak}$	lower loses 5 % of charge per month	higher loses 50 % of charge per month
Lifetime	2'000 cycles sensitive to deep discharge, overcharge, reverse polarity, and over temperature	100'000 cycles sensitive to over voltage, reverse polarity, and over temperature
Polarity	has polarity	has polarity

sensitive to under voltage, over voltage, as well as too high and too low temperatures. Exceeding permissible limits, for example by deep discharge, over charge, or a heavy continuous power drain, significantly reduces cell lifetime. Therefore it is necessary to have current limiters, temperature control, and voltage balancers directly integrated into the battery package, which we also investigate in this work.

II. APPLICATION PROFILES

As already indicated above, the requirements for an energy storage system depend heavily on the application and its profile. The core specifications of such an application profile are usually: 1) cost requirements 2) trade-off between energy density and power density 3) peak power and internal resistance 4) charging time 5) electric capacity 6) volume and/or weight.

Consider a wireless environmental sensor node with integrated localization. Such a battery powered device will be dormant most of the time. As a measurement of, for example, air quality commences, the node has to wake up and conduct several operations including: determine the air measurement and store the measurement datum. After a certain number of cycles the node also has to determine its position and establish a wireless link to a base station, via which it will transmit previously accumulated measurement data. The wireless transmission as well as the operation of the micro-controller require bursts of energy, while the rest of the time, almost no energy is consumed from the battery. Representative active currents for wireless front-ends operating at 3.3 V are 4.5 mA / 9.3 mA / 2.9 mA for Bluetooth Low Energy (BLE) / ZigBee / ANT, while the sleep currents are as low as 0.78 µA / 4.18 µA / 3.1 µA [8]. Depending on the duty cycle of the sensor node, the average currents can be well down in the tens of µA-range. A low-power micro-controller at 3 V consumes around 1 mA when active and drops to around 1 µA during sleep. The active currents of sensors can have a very wide range. For example, temperature and humidity sensing do not require much energy per measurement; localization usually consumes a relatively large amount of energy, because an active RF-front-end is required.

We also consider other applications profiles. On example are battery powered agile vehicles, which require the maximization of energy-density and power-density.

III. SUPER-CAPATTERY DESIGN & POWER MANAGEMENT

A. High power-density focused

Application examples that requires a high momentary power are for example photoflash lamps, flashing warning lights, robotics, and many other applications that involve mechanical actuators that are only rarely activated. Figure 3a shows the super-capattery design that will be optimized for this application profile. It contains a relatively large amount of super-caps and as little integrated electronics as possible. It is the cheapest and simplest proposed super-capattery, does however lack over- and under-volt protection.

B. High energy-density focused and safely stackable

Application examples that require a high energy density and high power density are different kinds of autonomous agile vehicles and robotics. The stackability provides the voltages required for motors. A light weight and high energy density enables a large range of the vehicles. Figure 4 shows a versatile stackable super-capattery that achieves a high energy density. An active or passive balancer is needed (at least during charging) to prevent reverse polarities across the super-capacitor and battery cells. Figure 4 shows two designs for different charging methods. In Fig. 4a all cells can be charged in series, which requires a balancer circuit that is integrated in the cells to prevent reversed polarities across cells. As shown in Fig. 4b the cells can alternatively be charged individually. The benefit of charging individually is that the balancer does not need to be integrated in the cell, but can be part of the external charger, which would benefit the energy density of the super-capattery.

C. Ultra-fast chargeability

To achieve ultra-fast charging a super-capattery with a large amount of super-capacitors as shown in Fig. 3b can be used.

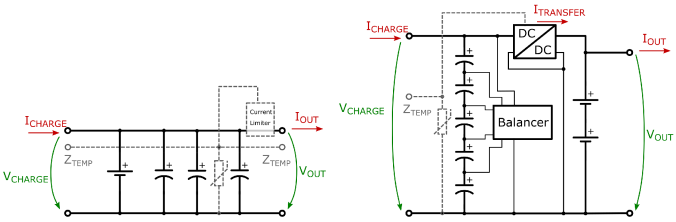

Fig. 3. Schematic of (a) high-power focused and (b) ultra-fast chargeable super-capattery.

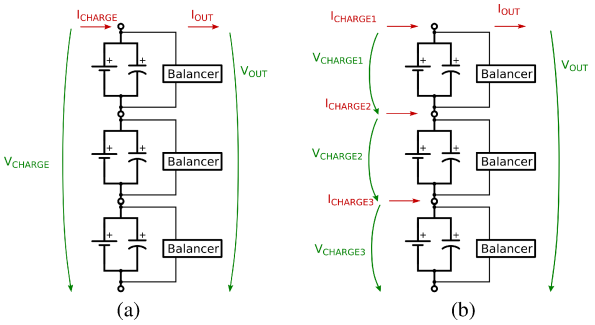

Fig. 4. Schematic of high-energy focused super-capattery. (a) Charging cells in series. (b) Charging cells individually.

The ultra-fast charging super-capattery operates in four modes. Ultra-fast charging is done by quickly charging the series of super-capacitor to a large voltage. The charging voltage can also be applied for a long period, which will give the batteries sufficient time to charge via the current $I_{TRANSFER}$. The charge is subsequently transferred to the batteries via a highly efficient, inductor less DC-DC-converter. As a result, in the long term, the energy is stored in the lower leakage battery cells. As soon as the voltage across the super-capacitors drops to the level of the battery, the DC-DC-converter is disabled. Power is now primarily supplied to a consumer from the energy stored in the battery cells. If the consumer temporarily requires high power the series of super-capacitors can directly buffer this demand. In this configuration, a passive or active balancer is necessary to ensure the lifetime of the super-capattery. Otherwise asymmetries of the super-capacitor capacities may lead to a reversing of the polarities across individual cells, which affects their lifetimes. Depending on the integration density, temperature sensor may also be necessary for the lifetime of the super-capattery, because of the high current flows during the very fast charging process. The required DC-DC-converters have an efficiency of around 90 % and a footprint of only 3 mm × 4 mm. This configuration effectively trades off super-capattery energy density and power density for a ultra-fast charging speed.

IV. Conclusion

Advanced printing technology and functional inks have enabled the direct integration of printed super-capacitors and printed Li-ion batteries on the same substrate. In this project SuperBat, first samples of super-caps have successfully been printed with a capacity of 100 mF at a dimension of 40 mm × 45 mm × 0.5 mm and a weight of only 1.44 g. They have the advantage of being much lighter and smaller compared to a current commercial super-cap that weighs in at 5.0 g and roughly has a diameter of 16 mm and a height of 11 mm. The printed super-cap has an ESR as low as around 5 Ω, i.e. this sample, when shorted delivers up to 200 mA after having been charged to 1 V. In this project also first Li-ion battery samples of similar dimensions and a capacity of around 100 mAh and 3 V have been printed. As a next step, both devices will be integrated on a flexible substrate in a high-volume low-cost roll-to-roll printing process, which will allow cheaper manufacturing compared to current super-caps and Li-ion batteries. Having both devices tightly integrated in one package together with smart power management, the new device becomes a super-capattery that can provide the advantages of both underlying energy storage systems. We showed how the super-capattery can be tailored to the needs of different application profiles including localization applications and can provide at the same time an higher power-density, higher energy-density, and lower cost compared to other electric energy storages.

Acknowledgment

This work was supported in part by AiF/IGF project SuperBat (331EBR/2). We would like to thank the Institute for Print and Media Technology at the University of Technology Chemnitz, Germany as well as the Institute of Metallurgical and Materials Engineering at Sakarya University, Turky for the discussions about printing technologies and functional ink technologies. We want to thank the BMBF (Federal Ministry of Education and Research of Germany) program 6G-life and the DFG cluster of excellence CeTI for discussions regarding the potentials of advanced DC supplies for information and communication technologies. We would like to thank Metirionic GmbH, Dresden, Germany for the collaboration on use cases and application profiles in this work.

References

[1] Q. Cai, et al., "A sizing-design methodology for hybrid fuel cell power systems and its application to an unmanned underwater vehicle," *Journal of Power Sources*, vol. 195, no. 19, pp. 6559–6569, 2010.

[2] Y.-Z. Zhang, et al., "Printed supercapacitors: materials, printing and applications," *Chem. Soc. Rev.*, vol. 48, pp. 3229–3264, 2019.

[3] D. L. Wood, et al., "Perspectives on the relationship between materials chemistry and roll-to-roll electrode manufacturing for high-energy lithium-ion batteries," *Energy Storage Materials*, vol. 29, pp. 254–265, 2020.

[4] Y.-Z. Zhang, et al., "Flexible supercapacitors based on paper substrates: a new paradigm for low-cost energy storage," *Chem. Soc. Rev.*, vol. 44, pp. 5181–5199, 2015.

[5] M. Tokur, et al., "Stress bearing mechanism of reduced graphene oxide in silicon based composite anodes for lithium ion batteries." *ACS applied materials & interfaces*, 2020.

[6] T. Weissbach, et al., "PANI-graphene nanocomposite as an active material for large-scale low-cost electrochemical double layer capacitors," IS&T conference Printing for Fabrication, Dresden, Germany, 2018.

[7] T. Meister, et al., "Bendable energy-harvesting module with organic photovoltaic, rechargeable battery, and a-IGZO TFT charging electronics," in *2015 European Conference on Circuit Theory and Design (ECCTD)*, Aug 2015, pp. 1–4.

[8] A. Dementyev, et al., "Power consumption analysis of bluetooth low energy, zigbee and ant sensor nodes in a cyclic sleep scenario," in *2013 IEEE International Wireless Symposium (IWS)*, April 2013, pp. 1–4.

Design Considerations for a System-Integrated MUX and DMUX for High-Speed Data Communication

Lars Garraud*, Marco Gunia* and Frank Ellinger*†
*Chair for Circuit Design and Network Theory (CCN) and
†Centre for Tactile Internet with Human-in-the-Loop (CeTI)
Technische Universität Dresden, 01062 Dresden
Email: lars_herve.garraud@tu-dresden.de

***Abstract*—An integrated Multiplexer (MUX) and Demultiplexer (DMUX) system designed for high-speed data communication in potential localization applications is presented. Our proposed system integrates a 2:1 MUX and 1:2 DMUX on a single chip, leveraging SiGe-BiCMOS technology to achieve data rates exceeding 200 Gb/s. This integrated approach aims to optimize signal transmission efficiency and system integration for future optical communication networks. The paper concludes with plans for fabrication, measurement, and integration into practical communication systems, marking a significant stride towards realizing high-speed communication solutions.**

Index Terms*— *Multiplexer, Demultiplexer, Optical Communication System, SiGe-BiCMOS

I. Introduction

High-speed communication systems enhance camera-based localization systems by enabling the real-time transmission of high-resolution images which is crucial for applications like virtual and augmented reality or industrial automation. In these systems, MUX play a critical role. With optical fiber as a high-speed data transmission medium with low attenuation, MUX combine as part of the transmission chain N-input low-speed channels (e.g. each camera in the localization system) to 1 channel with N-times the data rate, resulting in a high-speed output data stream. On the receiver, the DMUX takes one single input stream and splits it into N-paths, where the data rate of one output path is divided by N [1]. The DMUX outputs will be then further processed in the digital domain. The simplest architecture is a 2:1 MUX. Within this paper, we present a system integrated MUX and DMUX for high-speed communication. This is intended to ensure future measurability and thus enable the characterization of the individual subsystems in the communication chain. To the best knowledge of the authors, there exists currently no commercial data generator which can provide Non-Return to Zero (NRZ) data rates beyond 200Gb/s. The remaining part of the paper contains the categorization of related work, followed by the proposed system, and a conclusion with an outlook for further work.

II. Related Work

Recent advancement in semiconductor technologies such as in SiGe or InP results in increasingly reported higher data rates. This is due to the rising transit and maximum frequency f_t and f_{max}. Another method to raise the data rate is to use modulation techniques such as Phase-Amplitude Modulation (PAM)-4 [2] or Quadrature Amplitude Modulation (QAM)-16 [3]. To achieve high data rates, the analyzed related work focuses mainly on the selector circuit. A recently reported MUX in SiGe-BiCMOS with S-parameter measurements over 110 GHz bandwidth was published in [4] with a data rate of 190 GBaud/s [2]. On the contrast to the high bandwidth, this MUX requires already pre-synchronized data, meaning the two input data streams have to be aligned and additionally one data stream has to be shifted by half a clock period before being processed by the selector circuit. The highest data rate MUX was published in [5], realized in InP DHBT technology, but includes only a selector circuit. The authors are not aware of any other faster system.

Table I gives an overview over recently reported high-speed data circuits for MUX and DMUX. These high data rates stand in contrast to the power consumption, which plays a subordinate role.

There exists currently no fully integrated multiplexer targeting data rates exceeding 200 Gb/s for NRZ-signal modulation.

III. Approach

This proposed system contains a 2:1 MUX and a 1:2 DMUX and will be realized in one Integrated Circuit (IC). A system overview is given in Figure 1. The signal flow is from left to right. It has two data inputs, two data outputs and two clock (CLK) signals for each MUX and DMUX. All signals on-chip are fully differential. The MUX is composed of five latches (L) for re-timing purposes, a selector circuit, multiple I/O buffers, quadruper and active baluns for compact wideband signal transfer. At the input, the balun converts the single-ended signal into a differential one, before the signal is transmitted via transmission lines to corresponding latch inputs (L1 and L4). To compensate for losses in the signal path, a buffer stage is incorporated in between. The selector circuit chose

TABLE I
STATE-OF-THE-ART

Reference	Year	Technology	Circuit	Configuration	Bandwidth (GHz)	Symbol-Rate (GBd/s)	Modulation	Power (W)	Area (mm^2)
[5]	2019	InP	Selector	2:1	-	212[d]	NRZ	0.5-0.8	1.2 x 1.5
[3]	2019	InP	MUX[a]	2:1	110	138	QAM-16	0.99	2 x 2
[6]	2020	SiGe	MUX[b]	4:1	-	180[d]	NRZ	9.9	3 x 1.5
[4]	2021	SiGe	MUX[a]	2:1	110	190[c]	PAM-4[c]	1.22	0.97 x 1650
[7]	2021	SiGe	DMUX	1:4	36	128	NRZ	3.6	-

a. Analog MUX with no latches for re-timing. b. No output buffer. The selector drives directly laser diode.
c. Data rate and modulation of discussed chip given in [2]. d. Given in [5], [6] in Gb/s. For NZR modulation, BAUD-Rate is equivalent to Bit-Rate.

on the rising edge of clock signal the corresponding input data signals D1 or D2. The 50 Ohm buffer at the output of the selector is required to drive the 50 Ohm ground-signal-ground (GSG) pad for later measurement purposes. On the DMUX side after an input buffer, the signal is splitted and fed into two separate identical latches, each sampled with an high-frequency clock signal. It should be noted that one data path is fed with an inverted clock signal. The 50 Ohm output buffers in each path drive the 50 Ohm GSG pad. The clock is to be provided on-chip via bond-wires and routed differentially to the subsequent quadrupler via an active balun. The resulting high-frequency clock is then distributed via a high-impedance transmission lines. Each highlighted circuit block has its own supply and distribution network, taking different sampling phases of the clock into account. This allows the system to be measurable as a whole and also the individual sub-blocks. All individual blocks were designed for max speed. This approach has the goal of achieving high data rates. With the fully integrated approach, the system and especially the DMUX becomes measurable. To achieve such high data rates, all active components of each high-speed block were placed close together to minimize transmission losses. The system is designed in a way that the highlighted components in Figure 1 can be integrated into a communication system. The transition between electrical and optical signals is realized by means of a laser diode on the transmitter side and a photo diode on the receiver side.

This approach focuses on a full MUX structure including latches for re-timing purposes and to allows randomized data. Furthermore, the constraint of the designed system is that it needs to be measurable, resulting in the system choice of MUX and DMUX.

To achieve high-speed data rates with one on-chip integration, this proposed system will be fabricated in a SiGe-BiCMOS technology with a transit frequency f_t of 470 GHz [8]. As there is no technology on the market providing NRZ-signals with data rates beyond 200 Gb/s, the DMUX cannot be characterized as a stand-alone chip. With integration in future communication system, the proposed system can be extended into a fully integratable transmitter for optical communication. As the focus in on maximum speed, this design is not tailored on minimum power consumption.

As mentioned earlier, a critical design point is the bandwidth, resulting in a technology and circuit topology choice made by the designer to fulfill the given specification. Furthermore, a challenging aspect to name is the maximum frequency given by the material and length for which a bond-wire can transmit a high frequency signal. This fact is important for further measurements and characterization in the lab.

IV. CONCLUSION AND FURTHER WORK

This paper introduced a system-integrated MUX and DMUX designed for high-speed communication systems, enabling efficient data stream serialization and splitting for optimized signal transmission. Recent advancements in semiconductor technologies have facilitated higher data rates through

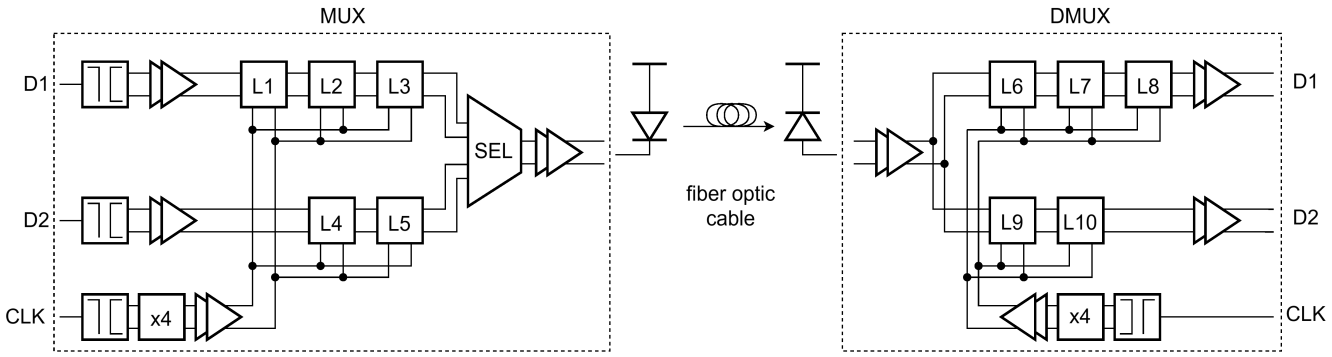

Fig. 1. System-integrated MUX and DMUX for potential optical communication system

improved transit frequency f_t parameters. The proposed system integrates a 2:1 MUX and 1:2 DMUX on one chip. Emphasizing maximum data rates while addressing critical design constraints, the proposed design will utilize a SiGe-BiCMOS technology, pushing the boundaries of high-speed communication system integration. Future work will concentrate on fabricating, measuring and integrating the proposed system into an optical communication system. This paper significantly advances high-speed communication systems by presenting an integrated MUX and DMUX solution tailored for data rates exceeding 200 Gb/s. Future challenges will come with characterization and measurement of the proposed design as supplying ultra wideband high frequency data signals on-chip is difficult.

ACKNOWLEDGMENT

This work was supported by the German Research Foundation (DFG) through the project PEAK under grant 464608440. We acknowledge the cooperation with the Centre for Tactile Internet with Human-in-the-Loop (CeTi), a Cluster of Excellence at TU Dresden and with the BMBF funded project 6G-life (project ID: 16KISK001K).

REFERENCES

[1] B. Razavi, *Design of integrated circuits for Optical Communications*, 2nd ed. Wiley, 2012.

[2] J. Schostak, T. Tannert, M. Grözing, V. Jungnickel, C. Schmidt, H. Rücker, M. Berroth, and R. Freund, "190 GBd PAM-4 signal generation using analog multiplexer IC with on-chip clock multiplier," in *2023 18th European Microwave Integrated Circuits Conference (EuMIC)*, 2023, pp. 1–4.

[3] M. Nagatani, Y. Miyamoto, H. Nosaka, H. Wakita, Y. Ogiso, H. Yamazaki, M. Mutoh, M. Ida, F. Hamaoka, M. Nakamura, and T. Kobayashi, "A 110-GHz-bandwidth 2:1 AMUX-driver using 250-nm InP DHBTs for beyond-1-tb/s/carrier optical transmission systems," in *2019 IEEE BiCMOS and Compound semiconductor Integrated Circuits and Technology Symposium (BCICTS)*. IEEE, nov 2019.

[4] T. Tannert, M. Grözing, M. Berroth, C. Schmidt, J. H. Choi, C. Caspar, J. Schostak, V. Jungnickel, R. Freund, and H. Rücker, "Analog 2:1 Multiplexer with over 110 GHz Bandwidth in SiGe BiCMOS Technology," in *2021 IEEE BiCMOS and Compound Semiconductor Integrated Circuits and Technology Symposium (BCICTS)*, 2021, pp. 1–4.

[5] A. Konczykowska, F. Jorge, M. Riet, V. Nodjiadjim, B. Duval, H. Mardoyan, J. Estaran, A. Adamiecki, G. Raybon, and J.-Y. Dupuy, "212-Gbit/s 2:1 multiplexing selector realised in InP DHBT," *Electronics Letters*, vol. 55, no. 5, pp. 242–244, mar 2019.

[6] C. Uhl, H. Hettrich, and M. Möller, "180 Gbit/s 4:1 power multiplexer for NRZ-OOK signals with high output voltage swing in SiGe BiCMOS technology," *Electronics Letters*, vol. 56, no. 2, pp. 69–71, Jan. 2020.

[7] P. Thomas, T. Tannert, M. Grözing, M. Berroth, Q. Hu, and F. Buchali, "1-to-4 analog demultiplexer with up to 128 GS/s for interleaving of bandwidth-limited digitizers in wireline and optical receivers," *IEEE Journal of Solid-State Circuits*, vol. 56, no. 9, pp. 2611–2623, 2021.

[8] H. Rücker and B. Heinemann, "High-performance SiGe HBTs for next generation BiCMOS technology," *Semiconductor Science and Technology*, vol. 33, no. 11, p. 114003, oct 2018. [Online]. Available: https://dx.doi.org/10.1088/1361-6641/aade64

An improved four-way ranging in phase-based ranging

Yan Wu
Metirionic GmbH
Dresden, Germany
yan.wu@metirionic.com

***Abstract*—By dramatically increased applications of Internet-of-Things (IoT) devices with cheap well-developed narrow-band technology such as Bluetooth Low Energy (BLE), localization of those devices in sensor networks is significant in civilian areas. An accurate ranging estimation between devices is required for achieving it. Phase-based ranging as an approach has been investigated in recent research. Two-way ranging as a common approach in the phase-based ranging has been applied in most of the related papers. However, due to the system imperfection of local oscillators in the low-cost IoT devices, the phase bias from the imperfection leads to inaccurate ranging estimation. In this paper, a proposed four-way ranging as an improved approach, is introduced, to alleviate the phase bias during measurement.**

***Index Terms*—phase-based ranging, two-way ranging, four-way ranging, IoT**

I. Introduction

Nowadays, IoT devices have been widely applied in ubiquitous applications in civilian areas. The need for deployment of those devices is driven by cheap narrow-band systems with well-developed technology, such as BLE.

To achieve the location of devices, an accurate ranging estimation between two devices is the main requirement. The concept of radio ranging has been studied and these are classified into three types [1], namely the power-domain approach, the time-domain approach and the phase-domain approach.

In the phase-domain approach, tones in a frequency band of interest are exchanged between two devices named as initiator and reflector, to form the spectrum in the frequency domain. Its channel impulse response can be extracted by applying inverse Fast Fourier Transformation (iFFT) or super-resolution spectrum algorithms [2].

Due to the less-efficient low-cost local oscillators in the devices, frequency bias exists with respect to the nominal frequency. It results in an offset in the extracted phase of the signal, which leads to an error in the ranging estimation.

II. Theory

In this section, the basic measurement scheme of the phase-based approach using two-way ranging [3] is first presented. Then, the system imperfection is introduced. From this point, an improved four-way ranging scheme is explained in the subsequent section.

A. Two-way ranging

The phase of a Radio-Frequency (RF) signal rotates during its propagation. The relationship between the phase and the distance between two devices is described as:

$$\phi(f,d) = \frac{-2\pi f_{\mathrm{RF}} d}{c} \mod 2\pi, \tag{1}$$

in which f_{RF} is the radio frequency, d is the distance, c indicates the speed of the RF signal.

On account of the short wavelength of the RF signal, a minimized distance range limits the measurement capability. Hence, to extend the unambiguous range, signal transmisson between two nodes in multiple frequencies is applied. In this way, the phase differences measured in consecutive frequencies are calculated. The distance during signal transmission derives from the idea of group delay, which represents the transit time through a channel.

The tone exchange at two frequencies between the initiator and the reflector in two-way ranging is depicted in 1. The initiator sends RF signal to the reflector at f_1. After down-conversion of the RF signal, the phase of the baseband complex value $\Phi_{\mathrm{I},1}$ is extracted by the reflector. Then the roles of both devices are swapped. The same procedure is repeated from the reflector to the initiator and the phase $\Phi_{\mathrm{R},1}$ is obtained. In this way, the tone exchange at f_1 is accomplished. Afterwards, the tone exchange at frequency f_2 proceeds.

By applying two-way ranging, the synthesized phase from both initiator and reflector are calculated as [4]:

$$\Phi_{2\mathrm{wr},1} = \Phi_{\mathrm{I},1} + \Phi_{\mathrm{R},1} = -4\pi f_1 \frac{d}{c} \tag{2}$$

$$\Phi_{2\mathrm{wr},2} = \Phi_{\mathrm{I},2} + \Phi_{\mathrm{R},2} = -4\pi f_2 \frac{d}{c} \tag{3}$$

The distance can be calculated as:

$$\Delta\Phi_{2\mathrm{wr}} = -4\pi\Delta f \frac{d}{c}, \tag{4}$$

in which

$$\Delta f = f_2 - f_1 \tag{5}$$

B. System imperfection

Both initiator and reflector contain a local oscillator as their signal generator, frequency synthesizer, and their own internal clock. In ideal conditions, both oscillators are synchronized at the reference frequency f_{ref} used to generate f_1 and f_2 in the

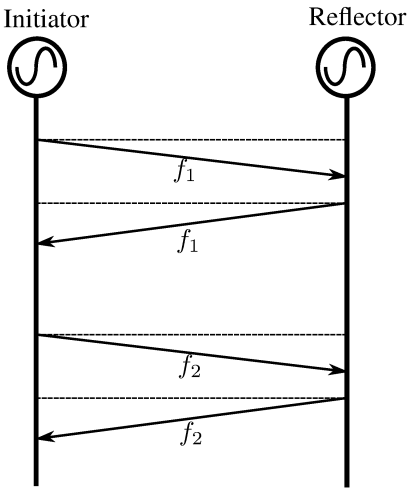

Fig. 1. Two-way ranging procedure

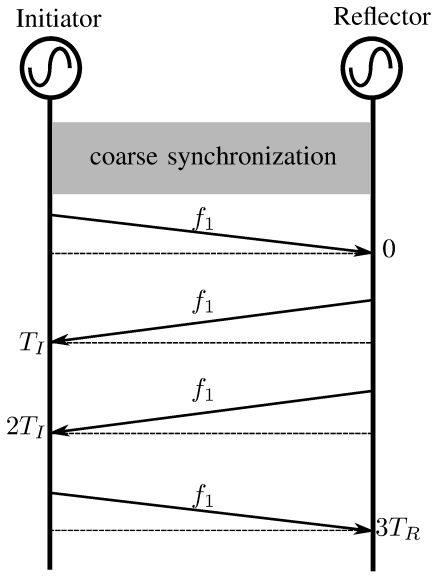

Fig. 2. Four-way ranging procedure

preceding section, and the phases of the generated signal from both devices are coherent. However, such synchronization cannot be accomplished in the low-cost IoT devices in practice. This imperfection results in phase offsets in the extracted phase during tone exchanges. Such offset has an impact on the ranging estimation.

The imperfection can be categorised into three components:

1) Initial Phase Offset: The local oscillators in both devices start with a random initial phase, which causes an initial phase difference before each tone exchange between the initiator and the reflector. It is compensated as an additional time delay in the ranging estimation.

2) Frequency Offset: The RF signal is generated by the oscillator and the Phase-Locked Loop (PLL) in the hardware of both devices. Since the low-cost oscillator in devices contains its individual frequency bias in respect of f_{ref}, the frequency offset between both devices exists. Hence, the phase offset varies during the tone exchange.

3) Time Offset: The local oscillator in the devices acts as both the RF signal source and the timestamp generator in the tone exchange. The RF frequency of both device varies at a pre-defined timestamp between two consecutive tone exchanges. Due to the frequency offset between devices, the RF frequency in both devices cannot vary simultaneously and it leads to an additional phase offset because of the asynchrony.

III. Proposed four-way ranging

The fundamental two-way ranging in the phase-based approach has been explained in the preceding section and many papers have looked into it [4] [5]. However, with the existence of system imperfection discussed above, their impact on the ranging estimation is not negligible.

To alleviate the degradation of distance accuracy, a proposed four-way ranging is provided:

1) A coarse synchronization between the initiator and the reflector at the beginning.
2) The initiator activates its transmitter and sends a tone at the defined frequency f_1.
3) The reflector activates its receiver during transmission period of the initiator, and extracts the phase at the timestamp defined as $t = 0$.
4) The roles of both devices are swapped at $t = T$ based on their own timestamp generators, and the initiator extracts the phase at $t = T_{\mathrm{I}}$.
5) Both devices keep their role, and the phase is extracted in the initiator at $t = 2T_{\mathrm{I}}$.
6) Finally, the roles are swapped back and the reflector extracts phase at $t = 3T_{\mathrm{R}}$. All timestamps at the receiver side are marked in 2.

The initial phase offset and the time offset components in the system imperfection can be alleviated by the well-known two-way ranging. However, the frequency offset cannot be mitigated by simply using this approach. The proposed four-way ranging can be regarded as the two-way ranging and its reciprocal, making it an solution to highlight such offset. By combining all the phases obtained in the four-way ranging, the accuracy in the ranging estimation can be improved.

References

[1] M. Pelka, C. Bollmeyer and H. Hellbrück, "Accurate radio distance estimation by phase measurements with multiple frequencies," 2014 International Conference on Indoor Positioning and Indoor Navigation (IPIN), Busan, Korea (South), 2014, pp. 142-151, doi: 10.1109/IPIN.2014.7275478.

[2] Y. Wu, N. Joram and R. T. Hach, "Quantitative Comparison of Distance Estimation Performance between TLS-MP and iFFT Methods in IEEE 802.15.4a Channel Models Using PSFM Radar Technique," 2021 International Conference on Indoor Positioning and Indoor Navigation (IPIN), Lloret de Mar, Spain, 2021, pp. 1-7, doi: 10.1109/IPIN51156.2021.9662549.

[3] Decawave. DW1000 User Manual: How to Use, Configure and Program the DW1000 UWB Transceiver. 2017. Available online: DW1000 User Manual (accessed on 26 April 2024).

[4] P. Zand, J. Romme, J. Govers, F. Pasveer and G. Dolmans, "A high-accuracy phase-based ranging solution with Bluetooth Low Energy (BLE)," 2019 IEEE Wireless Communications and Network-

ing Conference (WCNC), Marrakesh, Morocco, 2019, pp. 1-8, doi: 10.1109/WCNC.2019.8885791.

[5] I. Seto et al., "Sub-GHz Two-Way Ranging Based on Phase Detection for Remote Keyless Entry Systems," in IEEE Transactions on Vehicular Technology, vol. 71, no. 9, pp. 9705-9720, Sept. 2022, doi: 10.1109/TVT.2022.3181623.

On Current Trends in Positioning

Marco Gunia* and Frank Ellinger*†
*Chair for Circuit Design and Network Theory (CCN) and
†Centre for Tactile Internet with Human-in-the-Loop (CeTI)
Technische Universität Dresden, 01062 Dresden
Email: marco.gunia@tu-dresden.de

***Abstract*—This paper examines three trends in positioning, i.e. options for determining the location of a remote station in future communication standards, the transition from primary radar to secondary radar, and the integration of machine learning. While the first trend primarily concerns localization systems that are based on underlying communication infrastructure, the second trend relates more to proprietary approaches that are specifically designed for positioning. Apart from this, conventional concepts can be improved using artificial intelligence, e.g. to increase accuracy, to integrate results from multiple individual systems or to predict future trajectories.**

Keywords*—*Positioning, Localization, Trends, Future, Communication, Standard, Primary radar, Secondary radar, Artificial intelligence, Machine learning

I. Introduction

Even though many of the basic principles of positioning have been known for a long time, there is constant research and progress in the field. The paper examines three such trends and describes related literature. Arising from the desire for ever higher data rates, the first trend is the inclusion of positioning methods in future communication standards. The aim of the second trend, on the other hand, is to reduce energy consumption during localisation and to guarantee privacy. Due to the increased computing power of today's systems, ever more complex algorithms are feasible. In this context, machine learning finds its way into positioning, being the third trend.

II. Trends

Below, these trends are described in detail.

A. Future communication standards

Traditionally, a distinction is made between systems that are intended solely for communication and those that are created solely for positioning. When designing such positioning approaches, it is possible to freely define all parameters, including the transmission frequency, bandwidth and accuracy. However, the costs are very high, as in addition to the software, the corresponding circuits and associated circuit boards also have to be designed. For this reason, mixed topologies have emerged in which signal characteristics of systems originally intended as communication systems are read out and used for positioning. We described such systems in [1], [2] and [3]. In addition, individual research works also deal with the hybridisation of communication and positioning, e.g. [4].

For some time now, there is a visible trend towards including corresponding positioning methods in communication protocols. For example, the IEEE 802.15.4a standard has explicitly created the possibility of positioning by means of two optional signal formats, the Chirp Spread Spectrum and Ultra Wide Band (UWB). We described such a system in [5]. Besides, version 5.1 adds angular localization to Bluetooth.

The need for ever higher data rates for communication necessitates increasing frequencies and bandwidths, which means that the antennas used for signal transmission are becoming more and more directional. The rough position and direction of the receiver must therefore be known. Thus, simultaneous sensing and communication is used in modern standards, e.g. 5G includes measures for detecting the remote station [6].

B. Transition from primary to secondary radar

The second trend for radar systems concerns the transition from passive to active remote stations, i.e. from primary radar to secondary radar. On the one hand, this enables a reduction in energy requirements, as the transmission power is proportional to the fourth power in the first case and proportional to the square of the distance in the second case [7]. On the other hand, privacy is guaranteed with the latter, as the user can switch the corresponding functions on and off as required.

One possible approach is to install such radar systems at intersections to recognise Vulnerable Road Users (VRU). Corresponding information can then be forwarded to approaching vehicles. As almost every VRU nowadays carries a mobile device or a key batch, this device can act as a remote station. Such investigations are to be executed within the DistriMuSe project proposed for funding by the European Commission.

C. Artificial intelligence

Due to the increased computing power of today's systems and ongoing progress in research, the inclusion of artificial intelligence for positioning is visible in various places. Such concepts are useful where there is an underlying regularity that cannot be easily analysed, described or implemented. Machine learning methods work on either discrete or continuous data. Concept learning and decision tree learning are typical representatives of the first category. They enable to grasp simple concepts like Boolean conjunctions. In contrast, Bayesian approaches or neural networks belong to the second category that allow the representation of complex multidimensional functions. In either case, sufficient training data is required to capture the underlying regularities [8]. In the following, various such methods for localization are described.

The selection of a positioning system in the presence of multiple alternative systems represents a feasible approach for the aforementioned first two concepts. For example, it is

reasonable to set up two individual positioning systems in neighbouring rooms with a certain overlap in signal ranges. Depending on the signal qualities, it is now possible to learn a metric to choose the most suitable system per location, for example in terms of accuracy [9], [10]. In contrast to the isolated choice of just one system, learning to weight the individual results from all approaches is also an option.

Fingerprinting is the process of determining the position depending on local signal characteristics in an online phase by comparison with a database. The conventional approach to initialising that dataset consists of a preliminary measurement of the signals at every possible position in an offline step. Due to that time-consuming activity, the database usually contains a very limited number of entries. Often, signal strength is chosen as a measure. Since even small changes in the environment, e.g. moving a chair indoors, have an influence on the signal characteristics, the measured values will typically not exactly match the database. Thus, methods for selecting the best fit are necessary. Classical methods like the K-nearest neighbours [11] suffer from poor performance, if the record is growing. Moreover, biased estimates are created, if there are imbalances in the selected locations [12]. New types of research use neural networks, both to generate additional virtual points in the dataset from the recordings in the offline phase and to seek for the best estimated position in the online phase [13]. Further works also assist the learning process by considering ray tracing [14] or focuses on learning to recognise the number of people and their gestures based on the signal properties [15].

In addition to estimating the current location, efforts are made on predicting all future positions, i.e. the trajectory. Typical representatives are Recurrent Neural Networks (RNN). Non-recurrent neural networks represent an acyclic directed graph which, similar to combinatorial circuits in digital technology, assigns an output value to the inputs at each point in time independently of past values [10]. Thus, predictions depending on successive values of a time sequence cannot be made by this structure [8]. However, such applications are realised using RNNs, in which cycles are built into the network, e.g. by feeding back outputs to the inputs. In terms of digital technology, RNNs correspond to sequential models [10]. The problem is that the influence of previous input values decreases with increasing time [16]. Long Short Term Memory (LSTM) networks ([17]) are special RNN, where shortcuts are introduced to maintain the impact of important long past values. A vanilla LSTM network for estimating the future path of pedestrians is proposed in [18]. Social interactions are also analysed there. To further improve prediction, additional data can be included, e.g. scene layouts as in [19].

III. Conclusion and Further Work

The paper analysed three current trends in the field of positioning. Firstly, options for determining the location of the remote station in future communication standards were discussed. For communication links, this enables a significant improvement on accuracy compared to conventional methods based on evaluating the RSS. On the other hand, steadily increasing frequencies require more directional antennas, which means that a rough knowledge of the location of the remote station is beneficial. The second trend is the transition from primary radar, i.e. systems in which the remote station does not actively participate in determining the position, to secondary radar systems, where the co-operation of the remote station is necessary. Finally, the paper looked at ways of incorporating artificial intelligence to enhance position estimation accuracy.

Acknowledgment

We acknowledge the cooperation with the Centre for Tactile Internet with Human-in-the-Loop (CeTi), a Cluster of Excellence at TU Dresden and with the BMBF funded project 6G-life (project ID: 16KISK001K).

References

[1] M. Gunia, A. Zinke, N. Joram, and F. Ellinger, "Setting up a phase-based positioning system using off-the-shelf components," in *Proc. 14th Work. Positioning, Navig. Commun. (WPNC'17)*, Bremen, Germany: IEEE, 2017, pp. 1–6.

[2] M. Gunia, N. Joram, and F. Ellinger, "Theoretical considerations regarding the application of received signal strength within heterogeneous indoor positioning systems," in *Expert Talk on Localization (EToL'18)*, Lübeck, Germany, 2018, pp. 1–4.

[3] M. Gunia, A. Zinke, N. Joram, and F. Ellinger, "Hardware design for an angle of arrival positioning system," in *4th KuVS/GI Expert Talk on Localization (EToL'19)*, Lübeck, Germany, 2019, pp. 1–3.

[4] E. Sobotta, "Rekonfigurierbare Transceiver für mehrere Standards und Frequenzbänder," Diss. Technische Universität Dresden, 2019, pp. 1–265.

[5] M. Gunia, F. Protze, N. Joram, and F. Ellinger, "Hardware design for an ultra-wideband positioning system using off-the-shelf components," in *2nd KuVS Expert Talk on Localization*, Jul. 2016, pp. 11–12.

[6] M. A. Hassanien, M. Jenning, and D. Plettemeier, "Beam steering system using rotman lens for 5g applications at 28 ghz," in *2017 IEEE Int. Symp. Antennas Propag. & USNC/URSI Nat. Radio Sci. Meeting*, 2017, pp. 2091–2092.

[7] A. Figueroa, "Advanced system architectures and processing algorithms for digital beamforming radars," Diss. Technische Universität Dresden, 2021, pp. 1–188.

[8] T. M. Mitchell, *Machine Learning*. McGraw-Hill, 1997.

[9] M. Gunia, Y. Lu, N. Joram, and F. Ellinger, "Statistical positioning quality metrics for common received signal strength-based positioning techniques," *IEEE Sensors J.*, vol. 19, no. 23, pp. 11 377–11 395, 2019.

[10] M. Gunia, "Analyse und Design verschiedenartiger Positionierungssysteme, deren Zusammenführung sowie Vorhersage zukünftiger Positionen und Trajektorien," Diss. Technische Universität Dresden, 2023, pp. 1–371.

[11] P. Bahl and V. Padmanabhan, "Radar: An in-building rf-based user location and tracking system," in *Proc. IEEE INFOCOM 2000. Conf. Comput. Commun. Nineteenth Annu. J. Conf. IEEE Comput. Commun. Soc. (Cat. No.00CH37064)*, vol. 2, 2000, 775–784 vol.2.

[12] P. Roy and C. Chowdhury, "A survey of machine learning techniques for indoor localization and navigation systems," *J. Intell. & Robot. Syst.*, vol. 101, no. 3, pp. 63–96, Mar. 2021.

[13] Y. Narita, S. Lu, and H. Kamabe, "Accuracy evaluation of indoor positioning by received signal strength using deep learning," in *24th Int. Conf. on Advanced Commun. Techn. (ICACT)*, 2022, pp. 132–136.

[14] X. Gan, B. Yu, L. Huang, and Y. Li, "Deep learning for weights training and indoor positioning using multi-sensor fingerprint," in *Int. Conf. Indoor Positioning Indoor Navig. (IPIN)*, 2017, pp. 1–7.

[15] F. Adib and D. Katabi, "See through walls with wifi!" *SIGCOMM Comput. Commun. Rev.*, vol. 43, no. 4, pp. 75–86, Aug. 2013, ISSN: 0146-4833.

[16] L. Yann, B. Yoshua, and H. Geoffrey, "Deep learning," *Nature*, vol. 521, no. 7533, pp. 436–444, 2010.

[17] S. Hochreiter and J. Schmidhuber, "Long short-term memory," *Neural Comput.*, vol. 9, no. 8, pp. 1735–1780, Nov. 1997, ISSN: 0899-7667. [Online]. Available: https://doi.org/10.1162/neco.1997.9.8.1735.

[18] A. Alahi, K. Goel, V. Ramanathan, A. Robicquet, L. Fei-Fei, and S. Savarese, "Social lstm: Human trajectory prediction in crowded spaces," in *2016 IEEE Conf. Comput. Vision Pattern Recognition (CVPR)*, 2016, pp. 961–971.

[19] H. Xue, D. Q. Huynh, and M. Reynolds, "Ss-lstm: A hierarchical lstm model for pedestrian trajectory prediction," in *2018 IEEE Winter Conf. Appl. Computer Vision (WACV)*, 2018, pp. 1186–1194.

Passive Localization for Underwater Swarm Vehicles using a Low-cost Acoustic Modem

Yuehan Jiang
Hamburg University of Technology
Institute for Autonomous Cyber-Physical Systems
Hamburg, Germany
yuehan.jiang@tuhh.de

Bernd-Christian Renner
Hamburg University of Technology
Institute for Autonomous Cyber-Physical Systems
Hamburg, Germany
christian.renner@tuhh.de

***Abstract*—A passive localization method is presented for underwater swarm vehicles using the low-cost ahoi modem. To achieve the self-localization of all passive vehicles in a swarm, it requires one actively transmitting vehicle performing two-way ranging (TWR) with reference buoys, while other vehicles just overhear the transmitted acoustic packets passively. In every polling cycle of the active vehicle, the latest range measure and position of the active vehicle are encoded and sent out in the polling packet. The time difference of arrival (TDOA) between the polling packet and the ranging acknowledgment packet from the receiving buoy is measured by the passive listening vehicle and fed to a least squares solver to estimate the passive vehicle's position. The proposed localization method is tested in a shallow water channel in Hamburg with a BlueROV2 and several surface buoys. The paper demonstrates that the localization result of a passive listening buoy achieves sub-meter level accuracy.**

***Index Terms*—underwater swarm localization, low-cost, passive acoustic localization, ahoi modem, TWR, TDOA, DESERT simulator, BlueROV2**

I. Introduction

The ability of self-localization is fundamental for autonomous underwater vehicles (AUV) swarms. While single vehicles acoustic localization is well studied, the cooperative localization for underwater swarm vehicles is still at the early stage [1]. Acoustic self-localization methods can be categorized as active methods and passive ones. For active methods, two-way travel-time (TWTT) is often used [2], [4] where every vehicle performs active two-way ranging (TWR) with multiple anchors, which is hardly scalable since communication overhead is non-negligible for large swarm size. On the other hand, the passive methods are more scalable for larger swarms since the vehicles can self-localize by passively listening. Usually one-way travel-time (OWTT) is used where the vehicles listen to packets sent periodcally from anchors [3]. However, passive OWTT methods depend on accurate measure of time-of-arrival (TOA), which may require expensive atomic clocks. Other passive methods use time difference of arrival (TDOA) which does not require the time synchronization between the sender and receivers [5], [6]. However, they are either only tested in small water tanks or require real-time clocks (RTC) for anchor nodes which are prone to clock drift.

To utilize the scalable benefit of passive localization and alleviate the synchronization restrict, we propose a passive self-localization method for swarm vehicles which caters for the needs of low-cost, no synchronization requirement, and provide field experiment in a harbor area with real underwater robot. The proposed acoustic self-localization method uses portable, low-cost devices and is scalable for swarms of passive vehicles with minimized communication overhead.

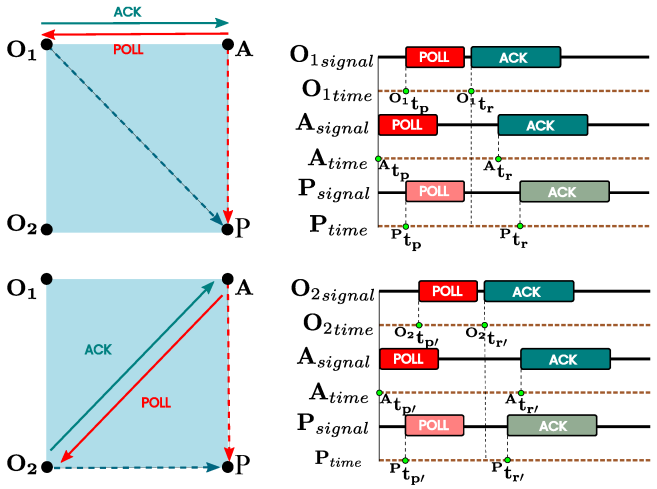

Fig. 1. The passive localization protocol. Left side is a 2D geometry illustration of the AUVs and buoys. Right side is the acoustic packet exchanged timelines.

Contributions of this work include:

- an acoustic passive localization method for underwater swarms that is scalable and without time synchronization.
- design and implementation of the passive localization protocol with DESERT Underwater [7] and a simulation scenario with two buoys and two AUVs.
- test of the passive localization method in a field experiment using a BlueROV2 [8] and three floating buoys. The localization result shows that the root-mean square error (RMSE) of the passive listening buoy is below 1 m.

II. Passive Localization Protocol

We illustrate the passive localization protocol with two fixed buoys $\mathbf{O}_1$, $\mathbf{O}_2$ and a minimal swarm of an active AUV (AAUV) $\mathbf{A}$ and a passive AUV (PAUV) $\mathbf{P}$ deployed in a rectangular shape. A full cycle of the passive localization protocol is shown in Fig. 1, where $\mathbf{A}$ periodically sends an

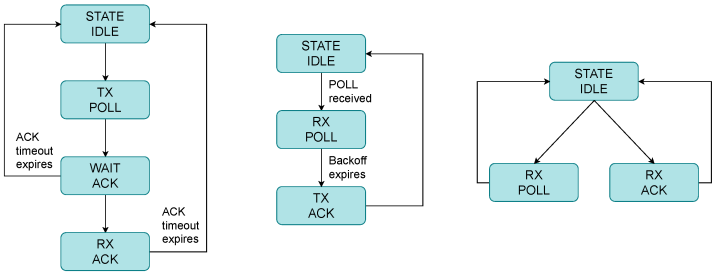

(a) UWTWR_AAUV (b) UWTWR_NODE (c) UWTWR_PAUV

Fig. 2. From left to right: state machine of the UWTWR protocol for an active AUV (AAUV) (a), for a fixed buoy (b), for a passive AUV (c), respectively.

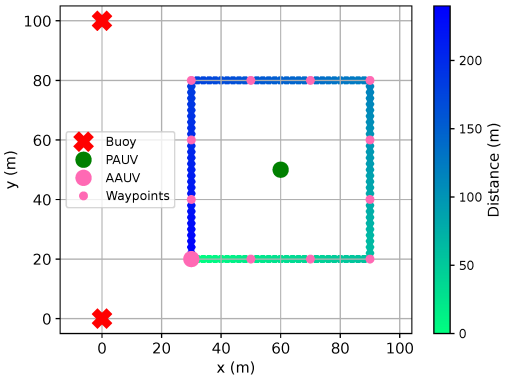

Fig. 3. A simulation scenario where the AAUV is moving around PAUV in a $60\,\mathrm{m} \times 60\,\mathrm{m}$ square-shaped area. Color bar represents the traveled distance by the AAUV.

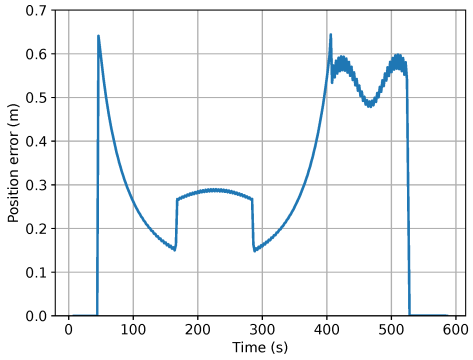

Fig. 4. PAUV 2D position error in simulation.

acoustic polling (POLL) packet to two buoys alternately. First POLL is sent to buoy $\mathbf{O_1}$. After a short back-off time the buoy responds with an acknowledgment (ACK) packet to $\mathbf{A}$. Then $\mathbf{A}$ repeats the same process with buoy $\mathbf{O_2}$. $\mathbf{P}$ "overhears" the POLL and ACK during the whole transmission. Upon reception of the ACK packets, $\mathbf{A}$ gets the distance measure to the target buoy from the time-of-flight (TOF) encoded in the ACK packet and the speed of sound in water.

The following equations of the geometric constraints can be derived:

$$\begin{aligned} \overline{\mathbf{O_1P}} - \overline{\mathbf{AP}} &= ({}^{\mathbf{P}}\mathbf{t_r} - {}^{\mathbf{P}}\mathbf{t_p}) \cdot \mathbf{c} - \mathbf{T_{poll}} \cdot \mathbf{c} - \overline{\mathbf{AO_1}} \\ \overline{\mathbf{O_2P}} - \overline{\mathbf{AP}} &= ({}^{\mathbf{P}}\mathbf{t_{r'}} - {}^{\mathbf{P}}\mathbf{t_{p'}}) \cdot \mathbf{c} - \mathbf{T_{poll}} \cdot \mathbf{c} - \overline{\mathbf{AO_2}} \end{aligned} \tag{1}$$

where distances are represented by overlined variables, $\mathbf{T_{poll}}$ is the duration of POLL packet, $c = 1500\,\mathrm{m/s}$ is sound speed in water. The above equations are used for the self-localization of the passive overhearing AUV $\mathbf{P}$. Due to scalability of the protocol, it applies to swarms with more PAUVs.

III. Simulation with DESERT Underwater

A. Passive TWR Protocol

We implement the passive TWR protocol as a MAC layer protocol called UWTWR using the DESERT simulator [7]. The general behavior of the protocol is depicted as the state machines in Fig. 2 whereas the AAUV transmits POLL packet to two buoys (as "NODE") periodically. The AAUV transmits every $2\,\mathrm{s}$ a POLL packet of $14\,\mathrm{bytes}$, first to the first buoy, then to the second buoy. Every sent POLL will be responded by the target buoy with a $10\,\mathrm{bytes}$ ACK packet. In this work we assume that AAUV position is available and focus on localizing the passive vehicle thus the real position of AAUV and the latest range measure to the last polled buoy is enclosed in the POLL packet. PAUV also receives the POLL and ACK packets of every polling cycle and upon reception of ACK, PAUV is able to measure the TDOA of POLL and ACK reception.

B. Simulation and Result

In simulation, two static buoys are set at fixed positions known to all agents. The PAUV is static and the AAUV is moving at $0.5\,\mathrm{m/s}$ along a square-shaped trajectory around the PAUV, as depicted in Fig. 3. In the simulation, buoys and AAUV are all at depth of $100\,\mathrm{m}$ and PAUV at depth of $50\,\mathrm{m}$. The data rate is $200\,\mathrm{bit/s}$.

With the UWTWR protocol, the PAUV records log files where the latest AAUV position, the distance measure from AAUV to the buoys and the TDOA measure can be extracted. The extracted data are fed into a least squares optimizer GTSAM [9] which allows the PAUV to estimate its position every $2\,\mathrm{s}$, upon the reception of a POLL packet. The localization error, e.g. the euclidean distance from the estimated PAUV 2D position to its true position is shown in Fig. 4.

IV. Real Experiment

A field experiment was carried out on December 20th, 2023 in a shallow water canal in Hamburg, Germany. Three floating buoys were deployed, two of which served as anchors with known GNSS positions, and one as a static listening PAUV. A BlueROV2 is deployed as the AAUV that moves along a rectangle-like shape beneath the water surface. All buoys and the ROV have RTK-GNSS antennas mounted on top of a mask which stays above the water during the whole experiment and provide the ground truth positions of centi-meter accuracy at $1\,\mathrm{Hz}$ for later evaluation. A low-cost acoustic modem, ahoi modem [10] is mounted on all buoys about $1.5\,\mathrm{m}$ below the water surface. The one on the BlueROV2 is about $10\,\mathrm{cm}$

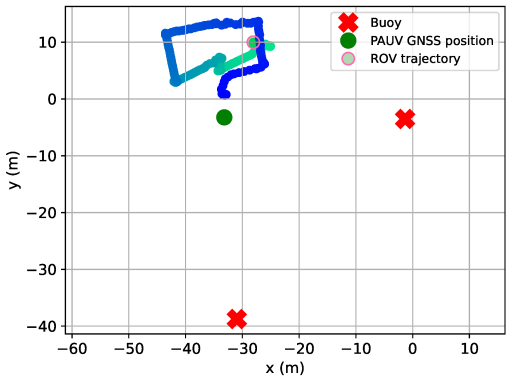

Fig. 5. The real experiment scenario with two fixed floating buoys (red cross), a passive listening buoy (green dot) and a BlueROV2 that moves at around $0.5\,\mathrm{m/s}$ along a rectangle-like trajectory.

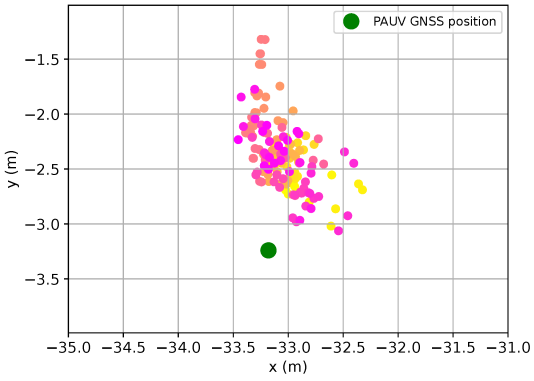

Fig. 6. Passive buoy 2D position estimates (represented by colored dot distribution).

underwater. The GNSS positions of all buoys and the trajectory of BlueROV2 is shown in Fig. 5

A. Modem Communication Protocol

The experiment adopts the same communication protocol as in the simulation which is implemented using the python library and the firmware of the ahoi modem. The modem on BlueROV2 sends a $14\,\mathrm{bytes}$ POLL packet every $2\,\mathrm{s}$ to the buoys alternately. The buoy which receives the designated POLL responds with a $10\,\mathrm{bytes}$ ranging ACK packet after a short processing time of around $12.26\,\mathrm{ms}$. The passive listening buoy that receives all POLL and ACK packets measures the TDOA of the adjacent POLL and ACK packets from the BlueROV2 and the polled buoy.

B. Experimental Result

As shown in Fig. 6, the colored dots distribution represents the position updates of the passive buoy. The duration of the experiment scenario is $7.6\,\mathrm{min}$. The ACK packet loss is $11\,\%$ and $14\,\%$ from the two buoys, respectively. At the passive buoy side, packet loss results in $10\,\%$ loss of TDOA measurement. The overall RMSE of the passive buoy position is $0.95\,\mathrm{m}$. A position offset from the passive buoy position estimates to its GNSS position can be observed, though the reason cannot be directly inferred due to many measured data with uncertainties, e.g. the range measurement uncertainty that is affected by TOF accuracy, sound speed accuracy and the bias due to the movement of the BlueROV2 which is not compensated by the localization algorithm. Moreover, the TDOA measurement is acquired by using the sampling counts of the start of received POLL and ACK packet provided by the modem firmware, whose accuracy is not determined yet in this work. Other factors include the uncertainty of the buoy and BlueROV2 GNSS positions which comes from the possible misaligned position between the GNSS antenna and the ahoi modem due the tilting of the mounting structure.

V. Conclusion and Outlook

In this work a passive localization method is proposed and tested for underwater swarm vehicles using the low-cost ahoi modem. The localization accuracy of both the simulation and the real-world experiment can be potentially improved by applying the extended Kalman filter (EKF) which compensates for the ranging error introduced by the AAUV movement. For the real-world experiment result, the higher overall position error compared to the simulation as well as the estimation offset is reasonable due to more measurement uncertainties involved, which requires future investigation for each error source mentioned above. Succeeding work will aim at error source analysis and filtering method for improving the localization accuracy, as well as integration with Robot Operating System (ROS) as a real-time passive self-localization system.

References

[1] Y. Jiang and B.-C. Renner, "Low-cost underwater swarm acoustic localization: A review," *IEEE Access*, vol. 12, pp. 25 779–25 796, 2024.
[2] A. Munafò and G. Ferri, "An acoustic network navigation system," *Journal of Field Robotics*, vol. 34, no. 7, pp. 1332–1351, mar 2017.
[3] A. Quraishi, A. Bahr, F. Schill, and A. Martinoli, "A flexible navigation support system for a team of underwater robots," in *2019 International Symposium on Multi-Robot and Multi-Agent Systems (MRS)*. IEEE, aug 2019.
[4] C. Busse and B.-C. Renner, "Towards accurate positioning of underwater vehicles using low-cost acoustic modems," in *2022 International Conference on Robotics and Automation (ICRA)*. IEEE, may 2022.
[5] A. Hinduja, Y. Ohm, J. Liao, C. Majidi, and M. Kaess, "Acoustic localization and communication using a mems microphone for low-cost and low-power bio-inspired underwater robots," in *2022 IEEE/RSJ International Conference on Intelligent Robots and Systems (IROS)*, 2022, pp. 5470–5477.
[6] A. R. Geist, A. Hackbarth, E. Kreuzer, V. Rausch, M. Sankur, and E. Solowjow, "Towards a hyperbolic acoustic one-way localization system for underwater swarm robotics," in *2016 IEEE International Conference on Robotics and Automation (ICRA)*. IEEE, may 2016.
[7] R. Masiero, S. Azad, F. Favaro, M. Petrani, G. Toso, F. Guerra, P. Casari, and M. Zorzi, "DESERT underwater: An NS-miracle-based framework to design, simulate, emulate and realize test-beds for underwater network protocols," in *2012 Oceans - Yeosu*. IEEE, may 2012.
[8] "Bluerov2," available online: https://bluerobotics.com/product-category/rov/bluerov2/ (accessed on 17 April 2024). [Online]. Available: https://bluerobotics.com/product-category/rov/bluerov2/
[9] F. Dellaert and G. Contributors, "borglab/gtsam," May 2022. [Online]. Available: https://github.com/borglab/gtsam)
[10] B.-C. Renner, J. Heitmann, and F. Steinmetz, "ahoi," *ACM Transactions on Sensor Networks*, vol. 16, no. 2, pp. 1–46, jan 2020.

Sensor Fusion for Object Localization with ROS 2

Jan-Philipp Schreiter* and Horst Hellbrück*
* Luebeck University of Applied Sciences, Germany
Department of Electrical Engineering and Computer Science
Email: jan-philipp.schreiter, horst.hellbrueck@th-luebeck.de

***Abstract*—The combination of camera and LiDAR technologies is crucial in autonomous systems. This paper presents an approach on the fusion of these two sensor modalities, with the aim of improving the accuracy and dependability of obstacle detection and localization. With advanced camera-LiDAR calibration method in the ROS 2 Humble framework, we implemented sensor fusion between high-resolution images of a camera and accurate depth measurements of LiDAR.**

***Index Terms*—Object detection, obstacle localization**

I. Introduction

Autonomous systems represent a significant milestone in development of transportation, both on land and across inland waterways. These systems introduce a new era where machines can perceive and interact with their environment independently. Precise object detection or obstacle localization is essential for ensuring safe and efficient operation of these systems. The limitations of traditional single-modality sensors in complex and dynamic environments are well-known, e.g. low light performance of cameras. However, there are more sophisticated solutions available. The fusion of camera and LiDAR sensors is a particularly promising approach. By combining high-resolution visual data from cameras with precise depth information from LiDAR, a comprehensive spatial understanding of the surroundings can be achieved. The presented approach in this paper uses camera and LiDAR fusion in combination with AI detection for object localization in real-world applications.

This paper begins by exploring the current methods of sensor fusion in ROS 2 Humble. We then discuss the methodologies employed in the calibration and alignment of camera and LiDAR data and its integration within ROS 2.

II. Related Work

Various fusion techniques have been proposed to enhance object detection accuracy and distance measurement precision, showcasing the potential of integrating camera and LiDAR data for improved 3D object detection systems. Kumar et al. highlighted the benefits of combining camera and LiDAR outputs for object detection and distance estimation in self-driving vehicles [1]. Caltagirone et al. demonstrate the potential of LiDAR-camera fusion to significantly improve semantic segmentation through the use of both supervised and semi-supervised learning in their study [2]. Liu et al. addressed the challenge of real-time object detection for autonomous driving by proposing a LiDAR-camera-based fusion algorithm [3]. Long et al. presented a multi-sensor data fusion system based on polarization color stereo cameras and LiDAR resulting in a robust perception system [4]. Further research include a novel multi-modal Multi-Object Tracking (MOT) algorithm for self-driving cars that combined camera and LiDAR data [5] as well as raw data LiDAR and camera fusion in real-time for obstacle detection [6].

These studies underscore the importance of camera-LiDAR fusion in advancing perception capabilities for autonomous systems. For the fusion of raw data several methods are available. A collection of papers and toolboxes can be found at Awesome-LiDAR-Camera-Calibration [7] which is part of the awesome curation [8]. These are mainly dividable into target-based and targetless methods. The calibration targets for target-based methods range from checkerboard, chessboard, cardboard, aruco or a combination of the mentioned targets. The targetless methods are based on motion or scene using traditional algorithms or deep learning to calibrate the sensors. The tools on the list vary from applications in Matlab, ROS or pytorch to stand-alone applications based on Linux.

In line with the goals of using ROS 2 integrating camera and LiDAR sensor and performing data processing, only a few tools from the list meet the requirements. Considering this lidar2camera [9] from SensorsCalibration toolbox by Open calib [10] and the targetless direct_visual_lidar_calibration [11] are the most promising for this project.

III. Idea

The fusion of camera and LiDAR sensors holds immense promise for advancing perception systems in various domains. By calibrating these complementary sensors, we achieve precise alignment, allowing us to seamlessly integrate their data streams. The LiDAR sensor provides a dense point cloud representation of the environment, capturing accurate depth information. Simultaneously, the camera captures high-resolution visual imagery, offering rich contextual details. By associating image pixel with the corresponding LiDAR measurements, we can accurately estimate the distance to the object. This fusion approach enhances the robustness of our perception system, enabling solution for real-world applications such as autonomous navigation and collision avoidance.

IV. Implementation

The following section covers the integration of hardware and software systems providing an in-depth examination of the technological underpinnings that constitute the core of

our approach. The implementation is carried out on a Nvidia Jetson Orin AGX developement kit running Ubuntu 20.04 where camera and LiDAR serve as the primary data acquisition sources connected via Ethernet.

A. Sensors

Camera-LiDAR fusion involves the alignment of two disparate sensor modalities to create a cohesive data representation of the environment. Two primary sensors are utilized: camera and LiDAR. The Camera Hik Vision DS-2CD2T47G2-LSU/SL capturing high-resolution visual data that provides rich texture and color information about the environment crucial for identifying and classifying objects based on their appearance. The captured image from the measuring run is shown in Figure 1. LiDAR sensor RoboSense RS-LIDAR-M1 offers a different set of capabilities. By emitting pulses of laser light with 905nm and measuring the time it takes for the reflection to return, the distance to objects is calculated with high precision. This depth information is essential for determining the exact distance and relative position of obstacles. An example point cloud representation of the environment shown in Figure 1 is displayed in Figure 2.

Fig. 1: Camera Image

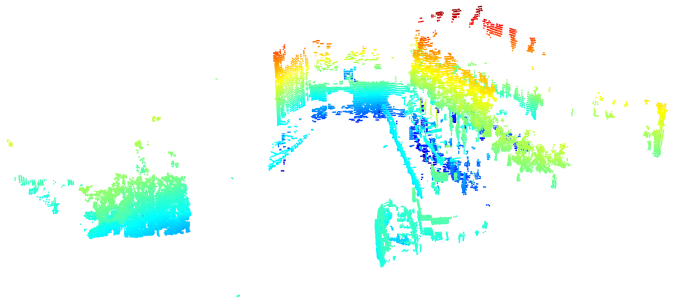

Fig. 2: Point Cloud

With regard to the field of view (FoV), the measurement is confined to the area where both FoVs overlap. Conversely, the detection is solely within the camera's FoV. With 120° the LiDAR has a slightly wider horizontal FoV compared to the camera's 111.9°. However, its vertical FoV with 25° is significantly narrower (60.5° for camera), focusing the distance measurement on a smaller vertical slice of the environment.

B. ROS 2

Our implementation is based on the highly versatile Robot Operation System 2 (ROS 2) Humble, which is specifically designed to support the creation of autonomous systems and robots. Its middleware, the Data Distribution Service (DDS) excels in meeting the demands for dependable and effective data exchange, managing data transfer, synchronization, and message routing among software components. DDS introduces priorities for critical messages, ensuring communication with low latency and meeting Quality of Service (QoS) requirements tailored to specific application needs. ROS 2 Humble is a crucial component that provides the required flexibility and scalability for effortless sensor integration, distributed processing, and efficient communication. The modular development paradigm advocated by ROS 2 facilitates integration, reusability and maintainability, enabling the autonomous creation of software components for sensors, control systems and communication modules.

In order to facilitate the implementation of sensor components and calibration tools in ROS 2 nodes, a system was devised which employed publisher nodes for camera [1] and LiDAR [2] data, and subscriber nodes for intrinsic camera calibration and rectification [3]. The extrinsic camera-LiDAR calibration [4] is also based on ROS 2 leveraging recorded bag files storing camera and LiDAR data. The usage of ROS 2 bags for calibration reduces the amount of steps needed for an accurate calibration. Additionally the calibration is performed on the device itself with no need for installing additional programs.

C. Camera LiDAR Calibration

To establish the internal parameters of the camera and LiDAR sensors, the process of calibration begins with intrinsic calibration. In order to perform intrinsic camera calibration, the camera_calibrator node from the image_pipeline package in ROS 2 is used. The node subscribes to raw image topics and presents a calibration window. The calibration is performed with the help of a checkerboard. The calibration parameters are computed as OpenCV calibration functions [5]. The image processing is performed by the image_pipeline component image_proc, which transforms an original distorted camera image into a rectified, de-Bayered, and undistorted image. As illustrated in Figure 3, the rectified camera image shows a significant reduction in distortion compared to the original raw sensor output (Figute 1), with the rooftop line now appearing straight and level, indicating the successful correction of the previous optical distortions.

[1] https://github.com/surfertas/ros2_ipcamera
[2] https://github.com/RoboSenseLiDAR/rslidar_sdk
[3] https://github.com/rosperception/image_pipeline
[4] https://github.com/koide3/direct_visual_lidar_calibration
[5] https://docs.opencv.org/4.5.4/d9/d0c/group__calib3d.html

Fig. 3: Rectified Image

Fig. 4: Camera Lidar Fusion

The sensors undergo extrinsic calibration to determine their relative rotation and translation. The direct_visual_lidar_calibration method simplifies this process by providing a general LiDAR-camera calibration toolbox. The transformation estimation between the LiDAR and camera is achieved through RANSAC with manually selected key points based on the previously recorded bag files. It is worth noting that this calibration is targetless. By inverting the transformation matrix the LiDAR point cloud is projected from 3D space into the 2D image plane. Once calibrated, the fused camera-LiDAR data can be used for specific point depth measurement.

V. Evaluation

Despite the presence of one missing segment in the LiDAR scanner, our evaluation of the camera-LIDAR fusion system on the Trave River in Lübeck yielded promising results. The prototype sensor box, comprising camera and a LiDAR scanner, was successfully deployed on an electric boat to conduct a measuring run along the riverbank. Despite the partial loss of LiDAR data, the system demonstrated robust performance in resolution enabling identifying relevant obstacles such as bridges and the harbor wall. The fusion between camera and LiDAR is illustrated in Figure 4 showing the projected point cloud on the rectified camera image. Furthermore, the fusion of camera and LiDAR data enabled accurate estimation of distance, allowing for effective navigation based on visual sensors. These results demonstrate the potential of our prototype system to provide reliable and accurate environmental perception in various aquatic environments.

VI. Conclusion and Future Work

In conclusion, our evaluation of the camera-LIDAR fusion system on the Trave River in Lübeck has demonstrated its potential to provide accurate and robust environmental perception in various aquatic environments. Despite being a basic visual-based evaluation, the fusion marks a significant achievement in remote sensing and autonomous navigation in the context of our project. To further evaluate the precision of the overlap between camera and LiDAR data, specific targets and a reference measurement system will be necessary. Future studies should focus on refining this technology to integrate it into diverse applications, setting a new standard for sensor-based environmental perception. The success of this project serves as a testament to the transformative potential of integrating multiple sensor modalities, paving the way for future innovations in the realm of intelligent systems.

Acknowledgments

This publication is a result of the research of the Center of Excellence CoSA and funded by the Federal Ministry for Digital and Transport of the Federal Republic of Germany (Id 19F2225C, DAVE). The joint project is managed by VDI VDE IT. Horst Hellbrück is adjunct professor at the Institute of Telematics of University of Lübeck.

References

[1] G. A. Kumar, J. H. Lee, J. Hwang, J. Park, S. H. Youn, and S. Kwon, "Lidar and camera fusion approach for object distance estimation in self-driving vehicles," *Symmetry*, vol. 12, no. 2, 2020. [Online]. Available: https://www.mdpi.com/2073-8994/12/2/324

[2] L. Caltagirone, M. Bellone, L. Svensson, M. Wahde, and R. Sell, "Lidar–camera semi-supervised learning for semantic segmentation," *Sensors*, vol. 21, no. 14, 2021. [Online]. Available: https://www.mdpi.com/1424-8220/21/14/4813

[3] H. Liu, C. Wu, and H. Wang, "Real time object detection using lidar and camera fusion for autonomous driving," *Scientific Reports*, vol. 13, 05 2023.

[4] N. Long, H. Yan, L. Wang, H. Li, and Q. Yang, "Unifying obstacle detection, recognition, and fusion based on the polarization color stereo camera and lidar for the adas," *Sensors (Basel, Switzerland)*, vol. 22, no. 7, p. 2453, March 2022. [Online]. Available: https://europepmc.org/articles/PMC9003213

[5] R. Pieroni, S. Specchia, M. Corno, and S. M. Savaresi, "Multi-object tracking with camera-lidar fusion for autonomous driving," 2024.

[6] A. Thakur and P. Rajalakshmi, "Lidar and camera raw data sensor fusion in real-time for obstacle detection," in *2023 IEEE Sensors Applications Symposium (SAS)*, 2023, pp. 1–6.

[7] Deephome, "Awesome-lidar-camera-calibration." [Online]. Available: https://github.com/Deephome/Awesome-LiDAR-Camera-Calibration

[8] S. Sorhus, "awesome." [Online]. Available: https://github.com/sindresorhus/awesome

[9] T. Ma, Z. Liu, G. Yan, and Y. Li, "Crlf: Automatic calibration and refinement based on line feature for lidar and camera in road scenes," 2021.

[10] G. Yan, Z. Liu, C. Wang, C. Shi, P. Wei, X. Cai, T. Ma, Z. Liu, Z. Zhong, Y. Liu, M. Zhao, Z. Ma, and Y. Li, "Opencalib: A multi-sensor calibration toolbox for autonomous driving," *arXiv preprint arXiv:2205.14087*, 2022.

[11] K. Koide, S. Oishi, M. Yokozuka, and A. Banno, "General, single-shot, target-less, and automatic lidar-camera extrinsic calibration toolbox," 2023.

Enhancing Collaborative Robots with Integration of a Depth Camera and Object Detection

Ole Hendrik Sellhorn* and Horst Hellbrück*
*Department EI, Center of Excellence CoSA
Technische Hochschule Lübeck - University of Applied Sciences, Lübeck, Germany
ole.sellhorn@th-luebeck.de, horst.hellbrueck@th-luebeck.de

***Abstract*—This paper explores the feasibility of enhancing collaborative robots (Cobots) to perceive their environment autonomously. By integrating a single camera and artificial intelligence (AI) image detection, the Cobot can accurately detect and locate objects in three-dimensional space. The study investigates the use of Microsoft's Kinect for cost-effective depth perception and the implementation of YOLOv4 object detection to recognize specific objects. Experimental results demonstrate the reliability of the proposed approach in detecting and localizing objects, such as pencils, within the Cobot's workspace.**

Challenges, including automatic coordinate output and coordinate system translation, are discussed, along with potential future directions for research, such as multi-camera integration and further development of the image AI for diverse object detection tasks. The significance of this research lies in its contribution to the advancement of collaborative robotics, offering practical solutions for improving efficiency and safety in industrial and service applications. Practical implications include the potential automation of assembly processes and enhanced quality control measures, underscoring the transformative potential of autonomous perception in collaborative robot systems

***Index Terms*—Collaborative Robotics, Depth Perception, object detection, Microsoft Kinect, YOLOv4, Object Localization**

I. Introduction

In today's rapidly evolving industrial landscape, collaborative robots (Cobots) have emerged as transformative tools, offering unparalleled versatility and efficiency in various manufacturing and service sectors. Unlike traditional robots, Cobots are designed to work alongside human counterparts, augmenting human capabilities, and facilitating collaboration. Their increasing prominence underscores a paradigm shift towards human-robot interaction, promising enhanced productivity and safety in diverse work environments [1].

Amidst the growing adoption of Cobots, configuring these systems presents a multifaceted challenge for researchers and practitioners alike. The selection of optimal configurations hinges on a myriad of factors, ranging from budgetary constraints to task-specific requirements. At the heart of this configurational dilemma lies the integration of sensors and AI, which holds the key to unlocking the full potential of Cobots in perceiving and interacting with their surroundings [2].

II. Methodology

The challenge of reliably perceiving a three-dimensional space using a single camera to accurately determine the position of an object presents a obstacle. To address this challenge, we adopted Microsoft's Kinect as our approach—an innovative sensor platform renowned for its unique technical specifications. The Kinect's standout feature lies in its affordability, coupled with its built-in infrared and depth camera capabilities [3]. Leveraging the depth camera option, it becomes feasible to detect the position of an object within a three-dimensional space using a single camera setup. This functionality is achieved through the measurement of light signals' runtime. The camera emits light pulses and measures the time it takes for the light to reflect and return to the sensor [4].

The next challenge entails developing a methodology to recognize and detect only the desired object. In the context of our research, the current target object—such as a pencil intended for pickup by the Cobot—poses a critical obstacle. To overcome this challenge, we utilized a prevalent object detection, You Only Look Once version 4 (YOLOv4), as our foundational tool and augmented it with additional data. object detection, in general, must be trained on specific objects of interest. It functions similarly to a human brain, discerning which features are crucial for object identification using a neural network [5]. YOLOv4 boasts high-speed and precise object recognition capabilities. One of YOLO's key advantages is its ability to process up to 155 images per second, depending on the desired level of accuracy. YOLO operates by initially dividing the image into a grid. Each grid cell is examined to determine if an object is present within it. As seen in Figure 1, bounding boxes are drawn around detected objects, and these are then reduced to a single box per object, retaining only those that the model believes best delineate the object [6].

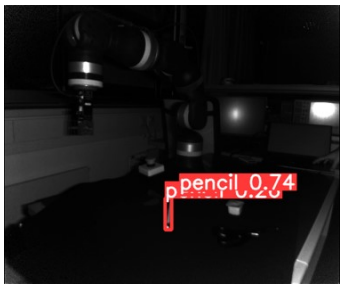

Fig. 1. object detection

The images used for training and validation were captured using the Kinect in typical operational scenarios. The image

detection process generates a bounding box, such as around a pencil in this case, to locate the object accurately. The camera can determine the precise three-dimensional position of this bounding box.

III. Experiments and Results

Figure 2 outlines the functional concept of our current setup. It involves the Cobot being connected to a computer via IPv4 with a static IP address, ensuring stable communication between the devices. The connection between the computer and the Kinect is established via USB. A driver installation is required to facilitate this connection. Similarly, the communication between the computer and the Kinect follows the USB protocol, requiring driver installation for compatibility. Interface integration enables the user interface of the Cobot to support easy camera integration. Subsequently, the computer is connected to the Kinect via USB, which is directed towards the Cobot's workspace. The camera is then initiated using a program that can start the camera as a virtual device, allowing its usage within a Python environment. In our setup, we utilize the OBS broadcaster software [7] for this purpose, as it provides a suitable interface for configuring a camera. An additional advantage is the availability of plugins that simplifies the integration process.

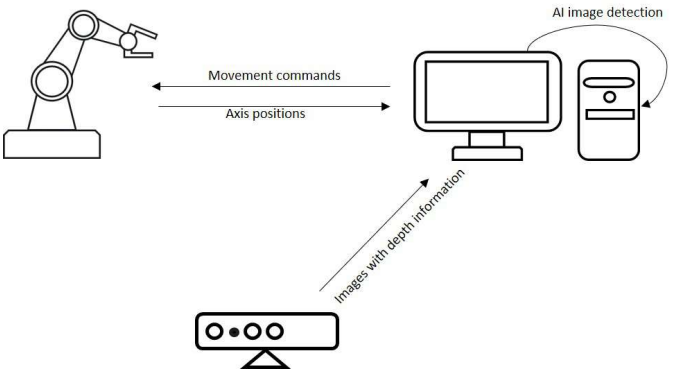

Fig. 2. Functional concept of the setup

For the output of coordinates, a script has been developed to access live detection and, upon clicking, retrieve the coordinates of the click from the camera's perspective. This enables the precise reproduction of the bounding box's exact position. Various camera angles covering the entire workspace were tested to assess the image detection system's performance. The testing encompassed different lighting conditions, including normal room lighting, sunlight, artificial lighting, and darkness. Results showed that uniform illumination across the workspace yielded optimal performance. The image detection system was tested under various camera angles and lighting conditions. The results indicate that detection works in the majority of cases.

Following the functional concept, we provide a visual representation of our actual setup, as depicted in Figure 3. The laptop is located under the platform on which the Cobot is installed.

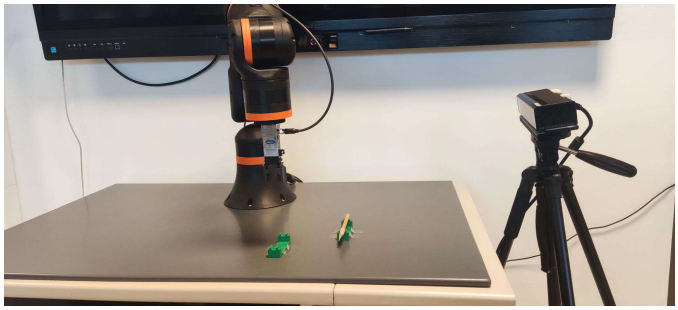

Fig. 3. Experimental setup

Currently, the infrared camera is utilized for detection purposes. This decision is based on the fact that the infrared and depth cameras share the same position, whereas the regular camera is slightly offset, resulting in the coordinates from the depth camera being slightly offset from those of the standard camera. However, it is noted that this choice may affect color accuracy. This aspect is slated for future improvement, as mentioned in the "Future Work" section. Further investigation into the potential identification of objects other than the target pencil by the infrared camera is deferred to subsequent sections for comprehensive discussion.

IV. Conclusion and Future Work

While our initial results are promising, several challenges remain for the continued advancement of this project. Currently, the output of coordinates relies on manual interaction with the bounding box, necessitating further efforts towards automating this process. Future work includes the development of a script to automate the central positioning of the bounding box, eliminating the need for manual interaction. Various methods for achieving this automation will be evaluated to determine the most effective approach. As previously mentioned, it is crucial to capture images using a standard camera instead of the depth camera. This approach increases the robustness of the AI system and reduces its susceptibility to variations in lighting conditions. This requires a translation of coordinates between the depth camera and the standard camera.

Additionally, determining the optimal grasping location for the Cobot and addressing the translation between the camera's coordinate system and the Cobot's coordinate system are essential for enabling reliable robotic movements. The challenge lies in determining the optimal grasping point for the Cobot, as it varies between devices. If automated bounding box positioning does not yield satisfactory results, alternative methods, such as training the image AI specifically for grasping points, will be explored.

Furthermore, future research avenues include expanding the capabilities of our image AI to detect multiple objects and integrating it with other AI systems capable of autonomously learning assembly instructions. Once the issues with image detection are resolved, the possibilities are limitless. For instance, AI could be trained on various assembly instructions with different tools. The image AI would identify the tools,

while another AI could evaluate the type of assembly and execute the instructions accordingly.

The implementation of these proposed improvements and advancements will enhance the capabilities of the system, paving the way for broader applications in robotics and artificial intelligence.

ACKNOWLEDGMENTS

This publication results from the research of the Center of Excellence CoSA at the University of Applied Sciences Lübeck. Horst Hellbrück is an adjunct professor at the Institute of Telematics of the University of Lübeck.

REFERENCES

[1] M. Javaid, A. Haleem, R. P. Singh, S. Rab, and R. Suman, "Significant applications of cobots in the field of manufacturing," *Cognitive Robotics*, vol. 2, pp. 222–233, 2022. [Online]. Available: https://www.sciencedirect.com/science/article/pii/S2667241322000209

[2] A. Hentout, A. Mustapha, A. Maoudj, and I. Akli, "Key challenges and open issues of industrial collaborative robotics," 08 2018.

[3] L. Yang, L. Zhang, H. Dong, A. Alelaiwi, and A. El Saddik, "Evaluating and improving the depth accuracy of kinect for windows v2," *IEEE Sensors Journal*, vol. 15, no. 8, p. 4275–4285, Aug. 2015. [Online]. Available: http://dx.doi.org/10.1109/JSEN.2015.2416651

[4] R. Horaud, M. Hansard, G. Evangelidis, and C. Ménier, "An overview of depth cameras and range scanners based on time-of-flight technologies," *Machine Vision and Applications*, vol. 27, no. 7, p. 1005–1020, Jun. 2016. [Online]. Available: http://dx.doi.org/10.1007/s00138-016-0784-4

[5] Y. Tian, "Artificial intelligence image recognition method based on convolutional neural network algorithm," *IEEE Access*, vol. PP, pp. 1–1, 06 2020.

[6] A. Bochkovskiy, C.-Y. Wang, and H.-Y. M. Liao, "Yolov4: Optimal speed and accuracy of object detection," 2020.

[7] P. W. Richards, "The unofficial guide to open broadcaster software," *The Unofficial Guide to OBS*, 2021.

System Architecture and Hardware Interconnects for an Adaptable 77-81 GHz FMCW Radar

Maximilian Gottfried Becker*, Naglaa El Agroudy*, Marco Gunia*, Frank Ellinger*‡
*Chair for Circuit Design and Network Theory, Technische Universität Dresden, Germany
‡Centre for Tactile Internet with Human-in-the-Loop (CeTI), Technische Universität Dresden, Germany
Email: maximilian_gottfried.becker@tu-dresden.de

***Abstract*— In this paper, a work-in-progress hardware concept for a millimeter-wave (mmWave) frequency-modulated continuous-wave (FMCW) radar system is presented. Separate, individual application specific integrated circuits (ASICs) and a substrate-integrated waveguide (SIW) antenna design allow flexible configuration of the system, especially with regard to the number of transmit/receive paths. A major challenge in this mmWave frequency range is signal distribution, not only within an ASIC or printed circuit board (PCB), but especially between ASIC and PCB or SIW antenna. Hence, necessary interconnects are considered in details and multiple concepts are presented.**

***Index Terms*—bondwire interconnections, mm-wave, radar**

I. Introduction

Contributing towards the goal of reaching zero road deaths by 2050 in the EU, the project NextPerception investigates on systems for detection of vulnerable road users (VRUs), particularly pedestrians. Millimeter-wave (mmWave) frequency-modulated continuous-wave (FMCW) radar has emerged as an attractive solution to detect VRUs at intersections [1]. For this, adaptable and compact radar hardware is desired. Systems at lower frequencies can be arranged flexibly due to cable based interconnects but tend to be bulky, e.g. [2]. On the other hand, highly integrated systems in the sub-THz range have very limited range [3]. The V- and W-band can represent an attractive compromise [4], but requires careful design of radio frequency (RF) interconnects.

This paper proposes a work-in-progress system architecture for a $77\,\mathrm{GHz}$ to $81\,\mathrm{GHz}$ pedestrian detection FMCW radar, describes the considerations on and implementation of the RF interconnects and provides work-in-progress results.

II. System Structure

An overview of the proposed hardware system divided into two parts is given in Fig. 1. The first part is dedicated to generating the necessary frequency sweep at an intermediate frequency (IF) as well as the baseband processing of the received signal. The second part is dedicated to the mmWave front end with application specific integrated circuits (ASICs) for transmission (TX) and reception (RX) and a custom substrate-integrated waveguide (SIW) antenna design. By placing multiple TX/RX pairs with highly-directive high-gain antennas facing in different non-overlapping directions, a larger combined range (distance or angle) can be covered and coarse angle estimation of targets is possible. The front end may therefore be implemented on a flexible printed circuit board (PCB) or composed of multiple TRX PCBs, each containing one TX/RX pair with antennas. An arbitrary number of pairs can be supplied with one generator in a daisy-chain topology. The system is complemented by a digital control board featuring microcontroller, field-programmable gate array (FPGA) and analog-to-digital converters (ADCs).

The FMCW signal for TX and RX is generated at the IF $f_{\mathrm{IF}} = 25.66\,\mathrm{GHz}$ to $27\,\mathrm{GHz}$ because PCB-based grounded coplanar waveguides (G-CPWs) as well as cables and connectors required for signal distribution have lower attenuation at this frequency than at the radio frequency $f_{\mathrm{RF}} = 77\,\mathrm{GHz}$ to $81\,\mathrm{GHz}$. For this, a commercial off-the-shelf (COTS) ADF4169 frequency synthesizer from Analog Devices is combined with a specifically designed voltage-controlled oscillator (VCO) ASIC presented in [5]. The VCO outputs both the IF signal and a divide-by-two signal for the ADF4169, which has a maximum input frequency of only $13.5\,\mathrm{GHz}$. An active loop filter is necessary to reach the required voltage tuning range $V_{\mathrm{tune}} = 1.7\,\mathrm{V}$ to $4\,\mathrm{V}$ of the VCO. Based on simulation, the active filter increases noise by only $5\,\mathrm{dBc/Hz}$ above $100\,\mathrm{kHz}$ offset compared to a passive filter.

The mmWave front end is realized as two separate ASICs. The transmitter features a frequency tripler that converts the FMCW signal from f_{IF} to f_{RF}. The resulting differential RF-signal is subsequently split to two single-ended paths. One is amplified to $13\,\mathrm{dBm}$ by a power amplifier (PA) based on a modified design of [6] for transmission. The second is buffered and fed to the receiver as local oscillator (LO)-signal for down-mixing the received signal reflected by the target to determine the frequency offset which is proportional to the distance. Furthermore, the ASIC provides a buffered output of the IF signal for subsequent TX/RX pair in a daisy-chain topology. Reception is realized by a zero-IF receiver in a mixer first architecture based on a Gilbert cell. The baseband signal is processed on PCB with COTS components. The SIW slot antenna shown in Fig. 2a is realized on $787\,\mu\mathrm{m}$ Rogers Duroid 5880 substrate. It is optimized for a high gain around $13\,\mathrm{dBi}$ and a narrow half-power beamwidth (HPBW) of $44°$ in azimuth and $28°$ in elevation.

III. RF signal distribution and interconnects

To realize the proposed system, three crucial signal interconnects at mmWave have to be implemented: Connecting the IF signal from PCB to the TRX ASIC at around $26\,\mathrm{GHz}$

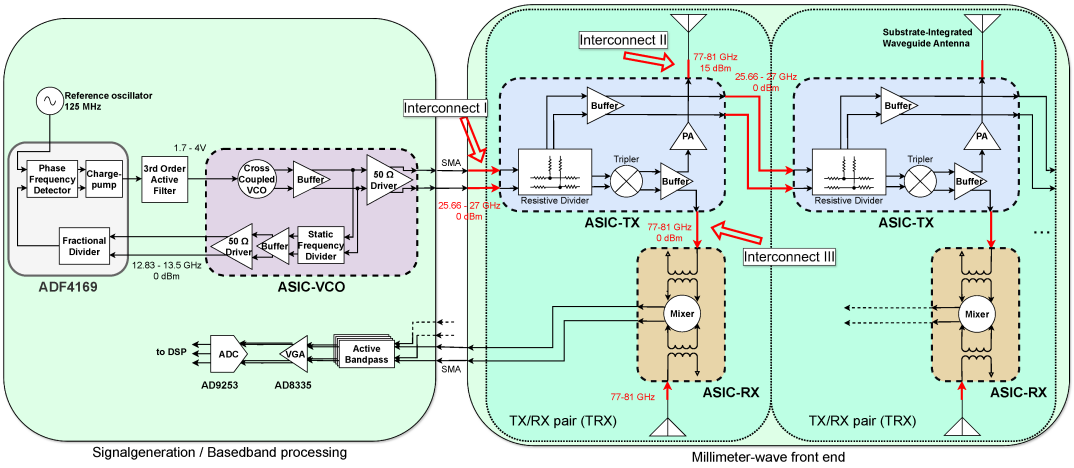

Fig. 1. Proposed system overview with two TX/RX pairs shown.

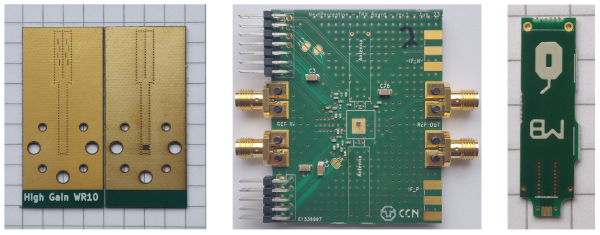

(a) (b) (c)

Fig. 2. (a) SIW antenna with simple WR10 interface for characterization, (b) initial TRX board for individual characterization with TX ASIC assembled and (c) dummy antenna for assembly proof of concept.

(Interconnect I), transferring the signal between TX/RX ASIC and the SIW of the respective antenna at around 78 GHz (Interconnect II) and feeding the LO-signal from TX ASIC to RX ASIC at the same frequency (Interconnect III). The respective implementations indirectly affect each other due to the mechanical constraints and physical dimensions. All interconnects require a transition from ASIC to a PCB or another ASIC. Here, a bondwire solution is favorable due to flexibility and low cost. Unfortunately, bondwires significantly affect the signal at mmWave. Minimizing their length for example by placing the ASICs in cavities on the PCB is beneficial. Moreover, it is possible to partly compensate their influence by carefully designing a planar matching structure on the PCB [7]. For Interconnect II, an additional transition to the SIW antenna is necessary. State-of-the-art G-CPW-to-SIW transitions achieve an insertion loss between 0.5 dB and 1 dB below 30 GHz [8], [9]. Furthermore, it is necessary to either implement a connection between TRX PCB and an antenna PCB or to integrate both into one PCB.

Four approaches to integrate the components and implement these interconnects are evaluated:

1) Integrate the antennas into TRX PCB and place ASICs into cavities. Use direct bondwire onto combined PCB or between ASICs for Interconnect II and III, respectively.
2) Attach separate antenna PCBs to TRX PCB and place ASICs into cavities. Realize indirect bondwire connection via compensation structure on TRX PCB for Interconnects II and III.
3) Attach separate antenna PCBs to TRX PCB. Use direct bondwire onto antenna PCB or between ASICs for Interconnects II and III, respectively.
4) Attach separate antenna PCBs to TRX PCB with direct copper contact (see below) for Interconnect II combined with bondwire compensation on TRX PCB. Use direct bondwire between ASICs for Interconnect III.

TABLE I
COMPARISON OF INTEGRATION APPROACHES

Approach	1	2	3	4
Bondwire count[1]	1	2	1	1
Bondwire length[1]	short	medium	long	short
Bondwire compensation	no	partly[2]	no	partly[3]
Assembly	easy	medium	medium	difficult

[1] Maximum across interconnects
[2] Only for LO-signal between TX and RX antenna
[3] Only for TX/RX to

Interconnect I is always realized by bondwire to a G-CPW without compensation due to the lower frequency. Interconnect II is always concluded by a G-CPW-to-SIW transition to feed the antenna. A comparison between these approaches regarding Interconnects II and III is given in Table I. Approach 1 is the easiest to assemble and requires only short bondwires. However, on the stackup predefined by the designed SIW antenna, it is difficult to realize compact highly-capacitive structures, which prohibits implementing bondwire compensation like proposed in [7]. The uncompensated bondwires result in 4 dB to 5 dB insertion loss at both interconnects according to simulations. In approach 2, the thickness of the antenna PCB results in a long bondwire that is difficult to compensate. In approach 3,

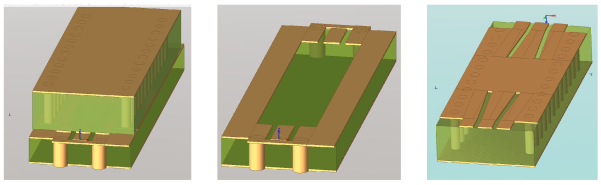

(a) (b) (c)

Fig. 3. Two back-to-back transition from G-CPW on TRX PCB to G-CPW on dummy antenna PCB to SIW: (a) Combined, (b) TRX PCB, dummy SIW antenna PCB (flipped view).

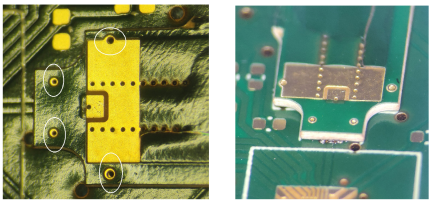

(a) (b)

Fig. 4. PCB to PCB interconnect evaluation for antenna assembly: (a) Top view with vias for alignment and (b) side view of gap between PCBs.

the bondwire leading to the antenna is even longer because the antenna PCB must be located 1 mm away from the ASIC to be able to bond the remaining pads. Approach 4 is considered in detail below.

The main challenge here is Interconnect II, which includes the bondwire from ASIC to TRX, the direct copper contact between G-CPW on TRX PCB and G-CPW on antenna PCB and the subsequent transition into the SIW. The best design achieved so far is centered around a triangular tapered G-CPW-to-SIW transition [9]. For evaluation, it is electromagnetic (EM)-simulated as two back-to-back transitions excluding the bondwire as shown in Fig. 3 and this results in an insertion loss of 3 dB attributed to a single transition over the relevant frequency range. More sophisticated structures like the V-slot structure in [9] or the transition presented in [8] are not feasible due to the small wavelength and the PCB minimum spacing/width design rules. To evaluate the feasibility of this concept and to individually characterize the ASICs on a wafer prober with and without Interconnect III, an initial TRX PCB shown in Fig. 2b is designed. Additionally, an antenna dummy shown in Fig. 2c is manufactured for initial mechanical and DC tests of Interconnect II. The dummy antenna can be aligned to the TRX PCB by via holes in both PCBs as shown in Fig. 4a and an electrical connection is established by placing solder paste on the exposed G-CPW and subsequent reflow soldering. However, in this first revision it is not possible to achieve a reliable electrical connection due to a larger than expected gap between PCBs as shown in Fig. 4b. The individual boards are not perfectly flat and the small width and spacing of the G-CPW structure of just 300 µm and 100 µm, respectively, do not allow filling the vertical gap with solder without creating horizontal short circuits. In the next revision, a sequential contact of ground and signal traces will be evaluated to reduce the risk of short circuits. Furthermore, a multi-layer PCB with a heterogeneous layer stack with the antenna may be evaluated, although the necessary vias may be detrimental at mmWave. Regarding Interconnect III, a half-wavelength bondwire [10] may be better than the proposed short connection.

IV. Conclusion and Outlook

In this paper, a flexible system architecture is presented. Individual components may be exchanged or adjusted to suit the application and an arbitrary number of TX/RX pairs can be used. Various approaches to electrically connect the RF components at mmWave have been evaluated, but low-loss interconnects remain challenging. Further measurements and evaluations are necessary to evaluate the full concept. Additionally, another silicon revision may be used to combine TX and RX into a single ASIC to eliminate Interconnect III. To further improve the system, the transmitter PA stage may be replaced by a PA that can be quickly enabled or disabled, e.g. [11]. Thereby, a time-division multiplex (TDM) multiple-input multiple-output (MIMO) radar scheme is possible.

Acknowledgment

This work was supported by the ECSEL Joint Undertaking under grant agreement No 876487 funded by the European Union's Horizon 2020 program and the BMBF (Federal Ministry of Education and Research) project 16MEE0063. We would like to acknowledge the BMBF project 6G-life (16KISK001K) and the DFG (German Research Foundation) project CeTI (390696704) for knowledge exchange.

References

[1] E. Tavanti, A. Rizik, A. Fedeli, D. D. Caviglia, and A. Randazzo, "A short-range FMCW radar-based approach for multi-target human-vehicle detection," *IEEE Trans. Geosci. Remote Sens.*, vol. 60, pp. 1–16, 2022.

[2] W.-C. Su, Y.-C. Lai, T.-S. Horng, and R. E. Arif, "Time-division multiplexing MIMO radar system with self-injection-locking for image hotspot-based monitoring of multiple human vital signs," *IEEE Trans. Microw. Theory Techn.*, vol. 72, no. 3, pp. 1943–1952, Mar. 2024.

[3] T. Jaeschke, C. Bredendiek, S. Kuppers, and N. Pohl, "High-precision D-band FMCW-radar sensor based on a wideband SiGe-transceiver MMIC," *IEEE Trans. Microw. Theory Techn.*, vol. 62, no. 12, pp. 3582–3597, Dec. 2014.

[4] E. Ozturk, D. Genschow, U. Yodprasit, *et al.*, "A 60-GHz SiGe BiCMOS monostatic transceiver for FMCW radar applications," *IEEE Trans. Microw. Theory Techn.*, vol. 65, no. 12, pp. 5309–5323, Dec. 2017.

[5] N. E. Agroudy, M. Becker, B. Al-Qudsi, S. Grover, M. Gunia, and F. Ellinger, "Investigation of a K-band SiGe VCO for FMCW radar localization," in *2023 SBMO/IEEE MTT-S Int. Microw. and Optoelectronics Conf.*, IEEE, Nov. 2023.

[6] M. G. Becker, S. Grover, N. El Agroudy, M. Gunia, and F. Ellinger, "Design and characterization of a 54-76 GHz SiGe power amplifier," in *2024 IEEE 15th Latin Amer. Symp. on Circuits and Syst. (LASCAS)*, Feb. 2024, pp. 1–4.

[7] C.-H. Chan, C.-C. Chou, and H.-R. Chuang, "Integrated packaging design of low-cost bondwire interconnection for 60-GHz CMOS vital-signs radar sensor chip with millimeter-wave planar antenna," *IEEE Trans. Compon. Packag. Manuf. Technol.*, vol. 8, no. 2, pp. 177–185, Feb. 2018.

[8] F. Taringou, D. Dousset, J. Bornemann, and K. Wu, "Substrate-integrated waveguide transitions to planar transmission-line technologies," in *2012 IEEE/MTT-S Int. Microw. Symp. Dig.*, IEEE, Jun. 2012.

[9] D. Lorente, M. Limbach, H. Esteban, and V. Boria, "Compact ultrawideband grounded coplanar waveguide to substrate integrated waveguide tapered V-slot transition," *IEEE Microw. Wireless Compon. Lett.*, vol. 30, no. 12, pp. 1137–1140, Dec. 2020.

[10] R. F. Riaz, F. Protze, C. Hoyer, J. Wagner, and F. Ellinger, "Design and experimental evaluation of 60 GHz self-compensating bond-wire interconnect," in *2023 21st IEEE Interregional NEWCAS Conf. (NEWCAS)*, IEEE, Jun. 2023.

[11] M. G. Becker, M. Gunia, D. Mendez, and F. Ellinger, "Switchable V-band power amplifier with ultra-fast turn-on for aggressive duty-cycling," in *2023 18th Eur. Microw. Integr. Circuits Conf. (EuMIC)*, IEEE, Sep. 2023.

On Reusable Software to Reducing Design Cycles for Positioning Sensors for Embedded Systems

Marco Gunia* and Frank Ellinger*†
*Chair for Circuit Design and Network Theory (CCN) and
†Centre for Tactile Internet with Human-in-the-Loop (CeTI)
Technische Universität Dresden, 01062 Dresden
Email: marco.gunia@tu-dresden.de

***Abstract*—Software for desktops and workstations, i.e. units having sufficient processing resources, is increasingly designed to be variable and extensible, so that changing behaviour is supported and extensions can be included without any modifications to already existing application code. This is contrasted for embedded systems, where memory and computing power are often limited. For such entities, software is highly tailored and modifications often require complete redesign. In the area of positioning and sensors, the paper describes three options for embedded systems that allow software to be reused on the one hand and design and testing time being reduced on the other.**

Keywords*—*Positioning, Localization, Object Oriented Programming, Embedded Systems, Reusable Software, Platform Abstraction Layer, Register Files, Cross-Compiling

I. Introduction

Nowadays, large software projects are primarily subject to Object-Oriented Paradigms (OOP) with the aim of supporting variable behaviour and enabling extensibility for future applications, since these two objectives in particular are difficult to realise using alternative programming techniques. One of the strengths of the OOP is polymorphism, i.e. the ability to treat objects of different (inherited) classes in the same way. On this basis, standard solutions for frequently occurring problems have emerged. These solutions, which are referred to as design patterns, are easy and smart approaches, which are usually not found from the beginning, but which are characterized by providing additional flexibility [1]. In particular, many patterns deal with variability and extensibility. In this regard, we presented a high-level software framework for positioning in [2], which, in addition to these two objectives, also enables arbitrary nesting, uniform interfaces, push / pull behavior and platform independence. Such frameworks are assumed to be run on processing units having sufficient hardware resources.

In contrast, many positioning software is designed for low-level embedded systems employing proprietary hardware. Due to the fact, that computing power and available memory of such entities is limited, implementations are usually subject to procedural programming with hard-coded parameter sets. Thus, the corresponding software libraries are based on customised approaches and are difficult to reuse. We proposed multiple such highly tailored units in [3], [4], [5], [6]. Small changes, e.g. the replacement of some circuit of the sensor, often require the software to be completely redesigned. However, as the performance of the Micro-Controller Units (MCU) for such low-level embedded systems continues to rise, the transition away from the procedural approach is becoming feasible.

Within this paper, we present three innovative methods to enable reuse of low-level positioning software for embedded systems and simplification of its design. These are the creation of virtual register files employing register indexing, the introduction of a Platform Abstraction Layer (PAL), and the set-up of mockup hardware for cross-compiling. While the first two employ OOP to addressing different entities in the same way, the latter allows to reduce time for software engineering and test, as it enables designing on high-performance platforms and eliminating the constantly recurring, time-consuming process of firmware loading onto the embedded system.

II. Related Works

Many works deal with design patterns or complete software framework being variable and extensible for high-level applications where sufficient processing resources are available. For positioning, however, embedded sensor units often only have little memory and computing power. For these entities, much effort is devoted to hardware aspects, e.g. on accuracy, precision, power, infrastructure and costs [7]. Software presented in this context often focuses on data processing algorithms that are customised for a specific application. Only few publications deal with the creation of software that distribute processing to different layers or combine multiple positioning approaches. For instance, [8] introduces the abstract fusion model originating from the US Joint Directors of Laboratories (JDL), consisting of five consecutive levels. On the lowest level 0, incoming sensor data is pre-processed. Coordinate system transformation is applied on level 1. On level 2, the contextual description of the scenario is elaborated. With the help of these results, inferences are drawn at level 3. Finally, system performance is monitored on level 4. Another layered approach for hybrid indoor geolocation with rigid interfaces is [9]. It is restricted to indoor positioning and only enables easy exchange of positioning algorithms. Due to its fixed interfaces and the lack of support for nesting, layered-based concepts are somehow restricted. Alternatives providing more degrees of freedom are cycle-based methods, e.g. the Boyd cycle [10]. Here, the cycle of observation, orientation, decision and action is constantly repeated. The disadvantage is that this is an abstract concept not being tailored for localization.

In contrast, in [2] we presented a hybrid localization framework employing general operators, where complex operators can be composed of simple ones. Positioning algorithms and data processing elements (like filters) are considered as basic elements. This enables natural integration of cumbersome real-

world issues like coordinate transformation or data sampling. All these frameworks are, however, not intended to be running on embedded systems, where processing resources are limited.

Operating Systems (OS) usually address completely different sensors the same way. For example, the Linux OS works with file handles, where entities are addressed by opening, reading, writing, and closing of files [11]. However, this is a very rigid approach with which complex operations are difficult to realise, for instance, switching on a transceiver and configuring a defined transmission frequency.

Various MCU manufacturers now offer high-level access in addition to low-level hardware access at register level, e.g. the Hardware Abstraction Laver (HAL) from ST Microelectronics for *ARM® Cortex®-M7* [12], [13]. For example, devices connected via Universal Asynchronous Receiver Transmitter (UART) can be addressed in the same way by multiple similar MCUs. The same applies to the Serial Peripheral Interface (SPI) or Inter-Integrated Circuit (I2C). However, abstraction to a higher level is not provided, so that selective addressing of devices optionally via UART, SPI or I2C is not possible. Our second method in the next section will do exactly that and enables abstract commands, e.g. output instructions that, depending on the underlying hardware, either print the output on a screen of a host PC, address a terminal via UART, or execute a blinking sequence on Light-Emitting Diodes (LED).

III. Approach

In the following, we present three methods for embedded positioning systems, the first two facilitating software reuse and the last reducing time to market. These concepts can be easily implemented with OOP.

A. Virtual register files employing register indexing

The hardware used in embedded systems is often configured by setting registers. Direct access to these registers or indirect access via corresponding protocols, e.g. UART, SPI or I2C, is common. Hardware components with similar functions often have similar register sets, which differ in the identifiers and the division into fields. For example, transceivers usually offer the option of defining the transmit or receive frequency, whereby the specific register configuration depends on the selected component. For uniform addressing of such units, we recommend the introduction of virtual registers whose configuration provided by the application is converted to the real hardware by register indexing. That indexing can be carried out using configuration files, which indicate the specific allocation for each component. Accordingly, the registers are read using a reverse indexing operation.

The procedure is explained using C++ as an example. The configuration files, realized as C++ header files, are automatically integrated during compilation and contain multiple *define*-statements for each virtual register, which specify its composition from the non-virtual real hardware register fields. Fig. 1 and 2 show a possible virtual register and, for the selected hardware, its composition of two real registers, each containing some of the bits. The coloured numbers in the hardware registers denote the corresponding bit indices in the virtual register and vice versa. Register indexing and its reverse operation is then simply implemented using a general

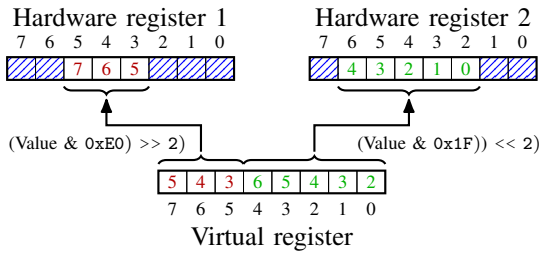

Fig. 1. Example on register indexing for writing data to virtual register

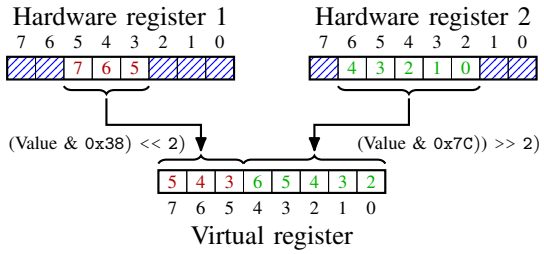

Fig. 2. Example on reverse register indexing for reading data from virtual register

algorithm for assigning virtual registers to the elements of the real registers specified in the configuration file. That universal method operates by masking (&), shifting (>> or <<) and logically adding (|) bits. For the example shown in Fig. 1 on register indexing, the values v_{reg1} and v_{reg2} of the real hardware register are composed from the virtual one as

$$v_{\text{reg1}} = ((v_{\text{virt}} \,\&\, \texttt{0xE0}) \texttt{>>2}) \;,\; v_{\text{reg2}} = ((v_{\text{virt}} \,\&\, \texttt{0x1F}) \texttt{<<2})$$

Note the values of the hardware register that are not to be modified must remain unchanged when writing, i.e. by previously reading the old values and logically combining them with the new values. On the contrary, for inverse register indexing in Fig. 2, the value v_{virt} of the virtual register reads

$$v_{\text{virt}} = ((v_{\text{reg1}} \,\&\, \texttt{0x38}) \texttt{<<2}) \,|\, ((v_{\text{reg2}} \,\&\, \texttt{0x7C}) \texttt{>>2})$$

If the value range of the virtual and real registers differs, the introduction of a multiplication factor is also conceivable.

B. Platform abstraction layer

The PAL is an additional intermediate layer so that the specific implementation of a requirement is separated from its realisation. This is shown using the example of the *template method* design pattern [1] according to Fig. 3 for an instruction to display an argument, i.e. print. Only the primitive operations of the *ConcreteClass* need to be implemented for the respective hardware. The first primitive method could be the output of a character string and the second could deal with printing integers. The display algorithm, which is identical for all hardware, is realised in the method `templateMethod()`. This could initially separate a passing argument into characters and integers and display these in each case using the primitive operations. Depending on the associated hardware, these could now be shown on a host PC or sent to a terminal connected to the embedded system via UART. Alternatively, visualization on LEDs could discard all characters and only show the numbers.

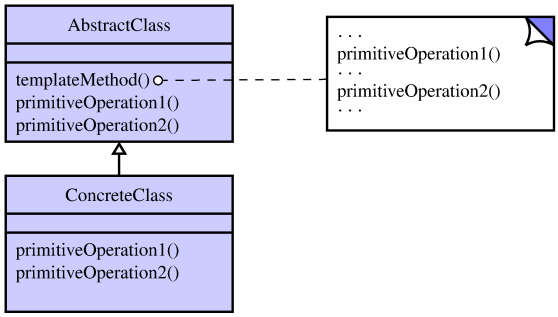

Fig. 3. Template method design pattern (adapted from [1])

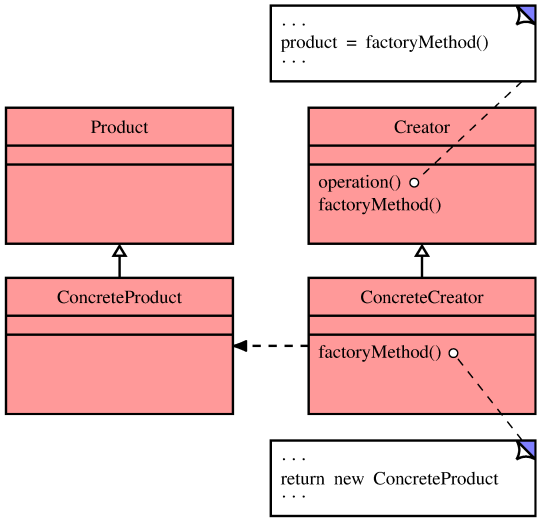

Fig. 4. Factory method design pattern (adapted from [1])

If, instead of primitive operations, complete individual classes tailored to the hardware are required, then realisation using the *factory method* design pattern [1] according to Fig. 4 is an option. All *ConcreateCreator* implemented for the respective hardware generate an object of the type *ConcreteProduct* customised for that hardware. All these are addressed in the same way in the application employing only the interface of the superclass *Product*.

C. Mockup hardware for cross-compiling

The final concept is used to run the software on alternative platforms. Since compiling on these platforms will fail due to the non-existence of specific hardware entities, we propose to introduce a PAL as highlighted in the last section III-B and create mockup code for all hardware. This code will serve as fallback, if specific hardware is not connected. The options include leaving the code of the corresponding operations empty or reproducing the results expected by the hardware. Thanks to these possibilities, corresponding application code can be tested on higher-performance platforms without the time-consuming intermediate step of loading the firmware to the embedded system or using slow emulators.

IV. Conclusion and Further Work

In this paper, three methods for embedded positioning sensors are presented, which on the one hand facilitate the reuse of software to avoid a complete redesign in case of hardware changes, and on the other hand reduce time to market. Employing OOP, virtual register files are initially introduced, where register indexing is performed with simple configuration files for each hardware entity. Subsequently, PAL allows complex commands to be traced back to the corresponding connected hardware. While modifications on the application software are avoided using these methods, the final approach on mockup hardware for cross-compiling allows to speed up design and testing by shifting executing the software away from the embedded system. These advantages come at the cost of slightly more memory usage and processing overhead, which are, however, more available as the hardware continues to develop. On the other hand, porting to alternative hardware is much easier, as only register configurations may need to be adapted, for example.

Acknowledgment

We acknowledge the cooperation with the Centre for Tactile Internet with Human-in-the-Loop (CeTi), a Cluster of Excellence at TU Dresden and with the BMBF funded project 6G-life (project ID: 16KISK001K).

References

[1] E. Gamma, R. Helm, R. Johnson, and J. Vlissides, *Entwurfsmuster: Elemente wiederverwendbarer objektorientierter Software*. mitp-Verlag, 2004.

[2] M. Gunia, B. Zhang, N. Joram, and F. Ellinger, "A hybrid localization framework supporting multiple standards and manifold post-processing," in *2016 Int. Conf. on Localization and GNSS (ICL-GNSS)*, Jun. 2016, pp. 1–6.

[3] M. Gunia, F. Protze, N. Joram, and F. Ellinger, "Setting up an ultra-wideband positioning system using off-the-shelf components," in *Proc. 13th Work. Positioning, Navig. Commun. (WPNC'16)*, Oct. 2016, pp. 1–6.

[4] M. Gunia, A. Zinke, N. Joram, and F. Ellinger, "Setting up a phase-based positioning system using off-the-shelf components," in *Proc. 14th Work. Positioning, Navig. Commun. (WPNC'17)*, Bremen, Germany: IEEE, 2017, pp. 1–6.

[5] M. Gunia, Y. Wu, N. Joram, and F. Ellinger, "Building up an inertial navigation system using standard mobile devices," *Journal of Electrical Engineering*, vol. 5, pp. 299–320, 2017.

[6] M. Gunia, A. Zinke, N. Joram, and F. Ellinger, "Analysis and design of a MuSiC-based angle of arrival positioning system," *ACM Trans. Sen. Netw.*, Jan. 2023, Gerade angenommen, ISSN: 1550-4859. [Online]. Available: https://doi.org/10.1145/3577927.

[7] F. A. Siddiqui, "A hybrid framework for localization and convergence in indoor environments," in *Student Conf. On Engineering, Sciences and Technology*, Dec. 2004, pp. 12–18.

[8] J. J. Salerno, "Where's level 2/3 fusion - a look back over the past 10 years," in *2007 10th Int. Conf. Infor. Fusion*, 2007, pp. 1–4.

[9] M. Wallbaum, "Wheremops: An indoor geolocation system," in *The 13th IEEE Int. Symp. on Personal, Indoor and Mobile Radio Commun.*, vol. 4, 2002, 1967–1971 vol.4.

[10] W. Elmenreich, "A review on system architectures for sensor fusion applications," in *Software Technologies for Embedded and Ubiquitous Systems*, R. Obermaisser, Y. Nah, P. Puschner, and F. J. Rammig, Eds., Berlin, Heidelberg: Springer Berlin Heidelberg, 2007, pp. 547–559, ISBN: 978-3-540-75664-4.

[11] J. Corbet, A. Rubini, and G. Kroah-Hartman, *Linux device drivers: where the Kernel meets the hardware*, 3rd. O'Reilly, 2005.

[12] STMicroelectronics, "RM0385 Reference manual: STM32F75xxx and STM32F74xxx advanced Arm®-based 32-bit MCUs," no. RM0385 Rev 8, pp. 1–1724, 2012.

[13] STMicroelectronics, "UM1905 User manual: Description of STM32F7 HAL and low-layer drivers," no. UM1905 - Rev 5, pp. 1–2312, 2012.